# HIGH-PERFORMANCE SINGLE-UNIT AND STACKED INVERTED TOP-EMITTING ELECTROPHOSPHORESCENT ORGANIC LIGHT-EMITTING DIODES

A Dissertation
Presented to
The Academic Faculty

by

Keith A. Knauer

In Partial Fulfillment
of the Requirements for the Degree
Doctor of Philosophy in the
School of Electrical Engineering

Georgia Institute of Technology
May 2015

# HIGH-PERFORMANCE SINGLE-UNIT AND STACKED INVERTED TOP-EMITTING ELECTROPHOSPHORESCENT ORGANIC LIGHT-EMITTING DIODES

Approved by:


Dr. Bernard Kippelen, Advisor
School of Electrical Engineering
*Georgia Institute of Technology*

Dr. Benjamin Klein
School of Electrical Engineering
*Georgia Institute of Technology*

Dr. Oliver Brand
School of Electrical Engineering
*Georgia Institute of Technology*

Dr. Samuel Graham
School of Mechanical Engineering
*Georgia Institute of Technology*

Dr. Bruno Frazier
School of Electrical Engineering
*Georgia Institute of Technology*



Date Approved: September, 18, 2014

Dedicated to:

The memory of my loving mother.

# ACKNOWLEDGEMENTS

This work would not have been possible without the generous support of my colleagues, friends, and family. First, I would like to thank Prof. Bernard Kippelen for the central role he has played in the development of this work. It is because of his hard work through the years that his group members have a laboratory with the resources and equipment required to conduct this level of research. In addition, I am grateful for the support he has provided to me personally and for his high standards for science that are reflected in the quality of his work. I am also thankful to Prof. Bruno Frazier and Prof. Oliver Brand for the time they have taken to be members of my committee and for their valuable advice.

I am indebted to many of the current and former members of the Kippelen Research Group. Thanks to Dr. Shree Prakash Tiwari for being the first to train me in our labs and for including me in many of his projects where I became familiar with the process of preparing work for publication in peer-reviewed journals. I thank Dr. William Potscavage for teaching me the importance of understanding and respecting the equipment within the lab. His attention to detail has continued to inspire me. I am grateful to Dr. Wojciech Haske for his brilliant scientific insights, his indefatigable work ethic, and his encouragement to overcome the greatest challenges posed by my research. Finally, I'm thankful to Dr. Canek Fuentes-Hernandez for the technical refinements he has made to my work and for his valuable career advice

There are many organizations that have generously contributed to this work. Support has been granted by the National Science Foundation's STC program under Agreement No. DMR-0120967, the Department of Energy under Agreement No. DE-

FG02-04ER46165, and by Applied Materials. Flexible glass substrates were also provided by Corning Incorporated.

Finally, I am grateful to my family in a way that words cannot describe. In particular, thanks to my mother, my father, and my brother. All of my achievements are their achievements as well because of all that they have invested in me.

# TABLE OF CONTENTS

# LIST OF TABLES

# LIST OF FIGURES

# LIST OF SYMBOLS AND ABBREVIATIONS

| | |
|---|---|
| OLED | Organic light-emitting diode |
| AMOLED | Active-matrix organic light-emitting diode |
| LCD | Liquid crystal display |
| CFL | Compact fluorescent lamp |
| LED | Light-emitting diode |
| ITO | Indium-tin oxide |
| VTE | Vacuum thermal evaporation |
| $Alq_3$ | 8-hydroxyquinoline aluminum |
| EQE | External quantum efficiency |
| PPV | Poly(*p*-phenylene vinylene) |
| EL | Electroluminescence |
| PtOEP | 2,3,7,8,12,13,17,18-octaethyl-21H,23H-porphine platinum (II) |
| HIL | Hole-injection layer |
| EIL | Electron-injection layer |
| HTL | Hole-transport layer |
| ETL | Electron-transport layer |
| EML | Emissive layer |
| WVTR | Water vapor transmission rate |
| TFE | Thin-film encapsulation |
| UDC | Universal display corporation |
| HOMO | Highest occupied molecular orbital |
| LUMO | Lowest unoccupied molecular orbital |
| EA | Electron affinity |

| | |
|---|---|
| IE | Ionization energy |
| UPS | Ultraviolet photoelectron spectroscopy |
| IPES | Inverse photoelectron spectroscopy |
| TOF | Time-of-flight |
| SCLC | Space-charge-limited current |
| IC | Internal conversion |
| NR | Nonradiative |
| IQE | Internal quantum efficiency |
| ISC | Intersystem crossing |
| TADF | Thermally activated delayed fluorescence |
| CIE | Commission Internationale de l'Eclairage |
| OVPD | Organic vapor phase deposition |
| PEDOT:PSS | Polyethylene dioxythiophene-polystyrene sulfonate |
| $F_4$-TCNQ | 2,3,5,6-tetrafluoro-7,7,8,8-tetracyanoquinodimethane |
| TpPyPB | 1,3,5-tri(p-pyrid-3-yl-phenyl)benzene |
| TmPyPB | 1,3,5-tri(m-pyrid-3-yl-phenyl)benzene |
| BPhen | 4,7-diphenyl-1,10-phenathroline |
| Ph-QAD | N,N'-diphenyl-substituted quinacridone |
| C545T | 10-(2-Benzothiazolyl)-2,3,6,7-tetrahydro-1,1,7,7 -tetramethyl-1H,5H,11H (1)benzopyropyrano (6,7-8-I,j)quinolizin-11-one |
| BCP | 2,9-dimethyl-4,7-diphenyl-1,10-phenanthroline |
| $Bebq_2$ | bis(10-hydroxybenzo[h] quinolinato)beryllium |
| $Ir(piq)_3$ | tris(1-phenylisoquinoline)iridium |
| TPBi | 1,3,5-tri(phenyl-2-benzimidazole)-benzene |
| $Ir(ppy)_3$ | Tris(2-phenylpyridine)iridium(III) |
| TCTA | 4,4',4"-tris(carbazol-9-yl)-triphenylamine |

| | |
|---|---|
| α-NPD | N,N’-di(naphthalene-1-yl)-N,N’-diphenyl-benzidine |
| Ir(MDQ)2(acac) | Irdium(III)bis(2-methyldibenzo-[f,h]quinoxaline)(acetylacetonate) |
| CBP | 4,4’-bis(N-carbazolyl)-1,1’-biphenyl |
| PES | polyethersulfone |
| FIrpic | Iridium(III)bi[(4,6-di-fluorophenyl)-pyridinato-N,C2’]picolinate |
| mCP | N,N’-dicarbazolyl-3,5-benzene |
| LEU | Light-emitting unit |
| CU | Connecting unit |
| HAT-CN | 1,4,5,8,9,11-hexaazatriphenylene hexacarbonitrile |
| XPS | X-ray photoelectron spectroscopy |

# SUMMARY

Organic light-emitting diodes (OLEDs) have the potential to replace the dominant technologies currently used in both displays and lighting; thus they can have transformative effects on how we receive our information and how we illuminate our environments. One of their major advantages is their reduced energy consumption due to their high efficiency in converting electrical energy into light. Another advantage is their unique combination of mechanical, electrical, and optical properties which can lead to improvements of old technologies as well as enable completely new applications. In order to accelerate the wide-spread implementation of OLEDs in consumer products, advances must continue to be made in manufacturing, device efficiency, thin-film encapsulation, and operational lifetime.

This thesis reports on the design, fabrication, and testing of state-of-the-art, high-performance inverted top-emitting OLEDs. The vast majority of research reports focuses on a device architecture referred to as a conventional OLED which has its anode on the bottom of the device and its cathode on the top. Moreover, most conventional OLEDs are bottom-emitting such that light exits the structure through both a semitransparent bottom electrode of indium-tin oxide and a glass substrate. The particular device architecture developed in this thesis is one in which the devices are inverted (i.e. their cathode is on the bottom as opposed to on top) and top-emitting. Despite the advantages that inverted top-emitting OLEDs possess over conventional bottom-emitting OLEDs, their development has been relatively slow. This is because inverted OLEDs have traditionally been hampered by the difficulty of injecting electrons effectively into the device.

In this work, a novel method of injecting electrons from bottom cathodes into inverted OLEDs is discovered. In several previous reports, bottom Al/LiF cathodes had been used with the electron-transport material $Alq_3$ to produce inverted OLEDs, but the resulting inverted OLEDs exhibited inferior performance to conventional OLEDs with top cathodes of Al/LiF. A new route for the development of highly efficient inverted OLEDs is shown through the use of electron-transport materials with high electron mobility values and large electron affinities.

After systematic device optimization, inverted top-emitting OLEDs are demonstrated that currently define the state-of-the-art in terms of device efficiency. Optimized green and blue inverted top-emitting OLEDs are demonstrated that have a current efficacies of 92.5 cd/A and 32.0 cd/A, respectively, at luminance values exceeding 1,000 $cd/m^2$. Finally, this discovery has enabled the development of the first stacked inverted top-emitting OLEDs ever made, combining all of the advantages offered by an inverted architecture, a top-emissive design, and a stacked structure. These OLEDs have a current efficacy of 200 cd/A at a luminance of 1011 $cd/m^2$, attaining a maximum current efficacy of 205 cd/A at luminance of 103 $cd/m^2$.

# CHAPTER 1

# INTRODUCTION

For over twenty-five years, organic light-emitting diodes (OLEDs) have been the subject of intense and steadily growing research interest because of their potential use in applications that can greatly improve our quality of life. In this chapter, an OLED is first defined. Next, the major application areas of OLEDs are described and some example OLED-based products are presented that have been produced by large corporations investing in the development of OLED technology. Competing technologies are also discussed with their advantages and disadvantages relative to OLEDs. Finally, the chapter concludes with a description of the major challenges that must be overcome for OLED technology to reach its full potential.

## 1.1 Organic Light-Emitting Diodes

An OLED is an electroluminescent device consisting of organic semiconducting material placed between two electrodes: an anode and a cathode [1]. Figure 1.1 contains a general OLED cross-section connected to a voltage source. When a voltage is applied across the electrodes with its positive terminal connected to the anode and negative terminal connected to the cathode, current flows through the OLED, and light is emitted.

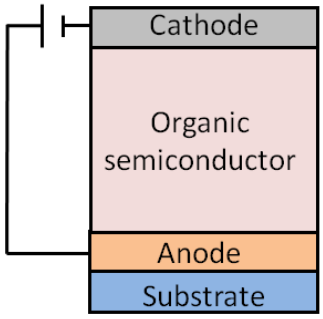


**Figure 1.1.** Device cross-section of an OLED.

## 1.2 Applications

OLEDs are having an increasingly significant impact in two general application areas. One is the area of full-color digital displays, and the other is the area of general-purpose solid-state lighting.

### 1.2.1 Displays

Displays are the primary interface between humans and their electronic devices. In our continually developing and evolving information-based society, the importance of displays is constantly growing as they meet our computing, communication, and entertainment needs.

OLEDs are now being used as the emissive display element in many common consumer electronic devices including digital cameras, audio players, car radios, head-up displays, cell phones, tablets, and televisions. Currently, Samsung Display and LG Display are the leaders in the commercial OLED display market. Samsung is using active-matrix OLED (AMOLED) technology in some of their phones (such as the popular Galaxy and Note product lines), cameras, tablets, smart watches, and televisions. At the time of this writing, Samsung Display has a 55” OLED TV listed at a sale price of

$8,999.99 (see Figure 1.2) [2]. LG Display has been focusing their efforts on large displays and is now selling a 55” curved OLED TV for $9,999.99 (see Figure 1.3) [3]. Other major electronic companies interested in OLEDs for use in displays include Panasonic, Sony, and Mitsubishi [4, 5].

**Figure 1.2.** Samsung’s 55” OLED TV [2].

**Figure 1.3.** LG Display’s 55” OLED TV [3].

#### *1.2.1.1 Competing Technologies*

Liquid crystal displays (LCDs) are presently the dominant technology in the area of flat panel displays. Their rise to dominance was fueled by the development of liquid crystal cell technology and microelectronics for use on large-area glass substrates [6].

The first LCD display used dynamic light scattering and was demonstrated in 1968 by researchers at RCA [7]. The now more common mode of operation, known as the twisted nematic mode, was described in 1971 [8]. Early LCDs used segmented displays with segment independently connected to control electronics. As a consequence, the content of these early displays were severely limited. Higher information-content displays require many pixels and individually addressing each pixel is impractical. The technique of passive-matrix addressing reduces the number of required interconnects compared to direct addressing, but results in displays with limited performance in terms of response time, gray scale, and contrast ratio. Active-matrix addressing was posed as a solution to these drawbacks; in active-matrix addressing, each pixel is independently controlled by a separate switch [9].

A diagram showing the twisted nematic mode of operation of a liquid crystal cell is shown in Figure 1.4. First, generated unpolarized white light passes through a linear polarizer. The polarized light then passes through a cell which consists of a thin layer (4-10 μm) of liquid crystal sandwiched between two glass substrates with electrodes on their inner surfaces. Liquid crystals have properties of crystalline solids and isotropic, deformable fluids. The crystalline anisotropy causes the refractive index and dielectric constant to be dependent on the orientation of the molecules, giving rise to birefringence. In a certain temperature range, nematic liquid crystals exist in a state between the solid and isotropic liquid states, and the orientation of the molecules can be changed by an

electric field. Without a voltage applied, the molecules of the liquid crystal are aligned in such a way as to produce a 90-degree rotation of the polarized light to allow for it to pass through the second polarizer (analyzer), which is oriented perpendicular to the first polarizer. When a voltage is applied across the cell, the molecules of the liquid crystal align perpendicular to the electric field and no longer rotate the polarization of the light. Thus, the light is blocked by the second polarizer. Color is achieved by subdividing each pixel into red, green, and blue subpixels where the white light from a backlight passes through color filters [6].

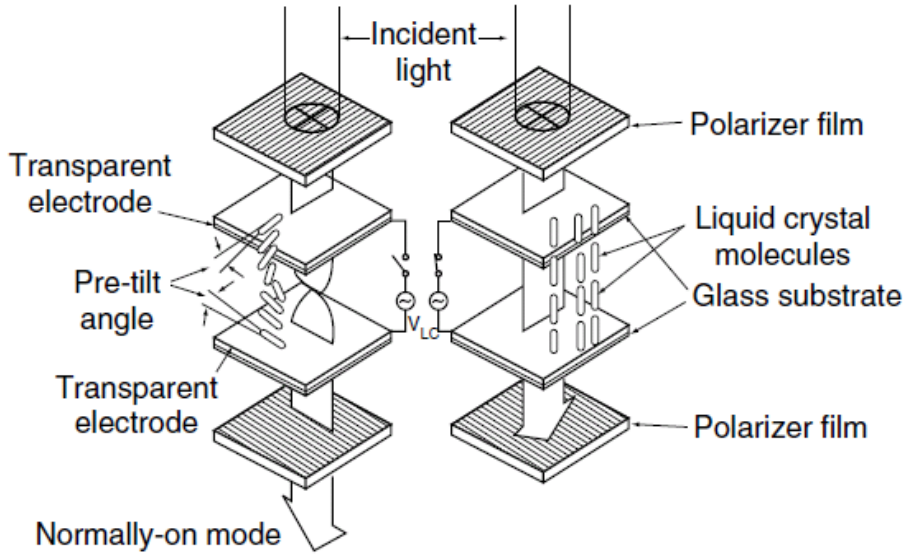


**Figure 1.4.** Twisted nematic operation of an LCD cell. Figure from [6].

### *1.2.1.2 Advantages of OLEDs in Displays*

OLED-based displays have a unique combination of features and offer many advantages over LCD technology. Displays containing OLEDs have high resolution, wide viewing-angles, and short response times [10]. They have superior contrast ratios and efficiencies over LCD-based displays, because OLEDs directly emit their desired

color and black pixels in OLED displays are electrically inactive. In contrast, LCD displays lose energy by producing black and colored pixels by filtering white light generated by a fluorescent bulb or LED backlight [11]. Also, OLED-based displays can be extremely thin and lightweight because the OLEDs themselves have a total thickness of only a few hundred nanometers. Finally, OLED screens can be semitransparent and can possess flexible form factors, enabling entirely new design concepts [10]. Though displays based on OLEDs are currently more expensive than LCD displays, OLED prices are expected to rapidly decline in the near future as the technology continues to mature.

### 1.2.2 Lighting

The act of powering sources of white light accounts for a significant portion of our society's energy consumption and greenhouse gas emissions. About 19% of the electricity generated globally is consumed by powering sources of white light, resulting in a total end-user cost of about $234 billion. Perhaps more significantly, this energy consumption ultimately leads to the emission of about 1900 megatons of $CO_2$ per year, roughly equaling 70% of the combined $CO_2$ emission from all of the world's cars [12]. The majority of our light is currently being produced by inefficient incandescent bulbs and linear fluorescent lamps [13]. Therefore, technologies that can generate white light in a more efficient and environmentally-friendly manner can have a sizable impact on our way of life, especially when one considers that the growth in demand for general lighting might grow as much as threefold by 2030 [12].

Many large companies are investing in the development of white OLED technology in the hopes of producing energy-efficient, long-lasting, and affordable white lighting products; these companies include Philips, LG Chem, Panasonic, OSRAM,

Konica Minolta, and Acuity Brands [13]. The Philips Lumiblade, shown in Figure 1.5, is a lighting panel product available in various sizes with a total thickness of 1.8 mm, a lifetime of 15,000 h, and a power efficacy of 25 lm/W at a luminance of 3,000 cd/m$^2$. Philip's long-term goal is to reach a power efficacy of 140 lm/W [14]. LG Chem offers a product portfolio of white OLED lighting panels of various shapes and sizes with a power efficacy of 60 lm/W. Their roadmap contains the goal of reaching a power efficacy of 80 lm/W by the end of 2013 and 135 lm/W by the end of 2015 [15]. Figure 1.6 shows some design concepts containing LG Chem's white OLED panels. Also of note is Panasonic's demonstration of white OLEDs with a device area of 25 cm$^2$, a power efficacy of 110 lm/W, and an operational lifetime of over 100,000 at a luminance of 1,000 cd/m$^2$ [13, 16].

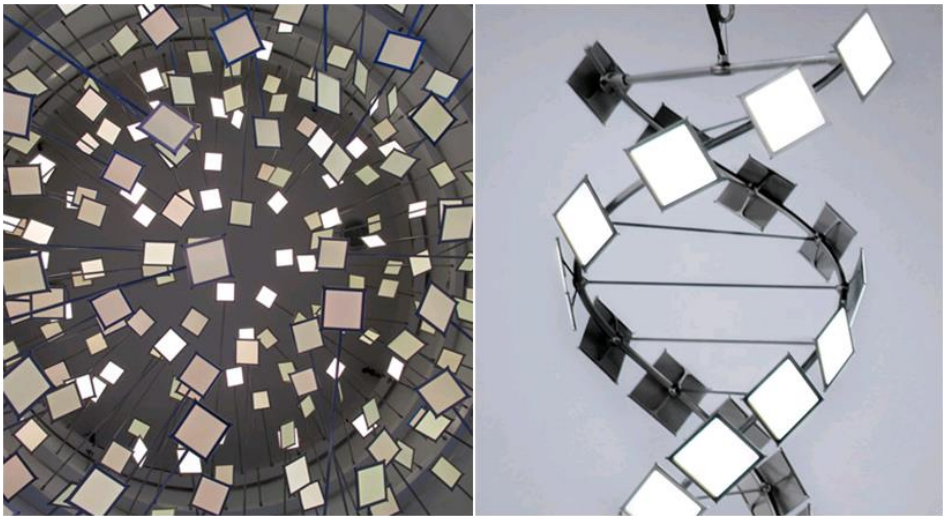

**Figure 1.5.** Two design projects containing the Philips Lumiblade [14].

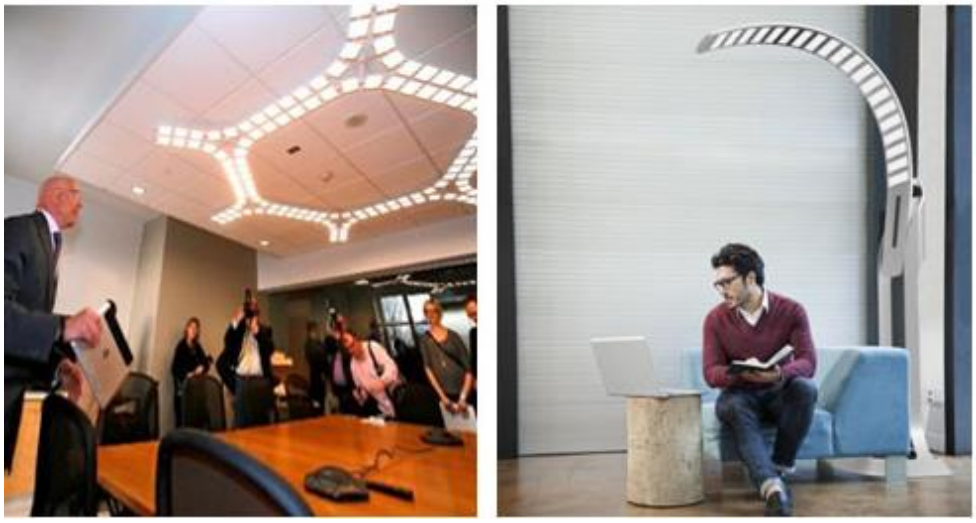

**Figure 1.6.** Design concepts using LG Chem's white OLED panels [15].

### *1.2.2.1 Competing Technologies*

There are many competing technologies to OLEDs in the field of general purpose white lighting. Some of the most significant alternative technologies are presented here. Their respective advantages and disadvantages are also discussed.

#### *1.2.2.1.1 Incandescent Bulbs*

The most recognizable source of white light is the incandescent bulb. It was patented by Joseph Swan in 1860 and later popularized by Thomas Edison. The light generated from an incandescent bulb spans the wavelengths of 400 – 700 nm and is emitted from an electrically heated filament within an evacuated glass enclosure. Its use is currently being phased out, because only 5% of the consumed electricity is converted into visible light, resulting in a low power efficacy of about 15 lm/W. Their average lifetime is about 1,000 h, which is quite low when compared to other technologies [12].

*1.2.2.1.2 Fluorescent Tubes*

The first fluorescent tube was made by General Electric in 1937, and the importance of fluorescent lighting continues to grow to this day. A fluorescent bulb consists of a glass tube filled with an inert gas, such as argon, and a small quantity (3-15 mg) of mercury. When an electric current passes between the tube's electrodes, the electrons within the mercury vapor are excited and subsequently relax to emit ultraviolet radiation. The ultraviolet radiation excites phosphors that are coated on the interior of the glass tube which then emit visible light. Linear fluorescent tubes convert about 25% of their electrical power into light and have power efficacies in the range of 60 – 100 lm/W. Their average lifetimes are in the range of 7,500 – 30,000 h. In the early 1980's, compact fluorescent tubes (CFLs) began to be commercialized. They tend to be less efficient than linear fluorescent tubes, converting about 20% of their electricity into light and have a power efficacy of about 35-80 lm/W. A typical CFL has a lifetime of about of 6,000 – 15,000 h. Large fluorescent tubes are currently the dominant lighting technology in commercial buildings and offices, while CFL's are on the way to becoming the dominant source of light for households. A major disadvantage of all fluorescent tubes beyond their modest efficiency is the environmental threat they pose due to the highly toxic mercury required for their operation [12].

*1.2.2.1.3 Inorganic LEDs*

Inorganic light-emitting diodes (LEDs) are currently the most efficient sources of white light available to the average consumer. The first red organic LED was demonstrated by Nick Holonyak and S. F. Bevacqua [17] in 1962 and the first blue LEDs were demonstrated by Shuji Nakamura in 1993 [12]. Upon the application of a

voltage, light is emitted from a very thin layer of inorganic semiconductor material. For example, in the case of an InGaN LED, a quantum well is constructed by sandwiching a thin (about 5 nm) layer of InGaN between layers of higher-bandgap energy *n*-type GaN and *p*-type GaN. When a voltage is applied across the LED, electrons and holes are injected into the InGaN from the *n*-type and *p*-type GaN, respectively. The electrons and holes occupy different energy bands within the InGaN, and when they recombine, light is emitted with a photon energy equivalent to the difference in the electron and hole energy levels. The color of the monochromatic light that is emitted can be controlled by altering the composition or thickness of the quantum well [12].

Most white LEDs are made by coating blue LEDs with yellow phosphors. A state-of-the-art white LED of this variety is about 30% efficient with a power efficacy of about 100 lm/W and a long lifetime of about 100,000 h. Unfortunately, these devices produce cool white light that is undesirable for use in homes and offices. Warmer white light can be generated by mixing in red phosphors, but the red phosphors currently available decrease the efficiency of the LED. For LEDs to become a dominant lighting technology, advances are still required in efficiency, heat management, color rendering index, lifetime, and cost. Of these, cost is the limiting factor, which remains high because white OLEDs are grown on small diameter substrates of $Al_2O_3$ or SiC. Their cost is expected to drop as the processing substrate sizes continue to grow [12]. In 2013, the worldwide sales of LED lighting products totaled $14.4 billion, representing a 25% growth over 2012 [13].

#### *1.2.2.2 Advantages of OLEDs for Lighting*

There are many advantages that white OLEDs offer over alternative technologies that make them appealing for use in future lighting products. Their advantageous properties include low operating voltages, low operating temperatures, broad spectrum emission, and instant, dimmable, noiseless, and glareless operation. They also possess the mechanical advantages of being thin, large-area, lightweight, flexible, and shatterproof. OLEDs are an intrinsic surface-emitting source of light, so they can be used for completely new design concepts [18]. Finally, they are compatible with methods of production that could lead to very low-cost manufacturing such as solution-processing and roll-to-toll manufacturing [19].

In order for white OLEDs to reach their full potential, advances are needed in the areas of reliability, manufacturing yield, power efficacy, lifetime, and cost [19]. Cost is a major barrier to large-scale commercial deployment. The cost and retail prices of OLED lamps are currently very high because they are still in the early research and development stage. Table 1 contains a list of some of the major white OLED developers and the performance characteristics of their devices. Larger volume production is gaining traction in 2013 and costs are expected to fall significantly in the next 3 years [13]. DisplaySearch has predicted that the size of the white OLED lighting market could grow to $6 billion by 2018 [20]. It is likely that once OLED lighting matures, it will be a complimentary technology to inorganic LED solid-state lighting sources, as many of the disadvantages of one technology are advantages of the other [13].

**Table 1.** Recent white OLED results by several major developers. Recreated from [13].

| Developer | Efficacy (lm/W) | Luminance ($cd/m^2$) | Area ($cm^2$) | CRI (Ra) | $L_{70}$ (1000 hrs) | Drive (V) |
|---|---|---|---|---|---|---|
| **Toshiba** | 91<br>78 | 1,000<br>3,000 | 56 | | | 3.1<br>3.5 |
| **Panasonic** | 87 | 1,000 | 25 | 82 | >50 | 6.1 |
| **UDC** | 70<br>57 | 1,000<br>3,000 | ~200 | 85<br>86 | 30<br>4 | 3.8<br>4.3 |
| **LG Chem** | 60 | 3,000 | 76 | >80 | 15 | 5.8 |
| **UDC/Acuity** | 52 | 2,550 | 115 | 87 | | |
| **UDC** | 43 | 3,000 | 225 | 84 | | 4.9 |
| **DuPont** | 30 | 1,000 | 50 | | | |
| **CDT** | 25 | 1,000 | 225 | ~70 | | 4.3 |

## 1.3 A Brief History of OLEDs

In 1963, fluorescent emission was observed from 10-20 μm thick anthracene crystals placed between two electrodes that were biased at a voltage of about 400 V [21]. Of course, the high voltage operation of these devices made practical applications infeasible. Later, in 1987, the era of modern low-voltage OLEDs was launched by C. W. Tang and S. Van Slyke who were conducting research at Eastman Kodak [1]. Their device was built on a glass substrate and contained a transparent indium-tin oxide (ITO) anode, two thin-film organic layers, and a Mg:Ag cathode. Both organic layers were composed of small-molecules deposited by vacuum thermal evaporation (VTE); one organic layer consisted of an aromatic diamine and the other consisted of 8-hydroxyquinoline aluminum ($Alq_3$). It exhibited an external quantum efficiency (EQE) of 1%, a power efficacy of 1.5 lm/W, and achieved a maximum luminance value of over 1,000 $cd/m^2$ at a voltage below 10 V.

The first solution-processed OLEDs were demonstrated by R. H. Partridge [22] and were based on polyvinylcarbazole (PVCz). Later, in 1990, Burroughs et al. [23] demonstrated OLEDs with an emissive layer consisting of a solution-processed conjugated polymer, poly(*p*-phenylene vinylene) (PPV). The device contained an ITO

anode and an aluminum cathode and yielded an EQE of 0.05%. The fabrication of OLEDs through solution-processable techniques is still an intensely active area of research, as solution-processable techniques might enable higher-speed, larger-area, and lower-cost fabrication of OLEDs as compared to VTE, though this must still be proven through commercial validation [24].

An important advancement was the discovery that the efficiency of OLEDs could be greatly increased by the addition of fluorescent dyes to a host organic material. In 1989, Tang *et al.* demonstrated that by adding fluorescent dyes to the emissive layer of $Alq_3$, the electroluminescent (EL) efficiency of an OLED could be doubled, and the OLED's emissive color could be conveniently tailored by the choice of the fluorescent dye [25]. This fluorescent host/guest doping scheme foreshadowed what would later become a major breakthrough in 1998 by Baldo *et al.* with the demonstration of phosphorescent emission from OLEDs through the incorporation of phosphorescent dyes as dopants [26]. These OLEDs contained the red-emitting phosphorescent dye 2,3,7,8,12,13,17,18-octaethyl-21H,23H-porphine platinum (II) (PtOEP) and had a maximum EQE of 4%.

These discoveries helped to lay the foundation for the field of OLED research which has experienced continuing breakthroughs in device performance. Through the use of optimized structures with phosphorescent dopants and methods of optical outcoupling, modern OLEDs have achieved EQEs as high as 60% at a luminance exceeding 10,000 $cd/m^2$ [27].

## 1.4 The Modern Multilayer OLED

Modern small-molecule OLEDs contain multiple layers of metal, inorganic material, and organic semiconductor material. A cross-section of a general multilayer OLED is shown in Figure 1.7. Each layer performs a specific function in order to decrease the voltage required to drive the OLED and to increase its efficiency. The anode and cathode inject holes and electrons into the device, respectively. The hole-injection layer (HIL) and the electron-injection layer (EIL) modify the work function of the anode and cathode to enhance the efficiency of injecting holes and electrons, respectively. The hole-transport layer (HTL) and electron-transport layer (ETL) consist of materials designed to efficiently transport their respective charge carrier to the emissive layer (EML) of the device. Finally, the material of the EML is chosen to promote the efficient formation of excitons and their radiative recombination to produce a desired color of light [28].

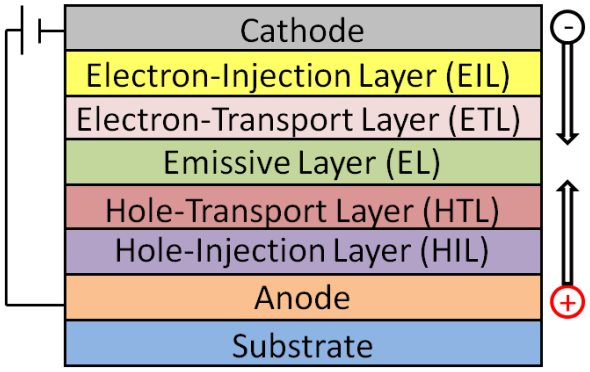


**Figure 1.7.** Cross-section of a general multilayer OLED.

## 1.5 Major Challenges

Despite the remarkable progress that has been made in developing OLED technology, there are many challenges that still have to be overcome for OLEDs to have a

dominant influence in the display and lighting markets. Advances are required in manufacturing, device efficiency, thin-film encapsulation, and operational lifetime. Manufacturing techniques are still in their early stages and expensive; especially for the production of large-area displays, improvements are needed in device yield, reliability, patterning, and scaling. The efficiency of OLEDs (specifically white OLEDs) must be further improved by means of optimized device structures and cost-effective light extraction techniques.

Encapsulation poses a complex challenge for flexible applications. It was recognized early that unencapsulated OLEDs quickly degrade, losing as much as 99% of their initial luminance in under just 150 min of continuous operation in air [29]. This is because OLEDs are adversely affected by oxygen and water in small amounts, with degradation from water being more severe. Their operational lifetime can be greatly enhanced if they are encapsulated with a barrier possessing a maximum water vapor transmission rate (WVTR) of $10^{-6}$ g $m^{-2}$ $day^{-1}$ [30]. For traditional, rigid applications, encapsulation is performed in inert atmosphere using glass substrates and rigid lids sealed with epoxy [31]. The desire for flexible form factors has led to a growing demand for thin-film encapsulation (TFE) methods for OLEDs fabricated on flexible polymer, metal foil, or thin glass substrates. Another TFE challenge is to perform the encapsulation at a low temperature to ensure that the process does not damage the underlying OLED. Several types of encapsulation barriers have been developed using different materials and processes, but one of the most promising approaches is the Vitex encapsulation method in which polymer filler layers and inorganic barrier layers (such as $Al_2O_3$) are alternately deposited in a multilayer stack. The filler layers decouple the defects of the barrier layers

so that permeating water molecules must follow a tortuous diffusion path through the multilayer structure before reaching the OLED [30]. Even though such barrier layers have successfully achieved the desired WVTR, manufacturability must still be proved to make the concept commercially viable.

It is also essential to produce OLEDs with operational lifetimes that are adequately long at sufficiently high luminance levels for use in commercial products [32]. The broadest definition of the operational lifetime of an OLED is the time taken for any loss of required functionality, which might include unacceptable changes in operating voltage or current, the formation of dark spots, changes in emission color or uniformity, pixel failure, or changes in luminance [33]. The exact operational lifetime specifications depend on, and are defined by, the intended application.

The causes for OLED degradation are multifarious, which makes studying operational lifetime a complex problem. Some factors affecting operational lifetime are intrinsic conditions such as the current density level, mode of operation, temperature stability of the constituent materials, purity of the materials, device structure, device efficiency, and device area; other factors are environmental conditions such as temperature, ultraviolet radiation, the presence of moisture, and the presence of air [34-36].

The most frequently used metric for operational lifetime is the amount of time it takes the luminance of the device to decrease to half of its initial value under a given test condition [37]. Such tests can be performed under a variety of test conditions, however, the majority of studies opt to perform tests using constant-current conditions, as the driving electronics used in active-matrix displays typically act as voltage-controlled

current sources [38]. In C. W. Tang and S. Van Slyke's seminal work, their OLED was tested for stability under constant-current conditions in argon at an initial luminance of 50 $cd/m^2$ and showed a half life of about 100 h [1]. Since that time, there has been great progress in developing OLEDs that have both high efficiencies and high operational lifetimes such as the OLEDs using UniversalPHOLED® technology by Universal Display Corporation (UDC). At an initial luminance of 1,000 $cd/m^2$ their red OLEDs have a current efficacy of 30 cd/A and take an estimated 900,000 h to decrease to 500 $cd/m^2$. Also at 1,000 $cd/m^2$, their green OLEDs have a current efficacy of 85 cd/A and take an estimated 400,000 h to decrease to 500 $cd/m^2$ [39]. However, OLEDs containing blue phosphors have a much shorter lifetime and remain a major challenge for the research community. Some of the longest-lived blue OLEDs have been demonstrated by UDC and take only 20,000 h to reach half of their initial luminance of 1,000 $cd/m^2$ [39].

# CHAPTER 2

# BACKGROUND ON OLEDS

The physics governing OLEDs is complex, and a complete understanding of how an OLED operates requires knowledge of many concepts from the disparate fields of solid-state physics, organic chemistry, and optics. This chapter contains a review of some of the relevant physical concepts necessary to understand OLEDs. It begins with a discussion of atomic orbitals, atomic bonding, frontier molecular orbitals, and organic semiconductors. Next, the operation of OLEDs is broken down into the four processes of charge injection, charge transport, exciton formation, and light emission. The chapter concludes with a section on how OLEDs are classified by the research community.

## 2.1 Organic Semiconductors

Organic semiconductors are carbon-rich compounds that can be tailored to possess the charge transporting and/or luminescent properties desired for use in electronic devices. The two types of organic semiconductors of primary interest for use in OLEDs are small molecules and polymers. Small molecules are compounds that possess a defined molecular weight; polymers, however do not have a well-defined molecular weight because they consist of long chains with varying numbers of repeat molecular units [24]. The unique electrical and optical properties of organic semiconductors arise because of the nature of carbon's atomic orbitals and the bonds that carbon forms with other atoms.

### 2.1.1 Atomic Orbitals

In the formalism of quantum mechanics, an electron is described by a wave function, $\Psi$, that is a solution to the Schrödinger equation,

$$i\hbar \frac{\partial}{\partial t}\Psi = \hat{H}\Psi(\boldsymbol{r}, t), \tag{2.1}$$

where $i$ is the imaginary number, $\hbar$ is the reduced Planck's constant, and $\hat{H}$ is the Hamiltonian operator which is the sum of the potential and kinetic energy of the system. Once the wave function is known, it can be used to determine the energy of the electron. The square of the wave function gives the probability of finding an electron at a certain position at a certain time [40].

When the Schrödinger equation is solved for an electron moving around the nucleus of an atom, the wave function is called an atomic orbital. A neutral carbon atom possesses six electrons: two in the 1*s* orbital, two in the 2*s* orbital, and 2 in 2*p* orbitals. The 1*s* and 2*s* orbitals are spherically symmetric, while the 2*p* orbitals exhibit a dumbbell shape. Figure 2.1 shows the electronic configuration and atomic orbitals of a neutral carbon atom. In this diagram, electrons are symbolically represented as arrows with their direction indicating their spin, *S*, which can have a value of either $S = +1/2$ or $S = -1/2$. The Pauli exclusion principal dictates that no two electrons can simultaneously occupy the same quantum state; thus two electrons can only occupy the same orbital if their spins are oppositely paired, and, to minimize energy in filling the degenerate 2*p* orbitals, the electrons occupy orbitals singly in accordance to Hund's rule [41].

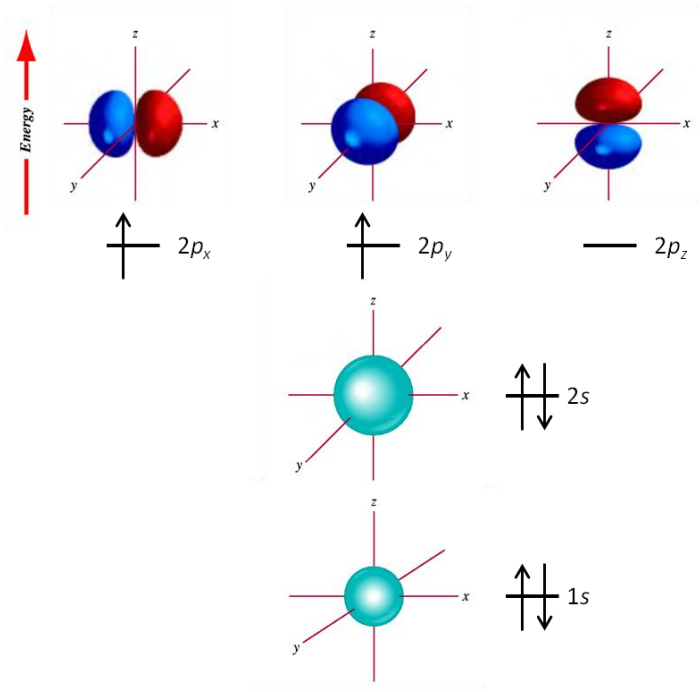


**Figure 2.1.** The electronic configuration of a neutral carbon atom and its atomic orbitals. Figure adapted from [41].

### 2.1.2 Bonding

The outermost electrons in an atom are known as valence electrons and are involved in the formation of bonds between atoms. Covalent bonds are formed when two atoms share electrons. The four valence orbitals of a carbon atom are the 2*s*, 2$p_x$, 2$p_y$, and 2$p_z$ orbitals, where the subscripts indicate the axis along which the lobes of the 2*p* orbitals are directed. When carbon forms bonds, its orbitals combine to form hybrid orbitals that are linear combinations of the 2*s* and three 2*p* orbitals. If a carbon atom forms four identical single bonds with other atoms, the 1*s* orbital and three 2*p* orbitals are involved in the creation of four new identical orbitals called $sp^3$ hybridized orbitals. If a carbon atoms bonds to three atoms, the 2*s* orbital and two of the 2*p* orbitals ($p_x$ and $p_y$) are involved in the creation of three new orbitals called $sp^2$ hybridized orbitals. After $sp^2$

hybridization, there remains a single unhybridized *p* orbital ($p_z$) which is perpendicular to the plane containing the $sp^2$ orbitals, as illustrated in Figure 2.2 [41].

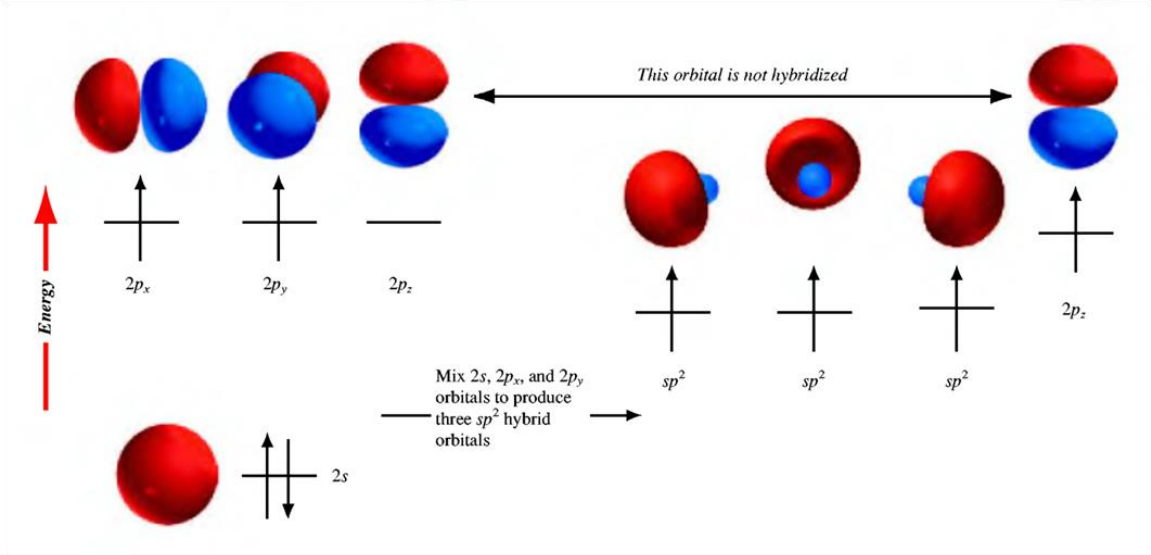


**Figure 2.2.** When carbon forms bonds with three atoms, three $sp^2$ hybridized orbitals are formed and the $2p_z$ orbital is left unhybridized. Figure from [41].

A covalent double bond occurs when four electrons are shared between two atoms. In the case of a carbon-carbon double bond, one of the bonds is a sigma ($\sigma$) bond that results from the overlap of two $sp^2$ hybridized orbitals, and the other is a pi ($\pi$) bond that results from the overlap of the two unhybridized $p_z$ orbitals. Figure 2.3 shows the formation of a double bond using ethylene as an example molecule. The strength of a $\sigma$ bond is much greater than that of a $\pi$ bond; consequently, the electrons forming the $\pi$ bond (known as $\pi$ electrons) are less tightly bound and more delocalized in space. Molecules that have a series of alternating single and double bonds are said to be conjugated. Such conjugation leads to the delocalization of the electrons across the conjugated regions of the molecule, as graphically depicted in the 1,3-butadiene molecule

in Figure 2.4 [41]. The electronic and optical properties of organic semiconductors are largely determined by the delocalization of their $\pi$ electrons [24].

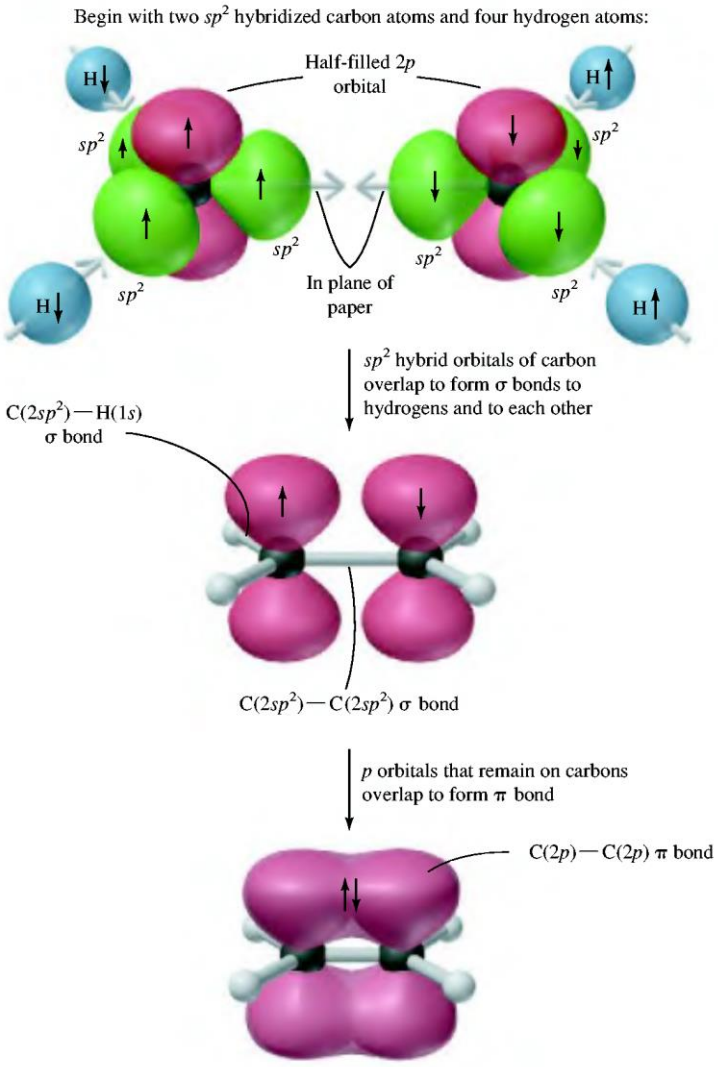


**Figure 2.3.** Two $sp^2$ hybridized carbon atoms forming a bond to produce an ethylene molecule. The overlap of two $sp^2$ orbitals results in a $\sigma$ bond and the overlap of the two unhybridized $p_z$ orbitals results in a $\pi$ bond. Figure from [41].

**Figure 2.4.** A 1,3-butadiene molecule with four carbon atoms in conjugation. The $\pi$ electrons are delocalized across the entire molecule. Figure adapted from [41].

### 2.1.3 Frontier Orbitals

Just as atoms have atomic orbitals, molecules have molecular orbitals. Molecular orbitals can be approximately represented as linear combinations of atomic orbitals. Consider the valence molecular orbitals of the ethylene molecule shown in Figure 2.5 with its associated molecular orbital energy diagram. The overlap of the 2*p* orbitals of the carbon atoms create a bonding ($\pi$) and an antibonding ($\pi^*$) orbital. The overlap of the $sp^2$ orbitals also creates a bonding ($\sigma$) and an antibonding ($\sigma^*$) orbital, but they are not explicitly considered because they are more strongly bound. Just as in atomic orbitals, electrons fill the molecular orbitals in order of increasing energy with a maximum of two electrons per molecular orbital. The $\pi$ orbital is the filled orbital with the highest energy and is known as the highest occupied molecular orbital (HOMO). The $\pi^*$ orbitals is the unfilled orbital with the lowest energy and is known as the lowest unoccupied molecular orbital (LUMO). The HOMO and LUMO are collectively known as the frontier orbitals of the molecule [41]. They correspond to one-electron wavefunctions and can be calculated; however, in practice, what is measured upon excitation or ionization is the energy difference between the *N*-electron ground state of the molecule and the *N*-electron excited state or the $N\pm1$-electron ionized state, respectively. For the purpose of

calculations, it is sometimes assumed that the HOMO level is minus the energy of the ionization energy (IE) and the LUMO is minus the energy of the electron affinity (EA) [42]. The fundamental gap, $E_{fund}$, is defined as the energy difference between the IP and the EA:

$$E_{fund} = IP - EA. \tag{2.2}$$

This quantity is different than the optical gap, which is defined as the energy of the lowest electronic transition possible through the absorption of a photon. The optical gap is lower than the fundamental gap, because when the molecule is in an excited state, the electron and hole are electrostatically bound. Thus, the binding energy, $E_B$, of the electron-hole pair must also be taken into account, so that

$$E_{opt} = E_{fund} - E_B. \tag{2.3}$$

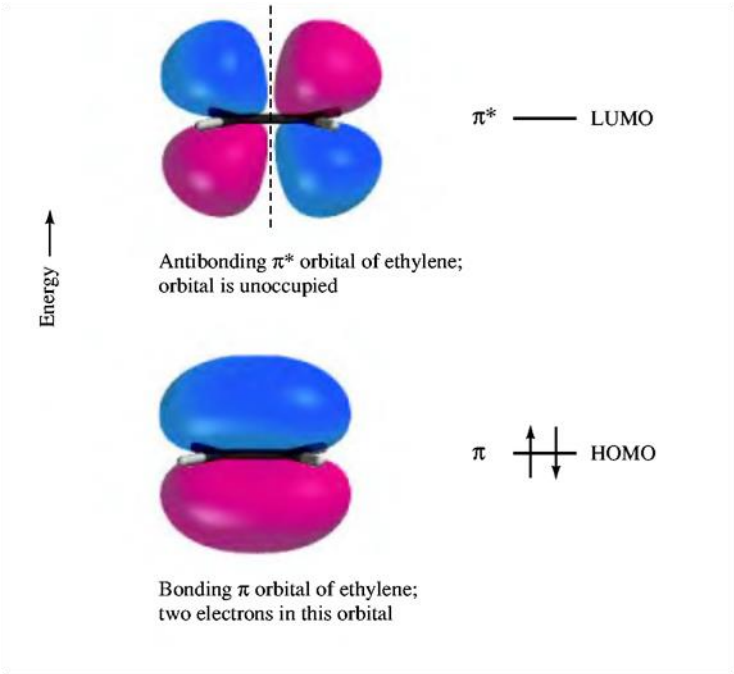


**Figure 2.5.** The $\pi$ and $\pi^*$ molecular orbitals of ethylene. Figure from [41].

In molecular materials, intermolecular interactions cause the energy levels to broaden into electronic bands with widths determined by the strength of the intermolecular interactions. In materials that are highly-ordered, like crystals without defects, the electronic wavefunctions delocalize over the entire structure. In contrast, in disordered films, the electronic wavefunctions are localized over a few molecules or perhaps even a single molecule. In molecular materials, the analog to the fundamental gap of a single molecule is known as the band gap or the transport gap, which is the difference between the IP and the EA of the material. The transport gap is not equivalent to the optical gap, as the lowest optical transition leads to the formation of a bound electron-hole pair and thus the exciton binding energy must be considered. In films composed of π-conjugated molecules, the value of the exciton binding energy is typically on the order of a few tenths of an eV – a value determined by both the small dielectric constant of $\varepsilon \approx 3\text{-}5$ and the electron-electron and electron-vibration interactions. This is in contrast to inorganic crystalline semiconductors where the value of the exciton binding energy is typically on the order of a few meV so that optical excitation at room temperature leads directly to free-carrier formation [42].

The IE and EA of organic films can be estimated experimentally by independent spectroscopy [43]. One of the most powerful techniques for determining the ionization energy is ultraviolet photoelectron spectroscopy (UPS) [44, 45]. In this technique, photons of a given energy are directed at the surface under investigation. Electrons absorb the photon energy and are emitted from the sample. By measuring the energy distribution of the emitted electrons, information is gained of the density of states in the occupied electronic structure of the material. The EA can be directly measured through

the use of inverse photoelectron spectroscopy (IPES) [46]. In IPES, a collimated beam of electrons is directed at the sample. The electrons occupy high-lying unoccupied orbitals and transition to low-lying unoccupied states with some of the transitions being radiative. The photoemission is detected and used to analyze the unoccupied electronic structure of the material.

Figure 2.6 shows an energy level diagram of a simple two-layer OLED. This diagram illustrates how the frontier orbitals of organic materials used in HTLs and ETLs typically distribute with reference to a common vacuum level. Also shown is the typical alignment between these materials and the Fermi levels, $E_F$, of an anode and cathode.

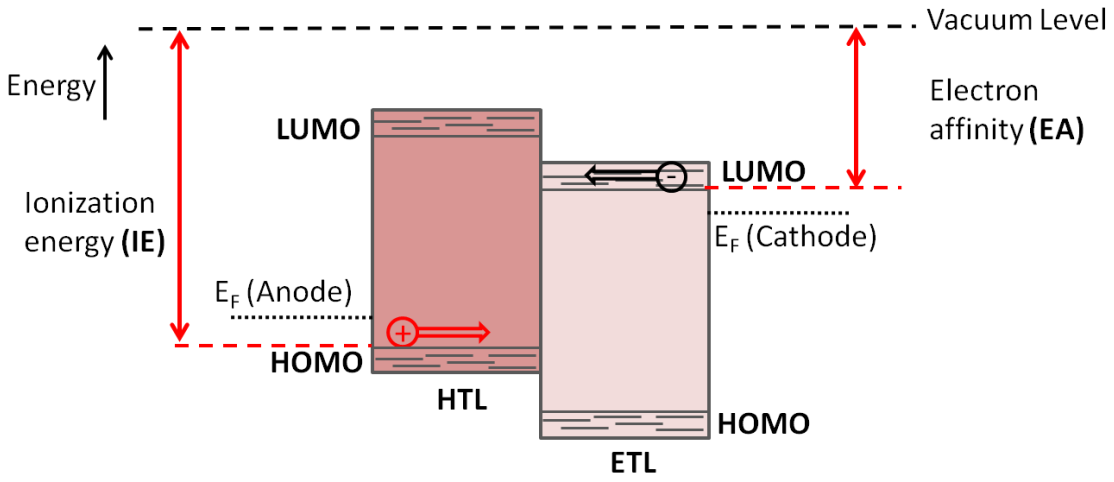


**Figure 2.6.** Energy level diagram of a simple OLED containing a two organic materials.

## 2.2 OLED Operation

The physical operation of an OLED can be conceptually broken down into the four steps depicted in Figure 2.7a-d. (a) When a voltage is applied across the device, holes and electrons are injected into the organic material from the anode and cathode, respectively. (b) These charges are then transported toward the center of the device under

the influence of the applied electric field. (c) The electrons and holes recombine and become bound by the Coulomb force in excited states called excitons. (d) The excitons radiatively decay and release energy through the emission of photons with a color determined by the energy of the excitons. The exciton energy depends on the emissive material for which there is a large variety available, allowing for the emission color to be tuned through a wide range of wavelengths [47].

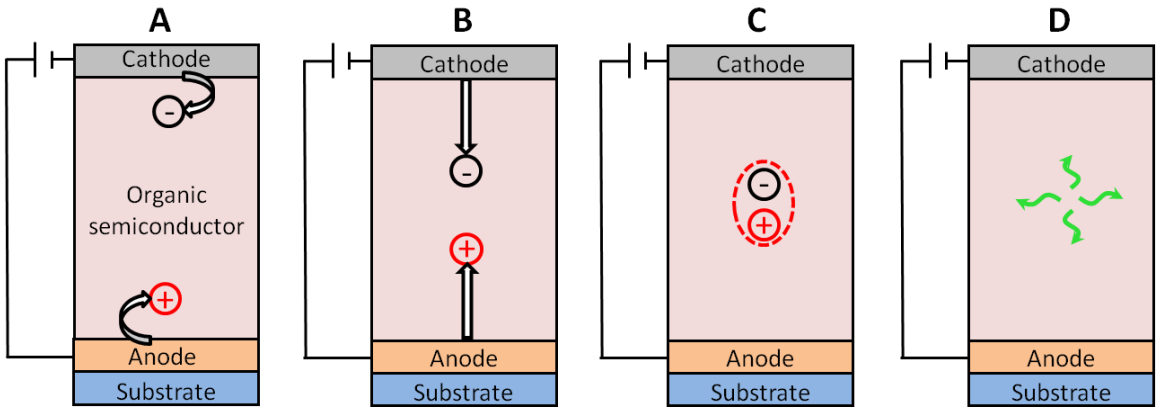


**Figure 2.7.** The four basic steps in the operation of an OLED.

### 2.2.1 Charge Injection

The injection of charge carriers from the electrodes into the organic semiconductors plays an extremely important role in determining the performance of organic electronic devices. Presently, there is no theory that completely describes charge injection from metals into organic materials. This is partly because, injection into amorphous organic semiconductors must account for injection into the manifold of highly localized electronic states where transport occurs via hopping rather than into the bands of a crystalline inorganic semiconductor where the wavefunctions of the electrons are highly delocalized. Furthermore, real metal/organic interfaces are far from ideal and are

strongly affected by the specific structure, chemistry, and morphology of the interface under consideration [43].

It is clear, however, that the most important factor in the injection process is the height of the energetic barrier at the interface that charges must surmount, known as the Schottky barrier. Determining the barrier height, $\Phi_B$, between a metal and an inorganic semiconductor is a straightforward process; it is simply the difference between the work function of the metal, $\Phi_F$, and the EA of the inorganic semiconductor, $\chi_S$, as graphically depicted in Figure 2.8. When the isolated materials are brought into contact, charge transfers across their interface to bring the Fermi levels of the materials into alignment. This state is referred to as equilibrium, and in this state, a depletion region with an associated electric field is established by donor or acceptor ions. The electric field leads to the band bending shown in the Figure 2.8 [43].

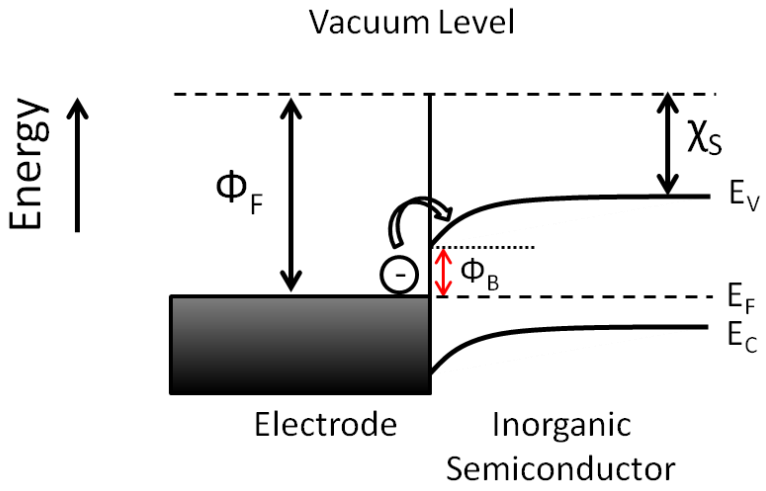


**Figure 2.8.** Energy level diagram of a metal/inorganic semiconductor interface.

However, determining the energy barrier between a metal contact and an organic semiconductor is not straightforward. If the Fermi level of the metal contact is between

the LUMO level and HOMO level of an undoped organic semiconductor, charge injection proceeds by an electron or hole being promoted in energy from the Fermi level of the metal to the LUMO level or HOMO level, respectively. The first complication that arises is that the Fermi level is unknown for most undoped organic semiconductors. A second complication is that the effect of the image potential must be considered; the image potential is responsible for a force of attraction toward the interface caused by the charge left behind after a charge-carrier is injected [43].

Thirdly, even if all of the energy levels of the isolated materials are known relative to a common vacuum level, the energetic barrier cannot be said to be the difference between the Fermi level and the energy level of interest because there is typically an interface dipole that introduces an energy level shift and vacuum level offset. The interface dipole depends on the specific interaction of the interface materials and needs to be considered on a case-by-case basis. The physical origin of these interface dipoles is still under investigation, but some factors causing it are understood. One factor relates to the fact that at the surface of metal, electrons spill out beyond the surface. When an organic layer is deposited on a metal surface, it affects how the electrons spill out. This generally introduces a positive surface dipole moment directed from the surface which lowers the energy needed to inject an electron from a metal. Two other contributions to the surface dipole are the orientation of the molecules at the surface and any chemical interactions at the interface that have either changed the distribution of charge or have lead to the creation of new states at the interface [43].

Despite these difficulties, current injection models have been applied to metal/organic interfaces to provide some physical insight into the process. One common

approach is to consider the injection process to be analogous to a metal/inorganic Schottky contact. The Shockley diode equation then gives the injection current:

$$J = J_0 \left( e^{\left(\frac{qV}{nkT}\right)} - 1 \right) \tag{2.4}$$

where $J_0$ is the reverse bias saturation current density, $q$ is the elementary charge, $V$ is the voltage across the diode, $n$ is the ideality factor, $k$ is the Boltzmann constant, and $T$ is the temperature of the junction. In the thermionic emission process, $J_0$ is given by,

$$J_0 = A^* T^2 e^{\left(\frac{-\Phi_B}{kT}\right)} \tag{2.5}$$

where $A^*$ is the effective Richardson constant and $\Phi_B$ is the height of the barrier to injection [48]. It must be stressed that this equation was originally derived for the thermionic emission of electrons from a metal into a crystalline semiconductor where electrons have wave-like propagation within bands, not for electron injection into highly localized states with transport proceeding via carrier hopping [43].

Fowler-Nordheim tunneling is occasionally used to describe carrier injection into organics at high electric fields. In this model, tunneling occurs from Fermi level of the metal into states beyond a barrier that is assumed to be triangular in shape [49]. The injection current is given by

$$J = AE^2 e^{\left(\frac{-4\sqrt{2m}{\Phi_B}^{2/3}}{3\hbar qE}\right)} \tag{2.6}$$

where $E$ is the applied electric field, $m$ is the electron mass, and $A$ is a prefactor [50]. Again, this equation was derived for the wave-like propagation of electrons and its derivation does not consider electron injection into localized states and transport via hopping [43].

### 2.2.2 Charge Transport

Charge transport in disordered, amorphous organic materials proceeds by free charge carriers hopping between interacting molecules or polymer chains [24, 51]. The process is understood to be an electron-transfer reaction between neighboring molecules, $M_1$ and $M_2$, and is schematically represented by

$$M_1^- + M_2 \rightarrow M_1 + M_2^- \tag{2.7}$$

From semi-classical Marcus Theory, a rate constant for the electron-transfer reaction, $k$, is given by the expression

$$k = Ae^{\left(\frac{-\lambda}{4k_BT}\right)} \tag{2.8}$$

in which $A$ is a prefactor related to the electronic coupling between the electron donor and acceptor molecules and $\lambda$ is the reorganization energy of the electron-transfer reaction [52].

In the equation for one-carrier current flow, the current density, $J$, can be expressed as the sum of a current density due to the drift of carriers, $J_{dr}$, and a current density due to the diffusion of carriers, $J_{di}$, so that

$$J = J_{dr} + J_{di}. \tag{2.9}$$

The drift and diffusion current densities are given by

$$J_{dr} = q\mu nE \tag{2.10}$$

$$J_{di} = -qD\frac{dn}{dx} \tag{2.11}$$

where $\mu$ is the carrier mobility, $n$ is the carrier concentration, $E$ is the strength of the applied electric field, $D$ is the diffusion coefficient. By the Einstein relation

$$D = \frac{\mu kT}{q}. \tag{2.12}$$

However, for undoped organic semiconductors with few free carriers at room temperature, often in practice a simplified theory is used in which diffusion currents are neglected [53].

The charge-carrier mobility, expressed in units of $cm^2\ V^{-1}\ s^{-1}$, is the key quantity used to characterize charge transport. Under the application of an electric field, carriers drift with a velocity, *v*, given by,

$$v = \mu E \tag{2.13}$$

If the mobility of a semiconductor and the charge density are known, the conductivity, σ, of the material can be obtained using

$$\sigma = nq\mu \tag{2.14}$$

where *n* is the carrier density.

The carrier mobility values of a film of material depend strongly on its morphology. For instance, for Si used in thin-film transistors, the field-effect mobility values range from 0.3-1 $cm^2\ V^{-1}\ s^{-1}$ for amorphous-Si, 10-200 $cm^2\ V^{-1}\ s^{-1}$ for low-temperature poly-Si,100-300 $cm^2\ V^{-1}\ s^{-1}$ for high-temperature poly-Si, and 400 $cm^2\ V^{-1}\ s^{-1}$ for crystalline silicon [6]. Highly pure, crystalline films of organic materials can have maximum field-effect mobility values that exceed that of amorphous-Si, such as 40 $cm^2\ V^{-1}\ s^{-1}$ for pentacene crystals [54], 15 $cm^2\ V^{-1}\ s^{-1}$ for rubrene crystals [55], and 4.9 $cm^2\ V^{-1}\ s^{-1}$ for crystalline films of $C_{60}$ [56]. However, typical bulk conductivity values of disordered small-molecule and polymer films typically fall in the range of about $10^{-3}$ – $10^{-5}\ cm^2\ V^{-1}\ s^{-1}$ [24].

The theoretical understanding of charge mobility is complex, because the mobility is influenced by many factors including disorder, the presence of impurities, the strength

of the applied electric field, and temperature [51]. A formalism has been developed for describing transport in disordered amorphous organic semiconductors [57]. Charge hopping is assumed to take place among localized states with a Gaussian energetic disorder distribution and positional disorder resulting in random variations in the electronic coupling between neighboring molecules. Each hopping event is assumed to be independent, with a hopping rate, $k_{ij}$, given by the Miller-Abrahams formalism [58], in which

$$k_{ij} = \nu_0 exp(-2\gamma a \frac{\Delta R_{ij}}{a}) \begin{cases} exp\left(-\frac{\varepsilon_j - \varepsilon_i}{k_B T}\right); & \varepsilon_j > \varepsilon_i \\ 1 \quad ; & \varepsilon_j < \varepsilon_i \end{cases} \tag{2.15}$$

where $v_0$ is a prefactor, $\gamma$ is a factor representing the electronic wave function overlap, $a$ is the lattice constant, $\Delta R_{ij}$ is the distance between transport sites $i$ and $j$, and $\varepsilon_i$ and $\varepsilon_j$ are the energies of transport sites $i$ and $j$. In jumping from a site of lower to higher energy, the hopping rate decreases exponentially with the difference in electronic site energies. On the other hand, if the jump proceeds from a site of higher to lower energy, the last term in the expression is equal to unity.

With these assumptions, Monte Carlo simulations [57] result in an expression for mobility given by

$$\mu = \mu_0 exp\left[-\left(\frac{2\hat{\sigma}}{3}\right)^2\right] exp\left[C(\hat{\sigma}^2 - \Sigma^2)E^{1/2}\right] \tag{2.16}$$

where $\mu_0$ is a prefactor, $C$ is a constant empirically determined to have a value of $2.9 \times 10^{-4}$ $cm^{1/2}$ $V^{-1/2}$, $\Sigma$ is the width of the positional disorder, and $\hat{\sigma}$ is

$$\hat{\sigma} = \frac{\sigma}{k_B T}. \tag{2.17}$$

Using this expression for mobility, excellent agreement has been found between experimental results and the results of simulations [59, 60].

Two common techniques for measuring mobility are the time-of-flight (TOF) technique and the space-charge-limited current (SCLC) technique. Unfortunately, the mobility values measured by these two techniques cannot be directly compared because they use samples that have different geometries and operate on different length scales; because the methods of preparing thick and thin films are different, the resulting films can have different morphologies and thus different mobility values [61].

#### *2.2.2.1 Time-of-Flight Measurements*

The most common method of determining the mobility of organic semiconductors is the TOF technique. The measurement is conducted on an organic layer of a few micrometers in thickness placed between a transparent electrode and a reflective electrode. A laser pulse is directed at the sample which generates free carriers near the transparent electrode. The free carriers are driven to the reflective electrode by an applied electric field ($E = 10^4 – 10^6$ V/cm) where they are collected, and the current is recorded over time. The mobility of the carriers can be then be determined by the expression,

$$\mu = \frac{d^2}{Vt} \tag{2.18}$$

where $d$ is the distance between the two electrodes, $V$ is the applied voltage, and $t$ is the average transit time [51, 61].

#### *2.2.2.2 Space-Charge-Limited Current Measurements*

The SCLC technique is a method of determining mobility from the current-voltage characteristics of an organic diode consisting of a thin organic layer sandwiched

between two electrodes. Ideally, at low values of electric field, the current through the diode is given by Ohm's law. As the current increases, if the diode is not injection limited, the current will be limited by the mobility of the organic semiconductor [61]. The current is said to be space-charge-limited when the charge density injected reaches a value close to that of the charge density of the electrode. In the space-charge-limited regime, and in the absence of traps, the current can be expressed by the Mott-Gurney law in which

$$J = \frac{9}{8}\epsilon_0\epsilon_r\mu\frac{V^2}{L^3} \tag{2.19}$$

where $\varepsilon_0$ is the permittivity of free space, $\varepsilon_r$ is the material's dielectric constant and $L$ is the thickness of the film [53]. As discussed previously, the mobility is field-dependent for an amorphous semiconductor, and this dependence can be incorporated into an expression for SCLC to yield the following approximation for the current density:

$$J \cong \frac{9}{8}\epsilon_0\epsilon_r\mu_0 exp\left(0.891\gamma\sqrt{\frac{V}{L}}\right)\frac{V^2}{L^3} \tag{2.20}$$

where $\mu_0$ and $\gamma$ are parameters obtained by fitting [62].

### 2.2.3 Excitons

When electrons and holes approach one another in an organic semiconductor, they interact and form excitons. In OLEDs, the formation of excitons is a random process and is kinetically bimolecular [63]. A model of this process was proposed by Langevin [64]. First, the coulombic capture radius, $r_c$, must is defined:

$$r_c = \frac{q^2}{4\pi\varepsilon\varepsilon_0 kT}. \tag{2.21}$$

The Langevin model holds if the mean free path of the charge carrier is less than $r_c$. Taking a typical value of $\varepsilon$ = 3.4 for an organic semiconductor, one obtains $r_c \approx 17$ nm. Thus, the required condition is met in low mobility amorphous organic semiconductors where the mean free path is the hopping distance (about 1 nm) [61]. The recombination current is given by

$$R = \gamma n_e p_e = \frac{e(\mu_n + \mu_p)}{\varepsilon n_e p_e} \tag{2.22}$$

where $\gamma$ is the Langevin recombination coefficient, $n_e$ is the electron density, $p_e$ is the hole density, $\mu_e$ is the electron mobility, and $\mu_p$ is the hole mobility.

#### *2.2.3.1 Singlet vs. Triplet Excited States*

Electrons possess a spin of either $S$ = 1/2 or $S$ = -1/2. Letting ↑ and ↓ represent the spin state of the individual electrons, a two-electron system has the following four basis states:

$$\uparrow\uparrow, \uparrow\downarrow, \downarrow\uparrow, \downarrow\downarrow.$$

The arrows in the first and second position represent the spin states of the first and second electron, restively. With these four basis states, the total spin of the composite system can be either $S$ = 0 or $S$ = 1. The state of the system with $S$ = 0 is known as a singlet state and its spin wavefunction, $\sigma_s$, is given by

$$\sigma_s = \frac{1}{\sqrt{2}}\{\uparrow\downarrow - \downarrow\uparrow\}.$$

There are three states that result in the system having a total spin of $S$ = 1. These states are known as triplets and have spin wavefunctions $\sigma_{t1}$, $\sigma_{t2}$, and $\sigma_{t3}$ represented by

$$\sigma_{t1} = \frac{1}{\sqrt{2}}\{\uparrow\downarrow + \downarrow\uparrow\}$$

$$\sigma_{t2} = \uparrow\uparrow$$

$$\sigma_{t3} = \downarrow\downarrow$$

Thus, three of the four states of a two-electron system are triplet states, while only one is a singlet state [40].

#### *2.2.3.2 Host-to-Guest Energy Transfer*

Excitons are mobile excited states that, when they relax to the ground state, usually generate light or heat [24]. A third process known, as the Auger effect, is also possible, wherein the recombination energy is used to provide enough kinetic energy to result in electron photoemission (this effect is rare in organic materials, but has been observed, for instance, in tetracene crystals [63]). Host/guests emissive systems are used in electrophosphorescent OLEDs to maximize performance, where a conductive host contains a phosphorescent dye that is sufficiently dispersed to prevent the effects of concentration quenching [65]. Excitons formed on the host can be transferred to the guest by both the Förster [66] and Dexter [67] energy-transfer processes. An energy transfer process can be schematically represented by

$$D^* + A \rightarrow D + A^* \tag{2.23}$$

where $D$ is the energy donor molecule, $A$ is the energy acceptor molecule, and the asterisk indicates that the molecule is in an excited state. For host-to-guest energy transfer to be efficient, the energy of the host's lowest excited state must be higher than the energy of the guest's lowest excited state.

The Förster resonant energy transfer process occurs through induced-dipole energy transfer and is shown in Figure 2.9. Through Coulombic interaction, the energy released from the relaxation of an excited energy donor can simultaneously excite an energy acceptor. In order for this to occur, the emission spectrum of the energy donor

must overlap with the absorption spectrum of the energy acceptor. This process is considered long-range because it can occur at distances of up to about 40 Å [26].

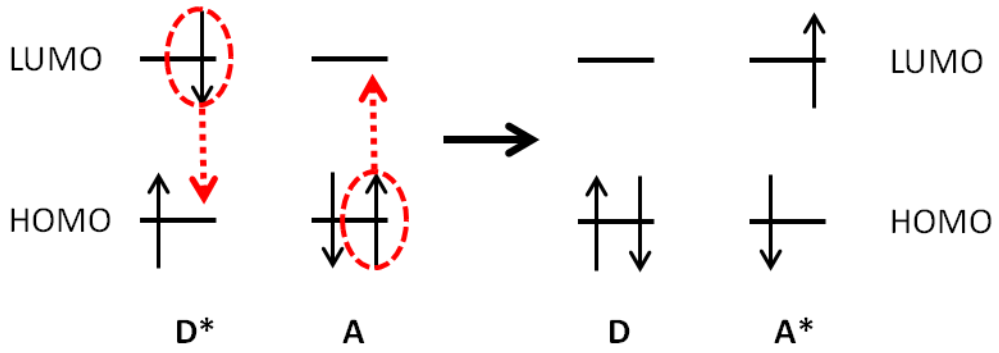


**Figure 2.9.** Diagram illustrating Förster energy transfer.

The Dexter process proceeds by electron-exchange and is illustrated in Figure 2.10. In this process, electrons are exchanged between the energy donor and the energy acceptor and thus it is necessary that there is overlap between the orbitals involved in the transfer. This process occurs over length scales of about 10 Å and is thus considered short-range. The spin before and after the Dexter process is conserved so that both singlet and triplet excitons can be transferred [61].

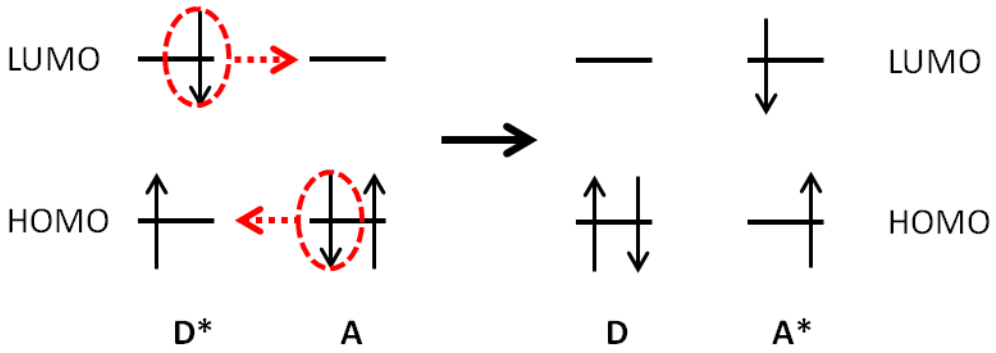


**Figure 2.10.** Diagram illustrating Dexter energy transfer.

### 2.2.4 Light emission

Once a molecule is in an excited state, many different processes can occur. Figure 2.11 contains a simplified Jablonski diagram that graphically depicts some of these different processes. Internal conversion (IC) is the process whereby a singlet or triplet exciton in a higher excited state ($S_n$ or $T_n$, respectively) transitions to a lower excited state. Radiative emission will be strongest from exciton in the lowest excited state ($S_1$ or $T_1$) decaying to the ground state, $S_0$. Nonradiative (NR) relaxation of excitons is also possible which leads to the generation of heat. Fluorescence is photon emission resulting from a singlet excited state radiatively decaying to $S_0$. In fluorescent materials, only singlet states can emit light; this is because the ground state is a singlet state, and the transition from triplets to singlets is forbidden due to the spin selection rules of quantum mechanics. Since fluorescent materials can only radiatively emit from singlet excited states, a severe restriction is placed on the internal quantum efficiency (IQE) of electrofluorescent OLEDs. Assuming, as in small-molecule OLEDs, that the formation rates of singlets and triplets excitons are equal, the quantity of singlet excitons under electrical excitation is only 25% of the total exciton population [68]. However, in some conjugated polymer systems, the rate of singlet formation can be greater than the rate of triplet formation, leading to predicted IQEs as high as 50% [69].

The spin selection rules can be partially lifted through the use of heavy-metal complexes. In these complexes, strong spin-orbit coupling effects from the heavy-metal atom cause the triplet and singlet states to mix. As a result, internal system conversion (ISC) of excited singlet excitons into excited triplet excitons is allowed. In addition, photon emission from triplet states relaxing to the singlet ground state is allowed in a process known as phosphorescence [26, 70].

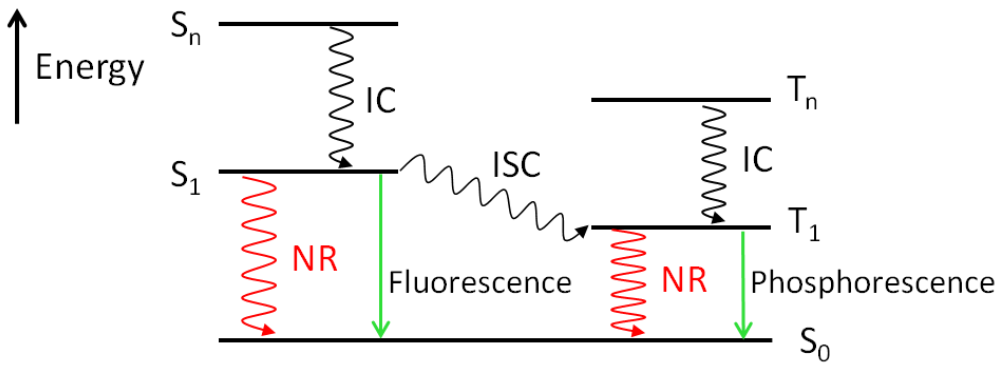


**Figure 2.11.** A simplified Jablonski diagram for a molecule in the excited state.

OLEDs based on fluorescent and phosphorescent emitters each have disadvantages. Devices with fluorescent emitters have low efficiency, and devices with phosphorescent emitters suffer from significant efficiency roll-off due to triplet-triplet annihilation, have poor operational lifetime when blue phosphors are used, and contain expensive, rare metals such as iridium and platinum [71]. A third possible route for an OLED to achieve a high IQE while circumventing the aforementioned disadvantages has recently been discovered using emitters capable of a process known as thermally activated delayed fluorescence (TADF) [72-74]. The process of TADF is explained in Appendix 8.3A.1.

### 2.2.5 Internal Quantum Efficiency

The IQE of an OLED is defined as the ratio between the total number of photons that are internally generated within the device to the total number of electrons injected. For OLEDs, an expression for the internal quantum efficiency, $\eta_{int}$, can be written as

$$\eta_{int} = \gamma \eta_{ex} \varphi_p \tag{2.24}$$

where $\gamma$ is the fraction of injected carriers that form excitons, $\eta_{ex}$ is the fraction of excitons formed which contribute to radiative emission ($\eta_{ex}$ = 0.25 for fluorescent emitters and $\eta_{ex}$ = 1 for phosphorescent emitters), and $\varphi_p$ is the intrinsic photoluminesce efficiency of the emitter [26, 68].

Thus, to maximize $\eta_{int}$, each term in equation (2.24) should be maximized. To maximize $\gamma$, balanced charge injection and transport must be achieved. In practice, attempts are made to make the charge-injection barriers as small as possible and to use charge-transporting materials with well-matched charge-carrier mobility values [61].

The term $\eta_{ex}$ can be maximized by utilizing host/guest systems where the guest consists of a heavy-metal complex dopant within a host material with higher triplet energy. In such systems, nearly all emission is due to phosphorescence. There are two processes by which triplets are formed on the guest: 1) Direct exciton formation and 2) efficient energy transfer of excitons from the host to the guest [61]. The phosphorescent dye is placed within the host at a low volume percentage (about 6%-12% [65]) to avoid crowding-induced concentration quenching. Well-chosen host/guest systems can also have high $\varphi_p$, and it has been demonstrated that OLEDs can achieve an IQE of about 100% [68, 75]

### 2.2.6 Light Outcoupling

Most OLEDs are built upon a transparent glass substrate coated with a transparent ITO anode. The organic material is sandwiched between the ITO below and a highly-reflective cathode above. Generated light must be transmitted through the ITO and the glass substrate in order to exit the device. Thus, the light must pass through several layers

with different indices of refraction, and due to total internal reflection, there is a limited cone of incidence from which generated light will exit the device.

Total internal reflection leads to a significant portion of the emitted light getting waveguided in ITO/organic and substrate waveguiding modes. Once waveguided, the light is either absorbed within the device or emitted from the edges [61]. An expression relating the internal and external quantum efficiencies can be written as

$$\eta_{ext} = \eta_{int}\eta_c \tag{2.25}$$

where $\eta_c$ is a factor representing the fraction of light coupled out of the device into the forward hemisphere [76]. If an OLED is assumed to have a perfectly reflecting cathode, isotropic emission, and no interference effects, the fraction of generated light that exits the substrate is given by

$$n_c = 1 - \sqrt{\left(1 - \frac{1}{n^2}\right)} \tag{2.26}$$

where *n* is the refractive index of the emissive layer [77]. Given that the refractive index for typical organic materials fall in the range of about 1.6 – 2.0, the fraction of outcoupled light for a typical OLED is about 20% [61, 78]. However, more detailed analysis has shown that when considering factors like the dipole orientation and the position of the emission zone, up to 50% outcoupling efficiency can be achieved without additional outcoupling techniques [61].

There is great interest in developing practical methods of enhancing the amount of light extracted from OLEDs. Many techniques have been employed, including roughening or shaping the substrate, as well as using high refractive index substrate materials, microlens arrays, microcavities and scattering media. Though these techniques

can greatly increase the amount of outcoupled light, they can also have an influence on the emission pattern which can lead to non-Lambertian emission [78].

## 2.3 OLED Classifications

Many different OLED device architectures have been designed and tested by the OLED research community. These various OLEDs are classified based on their electrical, optical, and structural characteristics. Some distinguishing characteristics include the location of the device's anode and cathode, and the direction of the emitted light.

### 2.3.1 Conventional vs. Inverted OLEDs

One way an OLED is classified is based on the location of its electrodes. This classification scheme is depicted in Figure 2.12. The OLED in Figure 2.12a has a so-called conventional architecture with the anode on the bottom of the device and the cathode on the top. It is called a conventional OLED because this architecture is the subject of the vast majority of research reports. The OLED in Figure 2.12b is in the inverted architecture, because the location and nature of its electrodes relative to the substrate in the device structure are reversed with the cathode on the bottom in contact with the substrate and the anode on top of the device. Figure 2.12b also shows that in an inverted OLED, the location of each of the functional layers between the electrodes is also reversed.

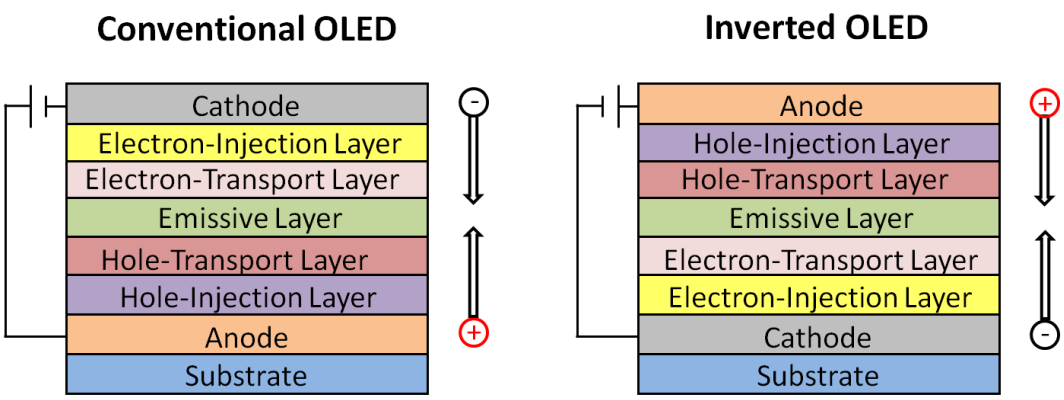


**Figure 2.12.** A (a) conventional OLED and an (b) inverted OLED.

Despite being the subject of fewer studies, inverted OLEDs offer the advantage of being more convenient to integrate with the driving technologies used in AMOLED displays. Different pixel-driving circuits for AMOLED displays with various levels of complexity and compensation for fabrication inhomogeneity have been developed, but in their simplest form these circuits use at least one transistor in series with the OLED; the other components in the pixel-driving circuits control the gate of the driving transistor in order to modulate the current supplied to the OLED. There are two types of driving transistors, *n*-type (electron-conducting) and *p*-type (hole-conducting), as well as two types of OLEDs based on which electrode is on the bottom. During the bottom-up fabrication of any OLED, its bottom electrode must connect to the underlying transistor. This leads to the four possible types of pixel-driving circuits shown in Figure 2.13 [38].

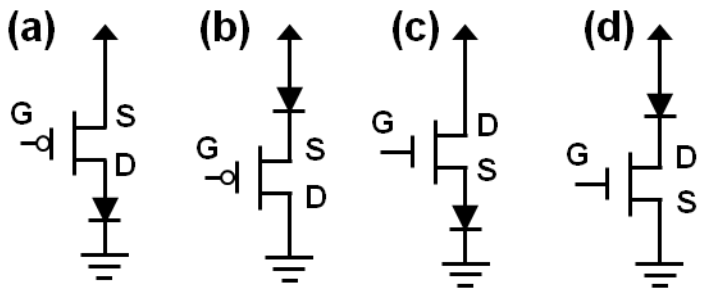


**Figure 2.13.** Circuit schematics of a *p*-type driving transistor connected to (a) a conventional OLED and (b) an inverted OLED, and an *n*-type driving transistor connected to a (c) a conventional OLED and (d) an inverted OLED.

From the standpoint of circuit design it is preferable to place the OLED in the drain path of the driving transistor as in Figure 2.13a with a *p*-type transistor/conventional OLED combination or Figure 2.13d with an *n*-type transistor/inverted OLED combination. When the OLED is in the drain path, the gate-to-source voltage, $V_{GS}$, and thus the current flowing through the transistor, is only dependent on the gate voltage and is independent of the characteristics of the OLED. If the OLED is connected to the source of the transistor as in Figure 2.13b and Figure 2.13c, $V_{GS}$ depends on both the gate voltage and the voltage across the OLED. Thus any variation in the OLED performance due to degradation will affect the operation of the circuit in undesirable ways. Driving transistors used in AMOLED displays contain poly-Si, a-Si, or metal-oxide conducting channels. In all of these technologies, the *n*-type transistors have higher mobility values than *p*-type transistors, resulting in superior performance. Thus, the circuit configuration in Figure 2.13, with an *n*-type driving transistor and an inverted OLED, is the overall preferred configuration [38].

### 2.3.2 Bottom- vs. Top-Emitting OLEDs

Another classification of OLEDs is based on the direction that generated light exits the structure [79]. In this classification scheme, the two general OLED types are shown in Figure 2.14. For bottom-emitting OLEDs (see Figure 2.14a), light exits the structure through both the bottom electrode and the substrate. Alternatively, in top-emitting OLEDs (see Figure 2.14b), light exits from the top electrode. Top-emitting OLEDs have several advantages over bottom-emitting OLEDs. First, top-emitting OLEDs provide the designer with a broad array of choices for substrates including glass, flexible plastics, metal foils, and opaque materials. In AMOLED displays, a top-emitting OLED can be fabricated directly upon its driving circuitry allowing the aperture ratio of the pixel to be increased beyond what is possible with bottom-emitting OLEDs [28]. The pixel aperture ratio is defined as the amount of surface area from which a pixel emits light divided by the total area needed for the pixel including its driving circuitry. When the pixel aperture is maximized, a given total display luminance can be achieved with a lower individual luminance for each pixel. This allows for operating the OLEDs at lower voltages and currents, leading to higher efficiency operation and longer device lifetimes [80]. The larger pixel aperture ratio of the top-emitting OLED is apparent in a comparison between the device cross-sections of Figure 2.14a and Figure 2.14b, which shows the active area of the top-emitting OLED extending above the transistor that is driving it. Also, unlike bottom-emitting OLEDs, top-emitting OLEDs do suffer the waveguide losses caused by light trapping in the substrate [81]. Finally, light-extraction can be easily achieved with top-emitting OLEDs by the simple deposition of an organic layer with appropriate refractive index on the semi-transparent top electrode [82, 83],

whereas light extracting methods for bottom-emitting OLEDs are more complicated, such as microlens arrays [84] or low-index grids [85].

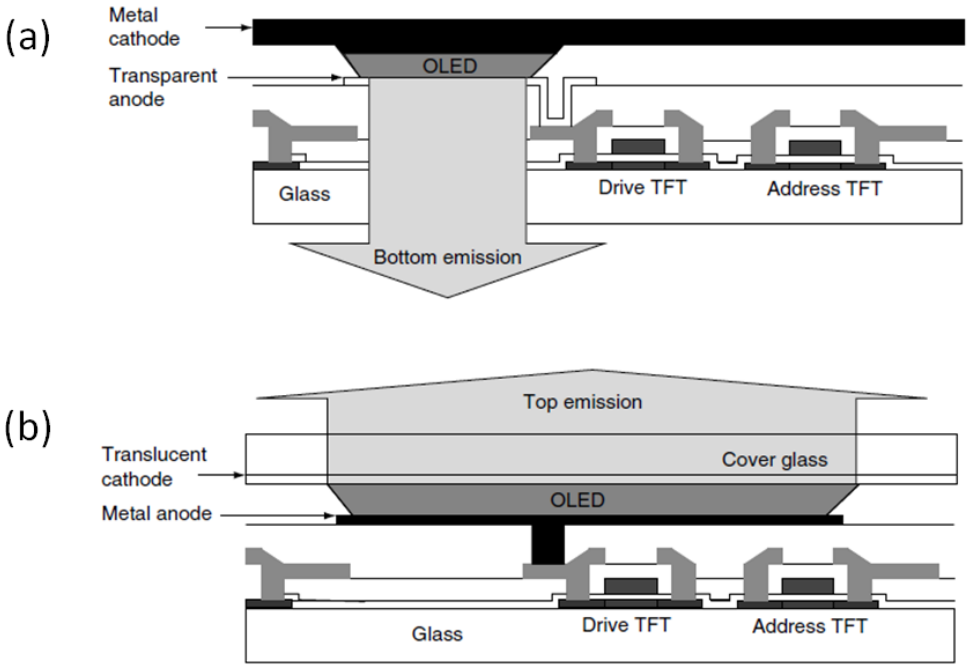


**Figure 2.14.** Cross-sections of a (a) bottom-emitting OLED and a (b) top-emitting OLED. Figure adapted from [6].

Combining the advantages of inverted and top-emitting OLEDs is ideal. Figure 2.15 shows a decision tree that graphically summarizes why inverted top-emitting OLEDs provide the most desirable option for AMOLED displays.

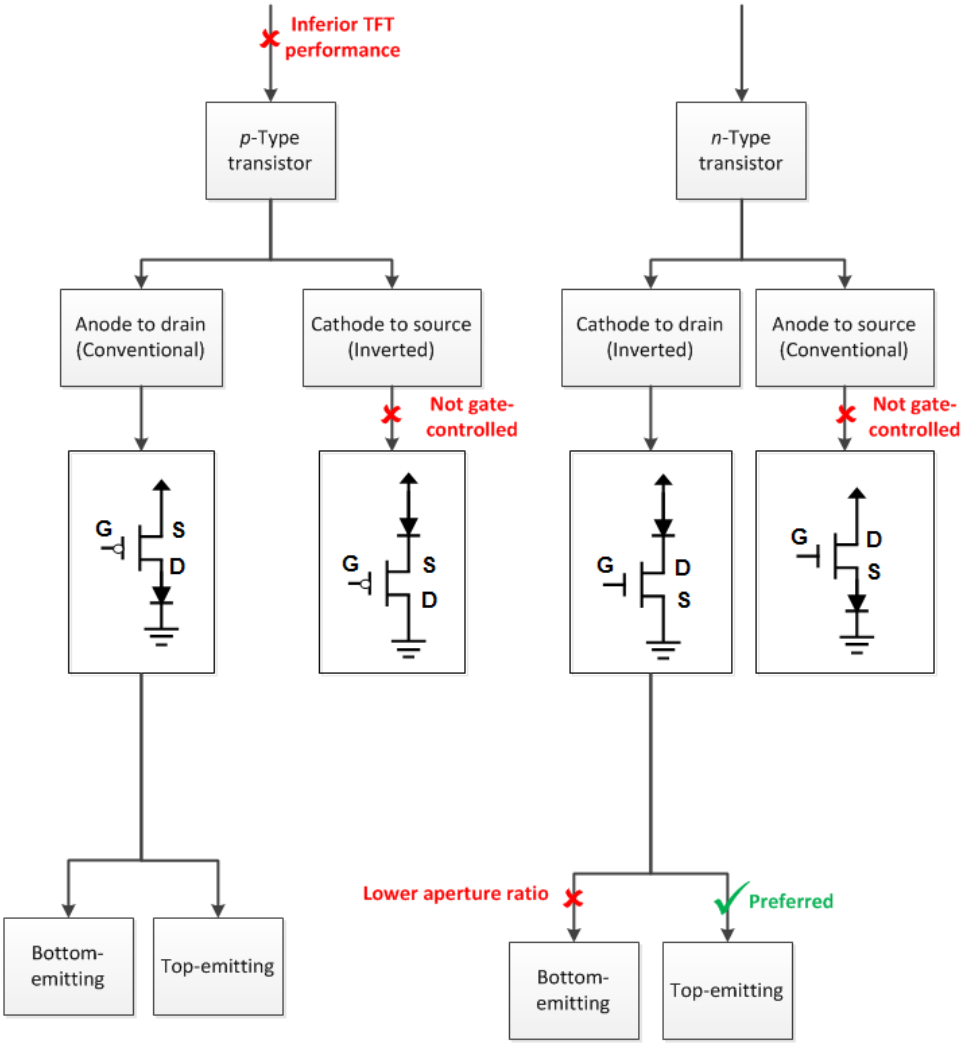


**Figure 2.15.** Decision tree for AMOLED driving and OLED technology.

# CHAPTER 3

# MEASUREMENT AND FABRICTAION PROCEDURES

The research community has adopted a set of standardized performance criteria so that the performance of OLEDs fabricated in different laboratories can be evaluated and compared. As optoelectronic devices, OLEDs are evaluated both in terms of their electrical and optical characteristics.

## 3.1 Performance Metrics

This section presents several of the key metrics that are used in evaluating the performance of OLEDs. Introducing these key metrics requires a review of some fundamental concepts from radiometry, which is the field concerned with the measurement of electromagnetic radiation. As OLEDs are of primarily used in visual applications with human observers, a review is given of some of the basic concepts of photometry, which is the field concerned with the measurement of light as perceived by the human eye.

### 3.1.1 Radiant Energy

A basic quantity in radiometry is radiant energy. It is defined as the amount of electromagnetic energy impinging on or emerging from a surface. Its unit is the Joule, and it is typically denoted by the symbol $Q$.

### 3.1.2 Radiant Flux

The rate of change of radiant energy with respect to time is referred to as radiant flux. Radiant flux is a quantity of power and thus has the units of Watts. Its symbol is $\Phi$ and it is mathematically defined as

$$\Phi = \frac{dQ}{dt}. \tag{3.1}$$

### 3.1.3 Irradiance

The irradiance is the radiant flux per unit area that is impinging on, passing through, or emerging from a point in a given surface. It is typically given the symbol *E* and defined as

$$E = \frac{d\Phi}{ds_0} \tag{3.2}$$

where $ds_0$ is a surface area element on the surface of interest. It has units of $W \cdot m^{-2}$. When determining the irradiance at a point in a surface, all of the solid angle in the hemisphere either below or above the surface must to be considered as shown in Figure 3.1.

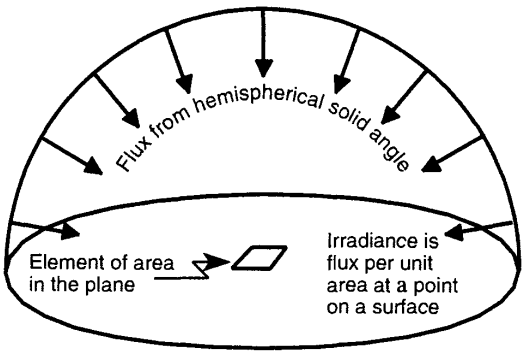


**Figure 3.1.** Geometry used to determine the irradiance at a point in a surface. Figure from [86].

### 3.1.4 Radiance and Spectral Radiance

Radiance is a measure of the area and solid angle density of radiant flux and has the units of $W\ m^{-2}\ sr^{-1}$. It is defined as the amount of radiant flux per unit projected area and per unit solid angle impinging on, passing through or emitting from a particular point on a surface in a specified direction. Mathematically, it is defined as

$$L = \frac{d^2\Phi}{d\omega ds} \tag{3.3}$$

where $\omega$ is the solid angle in a specified direction and $s$ is the projected area on to the surface containing the point of measurement. It is important to note that radiance is a function of both direction and position, and that in order to specify it, one must specify the surface of interest, a point in the surface, and the direction in which the measurement is taken. The geometry used to define radiance is shown in Figure 3.2.

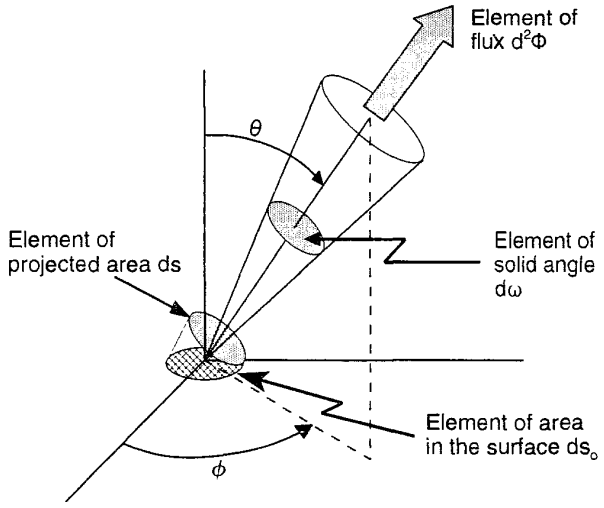


**Figure 3.2.** Geometry used to determine the radiance at a point in a surface of interest in a specified direction. Figure from [86].

### 3.1.5 Luminance

The human eye is the detector for most practical applications based on OLEDs. Thus a discussion of the optical performance of OLEDs in the context of applications requires an understanding of how the eye perceives visible light. The subset of the field of radiometry concerned with the detection of electromagnetic radiation by the human eye is known as photometry.

The detection of light by the eye is a complex process. Light entering the eye is first transmitted through preretinal optics and ultimately received by the retina which contains two different types of eye receptors known as rods and cones. Energy from the light is absorbed by the rods and cones and is converted into electrochemical signals that are sent through the optical nerve to the brain. The rods are used for vision under low levels of illumination known as scotopic vision. The cones are used for photopic vision, or day vision, and are responsible for the perception of colors. The absorption spectra of the cones and the transmittance of the eye's preretinal optics cause the human eye to have varying degrees of sensitivity to the wavelengths of visible light (wavelengths ranging from 360 – 800 nm) [86].

In 1924, the Commission Internationale de l'Eclairage (CIE) described a standardized spectral response for the human eye which is known as the photopic response. The photopic response is often denoted $V(\lambda)$ and is shown in Figure 3.3 [86]. As can be seen from this figure, the human eye is most sensitive to green light with a wavelength of 555 nm [12]. The photopic response is used to convert radiometric quantities to eye response-weighted photometric equivalent quantities. Photometric quantities are usually denoted by the same symbols as radiometric quantities with an added subscript of '$v$' to indicate that they have been weighted against the photopic response.

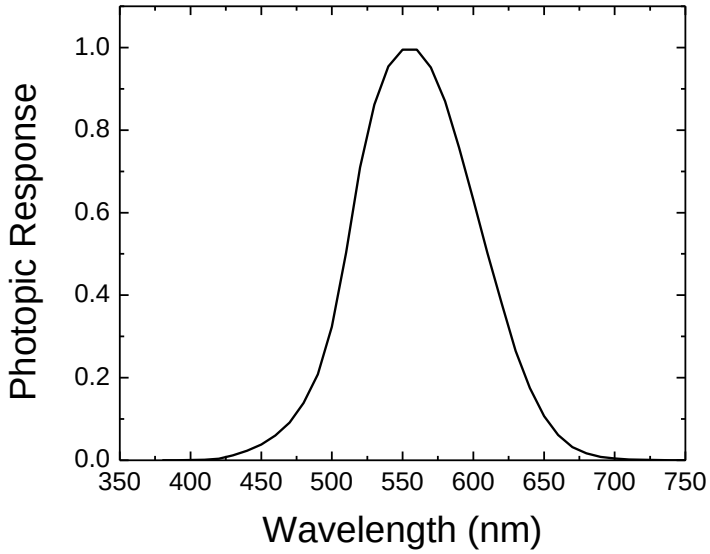


**Figure 3.3.** The photopic response of the human eye, denoted *V(λ)*.

The photometric equivalent of radiance is luminance, $L_v$, which is expressed in the units of lm $m^{-2}$ $sr^{-1}$ or cd/$m^2$ [76]. It is often thought of as the quantity that describes the subjective experience of brightness in photometry [6]. Mathematically, it is defined as

$$L_v = 683[\frac{lm}{W}] \int_{380}^{770} L(\lambda)V(\lambda)d\lambda. \quad (3.4)$$

For some perspective on the subjective experience of luminance refer to Table 2, which contains some common types of displays with luminance values that are typical for each.

**Table 2.** Common display technologies with typical luminance values [6].

| **Device** | **Typical Luminance [cd/m$^2$]** |
|---|---|
| Notebook LCD | 200 |
| Desktop LCD | 350 |
| LCD television | 600 |

### 3.1.6 External Quantum Efficiency

A mathematical definition of the EQE of an OLED is

$$\eta_{EQE} = \frac{n_{ph}}{n_e} \times 100\% \tag{3.5}$$

where $n_p$ is the total number of photons emitted from the device into the forward hemisphere and $n_e$ is the total number of electrons injected into the device. This definition is chosen to exclude the light emerging from the sides of the substrate that has been waveguided in the glass substrate, the ITO anode, and the organic layers [76].

### 3.1.7 Current Efficacy

The current efficacy is the ratio of the luminance and the current density. It is expressed in units of cd/A and is mathematically defined as

$$\eta_I = 0.1\frac{L_v}{J} \tag{3.6}$$

where $J$ is the current density of the OLED expressed in units of mA/cm$^2$. Current efficacy is a useful metric for quantifying the performance of OLEDs for use in displays. This is because the luminance of an OLED is usually measured over a small solid angle in the direction of the surface normal and displays are also typically viewed over a small solid angle in the direction of the surface normal [87].

### 3.1.8 Luminous Efficacy of Radiation

The luminous flux, $\Phi_v$, is the radiant flux weighted by the photopic response and is given by the expression,

$$\Phi_v = 683[\frac{lm}{W}]\int_{380}^{770} \Phi(\lambda)V(\lambda)d\lambda. \tag{3.7}$$

The unit of luminous flux is the lumen (denoted lm). The luminous efficacy of radiation, $K_r$, is defined as the ratio of the luminous flux to the radiant flux:

$$\mathrm{K_r} = \frac{\Phi_v}{\Phi}. \tag{3.8}$$

It is a quantity expressing the effectiveness of a beam of radiation for stimulating a response in the human eye and has units of lm/W.

### 3.1.9 Power Efficacy

Power efficacy, or lighting system luminous efficacy, is a measure of the amount of luminous flux produced by a light source at a given electrical input power. It is also expressed in units of lm/W. It is expressed as

$$\mathrm{K_s} = \frac{\Phi_v}{\mathrm{P}} \tag{3.9}$$

where $P$ is the electrical input power in units of Watts.

## 3.2 Lambertian vs. Non-Lambertian OLEDs

A radiator is said to be Lambertian if its radiance is independent of direction. Such a radiator is called Lambertian because it follows Lambert's cosine law, which states that the irradiance from an area element is given by the expression,

$$E(\theta) = E(0)\cos\theta \tag{3.10}$$

where $\theta$ is the angle between the direction of measurement and the direction perpendicular to the area element [86]. The relationship between irradiance and radiance is

$$E = \int_{\Omega} L(\theta, \varphi)\cos\theta \, d\omega \tag{3.11}$$

where $\Omega$ is the solid angle. If the solid angle over which the radiance is integrated is taken to be the whole hemispherical solid angle, then $\Omega = 2\pi$, and by converting to a spherical coordinate system with the point of interest taken as the origin this equation becomes

$$E = \int_0^{2\pi} \int_0^{\pi/2} L(\theta, \varphi) \cos\theta \sin\theta \, d\theta d\varphi. \tag{3.12}$$

If the radiator is Lambertian and its radiance is independent of direction, then the radiance can be removed from the integral, and the integration yields,

$$E = \pi L \tag{3.13}$$

The emission profile of conventional bottom-emitting OLEDs fabricated on ITO-coated glass is approximately Lambertian. Since the angular distribution of the light is known, a single measurement of the light output of an OLED is sufficient to calculate the EQE of the device. This measurement is typically taken over a small solid angle (the solid angle subtended by the detector) in the direction of the OLED's surface normal [87].

## 3.3 CIE Coordinates

The perception of color by a human being involves two separate processes. The first is a physical process in which a spectral radiant flux impinges on the retina. The second is the psychobiological process of the spectral radiant flux being received by the cones within the eye and this signal being interpreted by the brain. Accurately predicting the perception of color arising from the latter process is complex [86]. The topic of measuring and describing color is the focus of the science of colorimetry [6].

The perception of color varies slightly from one person to another; however, color experiments across many different individuals have revealed that there is enough

consistency to allow for color analysis for practical applications. Color-matching experiments with human observers have shown that nearly all colors can be described by the additive mixture of three different primary sources of light with properly chosen spectral flux distributions. Such a three-variable system is called a trichromatic system [86].

The CIE 1931 Color System is a trichromatic system roughly based on the primary color stimuli of red, green, and blue. Within the system, three primary color-matching functions denoted $\bar{x}(\lambda)$, $\bar{y}(\lambda)$, and $\bar{z}(\lambda)$, and plotted in Figure 3.4, are used as weighting functions for a given color stimulus. The color of a stimulus can be uniquely characterized by the tristimulus values *X*, *Y*, and *Z*, which are obtained using the following definitions [86]:

$$X = \int_{380}^{780} S(\lambda)\bar{x}(\lambda)d\lambda \tag{3.14}$$

$$Y = \int_{380}^{780} S(\lambda)\bar{y}(\lambda)d\lambda \tag{3.15}$$

$$Z = \int_{380}^{780} S(\lambda)\bar{z}(\lambda)d\lambda. \tag{3.16}$$

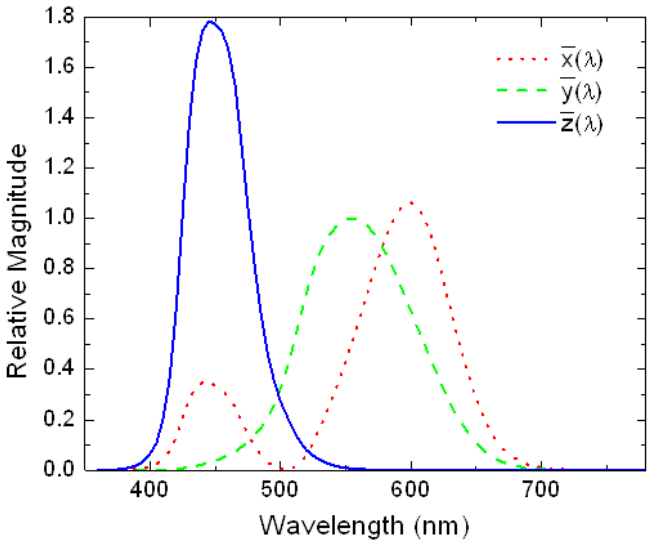


**Figure 3.4.** The three-color matching functions of the CIE 1931 Color System, $\bar{x}(\lambda)$, $\bar{y}(\lambda)$, and $\bar{z}(\lambda)$.

A transformation used to simplify color analysis is applied to the tristimulus values in which they are normalized as follows:

$$x = \frac{X}{X + Y + Z} \tag{3.17}$$

$$y = \frac{Y}{X + Y + Z} \tag{3.18}$$

$$z = \frac{Z}{X + Y + Z}. \tag{3.19}$$

The values *x*, *y*, and *z*, are known as chromaticity coordinates, and it is clear from their definition that

$$x + y + z = 1. \tag{3.20}$$

Thus, a chromaticity point is uniquely specified with only the coordinates *x* and *y*. The coordinates define an (*x*,*y*) point on the chromaticity diagram shown in Figure 3.5 [86]. This diagram includes all of the colors perceptible to the human eye. Pure colors of

monochromatic light are on the outer curve and mixed colors, such as white, are closer to the center [6].

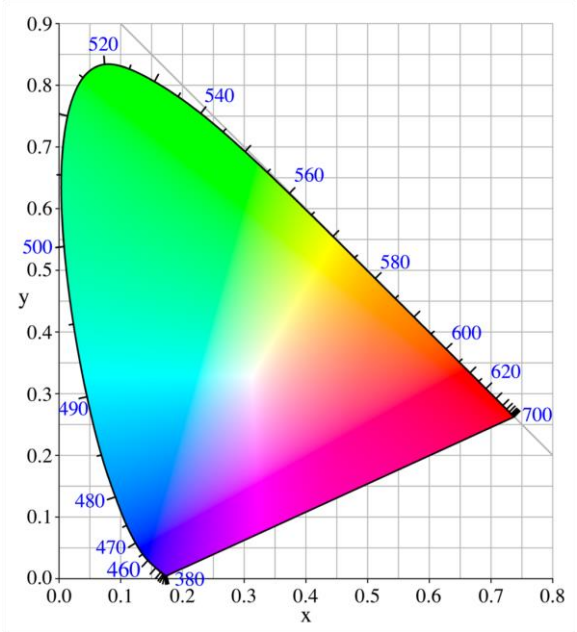


**Figure 3.5.** The CIE 1931 chromaticity diagram.

## 3.4 Measurement Highlights

This section describes the equipment that was used to collect the experimental data contained within this work as well as the methods that were used to calculate the performance characteristics of the devices under test.

### 3.4.1 Electroluminescent Spectrum Measurements

The angular-dependent electroluminescent spectra of OLEDs were collected by first placing the OLEDs within a custom-built enclosure upon a rotatable stage and connecting them to electrical pins. A Keithley 2400 SourceMeter was used to bias the OLEDs and the spectra were collected with a radiometrically calibrated spectrometer (Ocean Optics USB4000) interfaced with a workstation. The spectrum is collected at

each angle of interest by rotating the device using a software-controlled motor connected to the rotatable stage.

### 3.4.2 Photodiode Measurement Setup

Current vs. voltage and luminance vs. voltage characteristics of devices are acquired using a custom-built measurement setup consisting of various pieces of equipment controlled by a computer workstation running control software (National Instruments LabVIEW). When measuring OLEDs, they are placed behind a quartz window within a custom-built enclosure and connected to electrical pins. A general-purpose source measure unit (Keithley 2400 SourceMeter) is used to measure the current of the OLED as a function of the voltage applied. The emitted light exits the quartz window, and a radiometrically calibrated photodiode (Thorlabs Inc, FDS 100) is used to measure the optical power emitted from the OLED in the direction normal to its surface. The photocurrent generated by the photodetector is amplified by an operational amplifier (AD 549LH) in a current-to-voltage converting circuit with an amplifying feedback resistor. The output voltage is acquired by a digital acquisition unit (National Instruments USB-6221) which is connected to the workstation.

A schematic view of the OLED measurement setup is shown in Figure 3.6. The workstation records the OLED voltage, OLED current, and photodetector voltage and uses these to calculate the OLED performance characteristics, such as luminance, current efficacy, and EQE (when the OLED is a Lambertian emitter) at each data point.

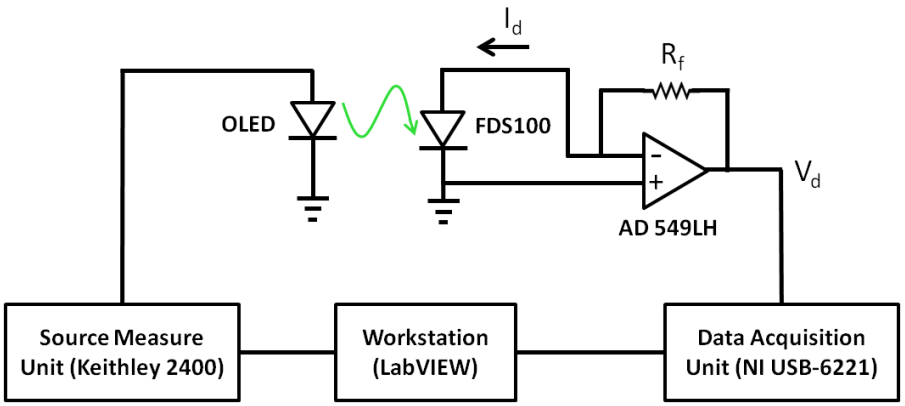


**Figure 3.6.** Custom-built OLED measurement setup used to characterize the electrical and optical performance of OLEDs.

In this circuit, the current of the photodetector, $I_{det}$, can be derived from Ohm's law and is given by,

$$I_{det} = \frac{V_{det}}{R_f} \tag{3.21}$$

where $V_{det}$ is the voltage produced at the output of the current-to-voltage converter and $R_f$ (with a resistance of 5 MΩ) is the feedback resistor.

### 3.4.3 Luminance Calculation

To use a photodiode to measure the luminance of an OLED, the flux transfer from the source to the detector must first be determined. The general geometry of for this problem is shown in Figure 3.7.

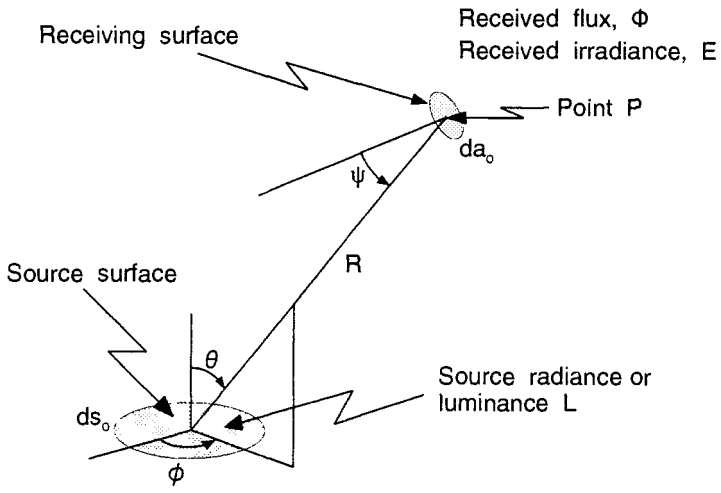


**Figure 3.7.** The geometry of the radiation transfer problem between a source and a photodiode. Figure from [86].

From Figure 3.7 and the definition of radiance, the radiance measured by the photodetector can be expressed as,

$$L = \frac{d^2\Phi}{d\omega ds_0 \cos\theta} \tag{3.22}$$

where $\theta$ is the angle between the surface normal of the source and the direction of interest, $d\omega$ is an infinitesimal solid angle element in the direction of interest, and $ds_0$ is an infinitesimal area element on the source. The figure also contains $da_0$, which is an infinitesimal area element on the detector, the distance between the source and the detector, $R$, and the angle $\Psi$, which is the angle formed between the normal of the detector and the line drawn between the source and detector points. The solid angle element subtended by the projected area of the receiver element at the distance $R$ from the source is given by,

$$d\omega = \frac{da}{R^2} = \frac{da_0 \cos\theta}{R^2} \tag{3.23}$$

Combining these two equations and solving for $d^2\Phi$ yields the expression,

$$d^2\Phi = L\frac{da_0\cos\Psi\, ds_0\cos\theta}{R^2} \tag{3.24}$$

Thus, the total flux received by the detector is given by,

$$\Phi = \int_{S_0}\int_{A_0} L\frac{\cos\Psi\cos\theta}{R^2}da_0 ds_0 \tag{3.25}$$

In the case of the measurement setup previously described, $R$ = 10 cm, and the area of the photodetector, $s_0$, is 12.96 mm$^2$. Because the photodetector area is much smaller than the measurement distance, it is assumed that $L$, $R^2$, $\cos(\Psi)$, and $\cos(\theta)$ do not vary much over the regions of integration and can therefore be removed from the integral. This results in the simplified expression,

$$\Phi = L\frac{\cos\Psi\cos\theta}{R^2}\int_{S_0}\int_{A_0} da_0 ds_0 \tag{3.26}$$

Furthermore, because the source and the receiver face each other directly, $\Psi = 0°$ and $\theta = 0°$, making $\cos(\Psi)$ and $\cos(\theta)$ equal to unity. Thus, the expression for the total amount of flux received by the source from the receiver is given by,

$$\Phi = L\frac{S_0 A_0}{R^2} \tag{3.27}$$

Solving for radiance gives the expression,

$$L = \frac{\Phi R^2}{S_0 A_0} \tag{3.28}$$

The photodetector has a responsivity that is wavelength dependent, and, because the OLED is a broad spectrum source, this wavelength dependence must be taken into account [76]. The responsivity of the photodiode, $R_{det}(\lambda)$, is given by,

$$R_{det}(\lambda) = \frac{I_{det}(\lambda)}{\Phi_{det}(\lambda)} \tag{3.29}$$

where $I_{det}(\lambda)$ is the photocurrent produced by the detector and $\Phi_{det}(\lambda)$ is the power at a given wavelength impinging on the detector. A weighted detector responsivity can be derived by integrating the product of the wavelength-dependent detector response with the spectrum of a device under test, $S(\lambda)$, by means of,

$$R_{det} = \frac{\int_{380}^{780} R_{det}(\lambda) S(\lambda) d\lambda}{\int_{380}^{780} S(\lambda) d\lambda} = \frac{I_{det}}{\Phi_{det}} \tag{3.30}$$

where $\Phi_{det}$ and $I_{det}$ are the total flux received by the detector and the total photocurrent produced by the detector, respectively. By combining this with equation (3.21) and equation (3.28), the expression for radiance can be rewritten,

$$L = \frac{I_{det} R^2}{R_{det} S_0 A_0} = \frac{V_{det} R^2}{R_f R_{det} S_0 A_0} \tag{3.31}$$

The luminance can then be obtained by converting the radiance to luminance using equation (3.4).

### 3.4.4 EQE Calculation for Lambertian OLEDs

In order to determine the EQE of an OLED under test, the number of emitted photons and the number of injected electrons must be calculated. Assuming that the OLED is a Lambertian emitter, the number of emitted photons can be determined from the radiance measurement at the surface normal. First, this radiance measurement must be used to find the total flux emitted by the source, $\Phi_{OLED}$. Recalling the definition of irradiance and a Lambertian emitter gives,

$$E = \frac{d\Phi_{OLED}}{ds_0} = \pi L \tag{3.32}$$

Solving for $\Phi_{OLED}$ and integrating over the source area gives,

$$\Phi_{OLED} = \pi L S_0 \tag{3.33}$$

Substituting the equation (3.31),

$$\Phi_{OLED} = \frac{\pi V_{det} R^2}{R_f R_{det} A_0} \tag{3.34}$$

The total number of photons emitted by the OLED is given by the expression,

$$\eta_{ph} = \frac{\Phi_{OLED}}{hc} \frac{\int_{380}^{780} \lambda \times S(\lambda) d\lambda}{\int_{380}^{780} S(\lambda) d\lambda} \tag{3.35}$$

The total number of electrons injected is simply given by,

$$n_e = \frac{I}{q} \tag{3.36}$$

The total EQE can then be calculated as given by equation (3.5).

## 3.5 Fabrication Highlights

The following section describes highlights of the process used to fabricate the devices in this research. First, a description is given of the method used to purify the organic materials. This is followed by a detailed fabrication procedure including an explanation of the process of vacuum thermal evaporation.

### 3.5.1 Purifying Organic Semiconductors

Impurities are any compounds of small concentration present within an intended compound that has a different chemical structure. Impurities are typically side products created during synthesis. When these impurities have HOMO and LUMO levels that fall within the HOMO-LUMO gap of the intended material, they can act as traps that affect transport, as well as sites for carrier recombination [24, 51]. Thus, to obtain high

performance and high reliability in organic electronic devices it is extremely important to have materials of high purity.

Small molecules can be purified by separating them from their impurities in a straightforward manner using the fact that they have a well-defined molecular weight. A common technique for producing pure powders ideal for use in VTE is by the process of temperature gradient zone sublimation. In this technique, several grams of the material to be purified are placed within a long quartz tube that is placed within a furnace with a temperature gradient. The tube contains smaller glass tubes that act as sleeves to catch purified material. The tube ensemble is first pumped down to a pressure below $1 \times 10^{-6}$ Torr and the source material is slowly heated up to its sublimation point (see Figure 3.8). After several days, the source material will grow as pure crystals on a central glass sleeve in a cooler part of the furnace; the less volatile impurities will be left in the source sleeve and the more volatile impurities will be removed by the vacuum pump [88]. The crystals from the region containing the pure material can then be extracted. Using gradient zone sublimation, fractional impurities as low as $10^{-4}$ are attainable [24].

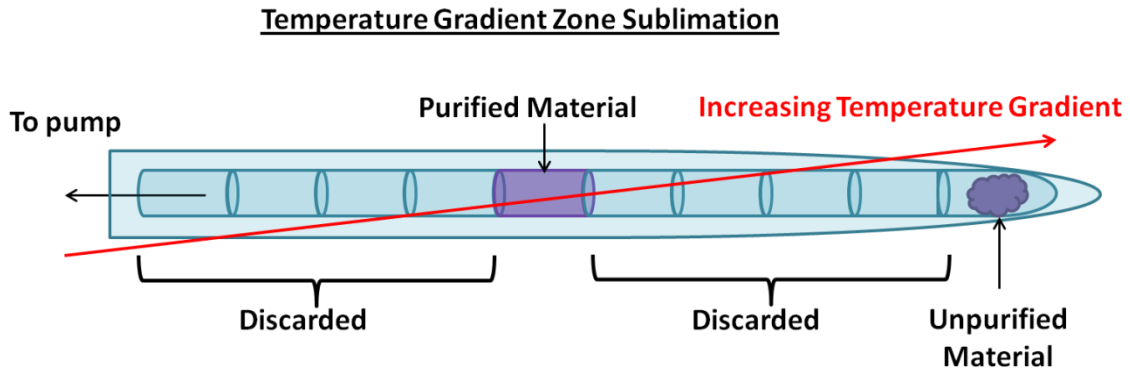


**Figure 3.8.** Diagram of the technique of temperature gradient zone sublimation.

### 3.5.2 Vacuum Thermal Evaporation

The most commonly used technique for depositing small-molecule organic materials is VTE. In this process, a source material is placed in one of many crucibles placed inside electrically heated sources; the different sources allow for many layers of different materials to be deposited during a single system evacuation. The substrates are placed several centimeters above the sources. Patterning is achieved by the use of shadow masks in proximity to the substrate capable of minimum feature sizes in the range of 20 – 75 μm. The thicknesses of the deposited layers are monitored by quartz crystal microbalances allowing for a thickness control of about ± 0.5 nm [24].

The major shortcomings of VTE are the large quantity of material that is wasted and the low level of cleanliness for the system. Point-type sources have a 5% material utilization, and line-type sources have a 40% – 50% material utilization. The unused material is deposited on the deposition system itself [89]. These coated areas flake and generate particles that cause defects in the devices. Keeping VTE systems clean requires significant system downtimes for maintenance. Despite these disadvantages, most research samples and most commercial OLED screens are produced using VTE [24]. Organic vapor phase deposition (OVPD) is a relatively new technique used to deposit organic films [24, 90, 91] that has some key advantages over VTE. It might become an important technology for advancing the organic electronics industry and is explained in the Appendix in section 8.3A.2.

### 3.5.3 Fabrication Procedure

All of the devices presented have a common fabrication and measurement procedure. First, glass micro-slides (VWR international) are cut into 25.4 mm × 25.4 mm

squares and are used as substrates. The glass substrates are sequentially cleaned by ultrasonication in baths of detergent water, distilled water, acetone, and isopropanol for 20 min each and then blown dry with nitrogen. The dry substrates are treated by oxygen plasma for 2 min to improve the wetting of the subsequent poly(3,4-ethylenedioxythiophene) poly(styrenesulfonate) (PEDOT:PSS) layer. PEDOT:PSS (Clevios P VP AI 4083) is dispensed on the substrate through a 0.45 μm polyvinylidine fluoride filter and spin-coated at a speed of 5,000 rpm for 1 min. The substrates are then annealed at 140 °C for 10 min. With this recipe, the thickness of the PEDOT:PSS as measured by spectroscopic ellipsometry is about 40 nm. A previous report demonstrated that when using glass substrates, a layer of PEDOT:PSS leads to improved reliability for electron-dominated organic diodes [92]. This layer planarizes the substrate and provides improved wetting during the deposition of the bottom electrode leading to improved device yield, reliability and performance.

The samples are then transferred to a high-vacuum VTE system (EvoVac, Armstrong Engineering Inc.) which is evacuated to a base pressure of $3 \times 10^{-7}$ Torr. All metal layers are deposited at a rate of 2 Å/s and all other inorganic materials, such as LiF and $MoO_3$, are deposited at a rate of 0.2 Å/s. The organic layers are deposited at a rate of 1 Å/s. The typical active area of a completed device is about 3.6 × 4.2 mm. The patterning on a substrate is achieved by evaporating through a series of shadow masks sequentially placed in near-contact to the substrate. A general layout of a completed device is shown in Figure 3.9. All organic materials are purchased from Sigma-Aldrich (St. Louis, MO, USA) or Luminescence Technology Corporation (Hsin-Chu, Taiwan)

and purified by gradient-zone sublimation prior to their deposition by thermal evaporation.

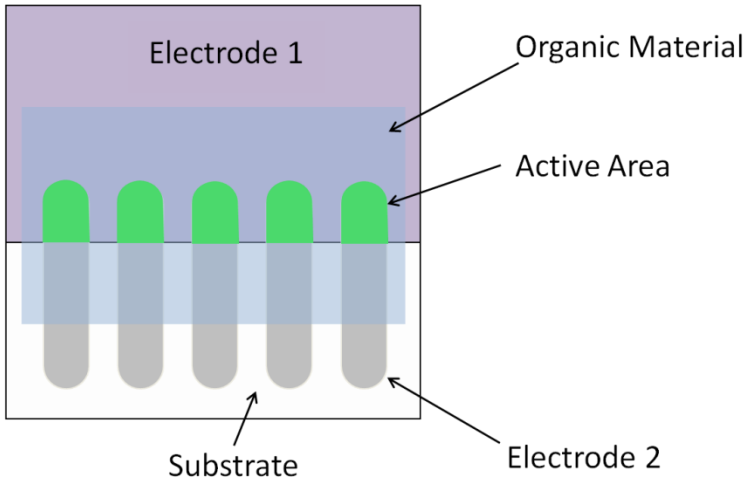


**Figure 3.9.** General top-view layout of a completed device.

After fabrication, the thermal evaporator is opened within a nitrogen-filled glove box where the devices are measured with the measurement setups described in sections 3.4.2 and 3.4.1.

# CHAPTER 4

# Electron-Dominated Devices and Al/LiF Bottom Cathodes

This chapter contains a discussion of the major challenge of fabricating inverted OLEDs and some approaches that the research community has used to overcome this challenge. Of particular interest is the use of bottom Al/LiF cathodes, which were believed to be a poor cathode for choice for inverted OLEDs. Experimental results of electron-dominated devices are then shown that support the conclusion that Al/LiF bottom cathodes can be nearly as effective as Al/LiF top cathodes if one makes a judicious choice of the ETL used.

## 4.1 Challenge of Bottom-Cathode in OLEDs

The major challenge of fabricating inverted OLEDs has been finding a relatively stable bottom cathode capable of effectively injecting electrons into the device [38]. Effectively injecting electrons into organic materials is challenging because a large energetic barrier usually exists at the metal/organic interface adjacent to the cathode. The EA of most organic materials fall within the range of 2.6 – 3.3 eV [93]. To minimize the barrier to electron injection, low-work function metals can be used. Cs (2.14 eV [94]) and Rb (2.16 eV) have the lowest work function values (less than 2.2 eV [94]), but due to their low melting points and high instability, they are very difficult to use in VTE. Ca (2.87 eV [94]) and Mg (3.66 eV [94]) are commonly used, but they are highly unstable in the presence of oxygen and water. A more desirable choice is aluminum, but its work function (4.3 eV [94]) is high enough to produce a significant energy barrier.

Doping organic semiconductors allows for the convenient creation of ohmic contacts. Doping refers to the process of introducing electron rich or electron poor dopant molecules into a material to either increase the material's conductivity or to enhance the process of charge injection [24]. In a doped film, mobile electrons or holes are created by electron donors or electron acceptors, respectively. In *p*-type doping, an electron acceptor, such as 2,3,5,6-tetrafluoro-7,7,8,8-tetracyanoquinodimethane ($F_4$-TCNQ), is used to remove electrons from the filled states near the HOMO level of the host matrix in order to generate holes. In *n*-type doping, electrons are donated from an electron donor to unoccupied states near the LUMO level of the host matrix. Thus, good *n*-type dopants have an IE value that is smaller than the EA value of the host material; unfortunately, such materials have high chemical reactivity and are thus undesirable for production environments [95]. As with inorganic semiconductors, highly doped space-charge layers next to contacts lead to thin interfacial barriers that can be tunneled through. This provides great flexibility in choosing contact materials because alignment between the metal's Fermi level and the desired transport level is no longer required for effective charge injection [96].

### 4.2 Al/LiF Bottom vs. Top Cathodes

Often, interfacial doping is achieved through the addition of a thin electron injection layer (EIL) consisting of an oxide or fluoride containing an alkali or alkaline earth metal such as LiF [97] or CsF [98]. These EILs have been shown to increase the performance of OLEDs by up to an order of magnitude [61]. It is generally believed that these interlayers undergo a chemical reaction in the presence of some metal cathodes, such as Al, and the neighboring ETL. The chemical reaction liberates the low work

function metal, such as Li or Cs, leading to interfacial doping [98, 99]. A common cathode system in conventional OLEDs consists of Al/LiF/$Alq_3$ [1]. In the thermal evaporation sequence of a conventional OLED (see Figure 4.1a), a chemical reaction between these three components has been shown to occur. Liberated Li atoms donate electrons to $Alq_3$ molecules, forming $Alq_3^-$ radical anions, and resulting in interfacial doping [95, 100]. However, attempts at fabricating inverted OLEDs with LiF on top of an bottom cathode of Al (see Figure 4.1b) have yielded modest performance with $Alq_3$ as an ETL [101, 102]. It has been hypothesized that the energy necessary to induce the chemical reaction between Al/LiF/$Alq_3$ in the conventional deposition sequence is provided in the last step when the hot metal vapor of the cathode condenses upon the preformed layers of the $Alq_3$ and LiF; however, in the inverted deposition sequence, the cathode is deposited first and some studies have concluded that the energy necessary to drive the chemical reaction is too low [101, 102].

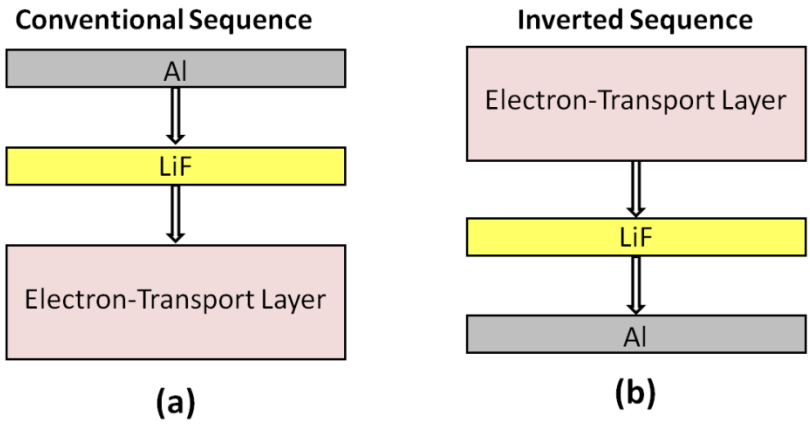


**Figure 4.1.** (a) The conventional evaporation sequence and (b) the inverted evaporation sequence.

### 4.3 Electron-Dominated Devices

Single-carrier-dominated devices [103] are a platform for assessing the effectiveness of electrodes at injecting a single carrier type into an organic material. They typically consist of a sandwich of an organic material between two electrodes. The electrodes are selected so that the energetic barriers between their work function and the transport levels of the organic only allow for the injection of a single carrier type.

Inverted OLEDs using a bottom Al cathode, an EIL of LiF, and an ETL of $Alq_3$, have yielded inferior performance [101, 102] to conventional OLEDs with the same layers; however; the use of other ETLs with bottom Al/LiF cathodes has remained relatively unexplored. Here, electron-dominated devices are used to assess the effectiveness of bottom Al/LiF cathodes at injecting electrons into ETLs with high electron mobility values, and to compare the effectiveness of bottom Al/LiF cathodes to top Al/LiF cathodes.

For this experiment, electron-dominated devices containing either 1,3,5-tri(*p*-pyrid-3-yl-phenyl)benzene (TpPyPB) or 1,3,5-tri(*m*-pyrid-3-yl-phenyl)benzene (TmPyPB) were fabricated. The chemical structures of these pyridine-containing triphenylbenzene materials are shown in Figure 4.2. The electron-dominated device structure is shown in Figure 4.3 and consists of Glass/PEDOT:PSS (40 nm)/Al (50 nm)/LiF (2.5 nm)/TpPyPB or TmPyPB (95 nm)/LiF (2.5 nm)/Al (50 nm). Note that the difference between the work function of the Al contact and the HOMO levels of the ETLs (6.7 eV for both materials [104]) ensures that a sufficiently large hole-injection barrier exists to make hole injection from the Al/LiF electrodes negligible. Thus, the current measured is due primarily to electrons.

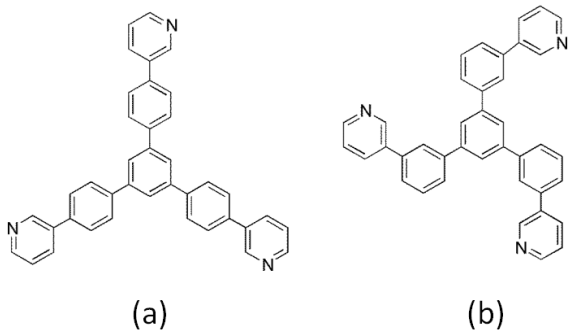


**Figure 4.2.** Chemical structures for (a) TpPyPB and (b) TmPyPB.

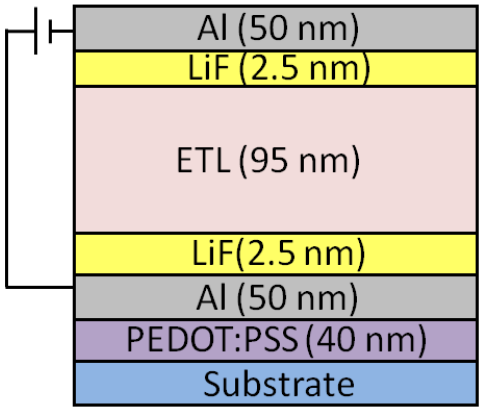


**Figure 4.3.** Device structure for electron-dominated devices.

The current density vs. voltage curves of these devices are shown in Figure 4.4, in which negative voltages and positive voltages correspond to electron injection from the bottom and top electrodes, respectively. The nearly symmetric current voltage characteristics demonstrate that the bottom Al/LiF electrode is comparable to the top Al/LiF electrode at injecting electrons into these ETLs. If the difficulty of producing high-performance inverted OLEDs is poor electron injection from bottom cathodes, these results indicate that that inverted OLEDs using bottom Al/LiF cathodes with ETLs other than $Alq_3$ could perform nearly as well as OLEDs using top Al/LiF cathodes.

It is also apparent that the electron current density of the devices with TpPyPB is greater than that of devices with TmPyPB. This higher current can be attributed partly to TpPyPB's larger EA of 3.0 eV compared to the EA of 2.7 eV of TmPyPB, leading to more efficient electron injection into TpPyPB. Additionally, the electron mobility of TpPyPB as measured by TOF ($7.9 \times 10^{-3}$ $cm^2$ $V^{-1}$ $s^{-1}$ at $6.1 \times 10^5$ V/cm) is significantly larger than that of TmPyPB ($1.0 \times 10^{-3}$ $cm^2$ $V^{-1}$ $s^{-1}$ at $6.4 \times 10^5$ V/cm), leading to better electron transport in TpPyPB [104].

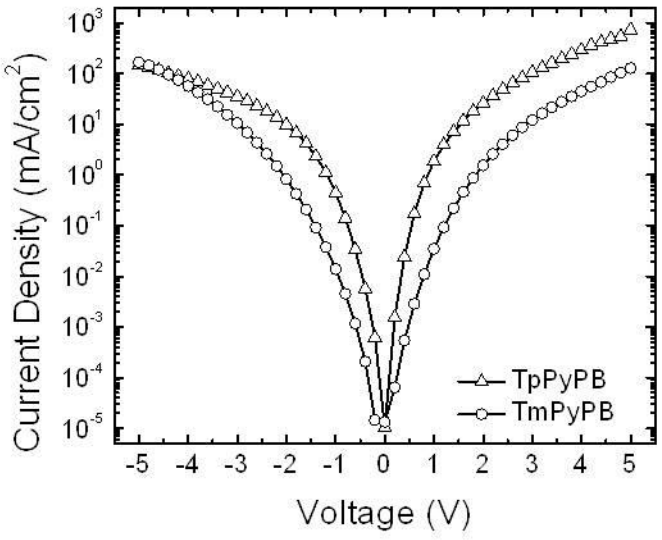


**Figure 4.4.** Current density vs. voltage characteristics of Al/LiF/TpPyPB or TmPyPB/LiF/Al electron-dominated devices. Electrons are injected from the top electrode for positive voltage values and from the bottom for negative voltage values.

It should be noted in passing that our group has also recently shown that the bottom Al/LiF cathode is highly sensitive to trace amounts of oxygen and water. In [105], electron-dominated devices were subjected to a vacuum break and subsequently exposed to the glovebox $N_2$ atmosphere ($O_2$ <0.1 ppm, $H_2O$ < 3.0 ppm) immediately after the bottom Al/LiF cathode was deposited. When electrons were injected from the bottom

cathode, the current density of the exposed devices was nearly four orders of magnitude lower than that in unexposed devices. We hypothesize that the Al/LiF cathode oxidizes when exposed to the trace amounts of $O_2$ and $H_2O$ present in the glovebox atmosphere. If an oxide forms, the insulating property of the oxide would reduce the ability of the cathode to inject electrons; moreover, an oxide could prevent a chemical reaction from occurring between the ternary Al/LiF/ETL system. The high sensitivity of the Al/LiF cathode to trace amounts of $O_2$ and $H_2O$ might explain why such cathodes have not been widely implemented successfully in inverted OLEDs.

# CHAPTER 5

# Green Inverted Top-Emitting OLEDs

Building on the results of the previous chapter, experimental results of highly efficient inverted top-emitting green electrophosphorescent OLEDs are now presented. A particular inverted architecture is chosen, and it is shown that in this architecture, the performance of the inverted OLED can be increased if the electron mobility value of the ETL material is increased given that the EAs of the ETL materials are the same. To place these results in the proper context, an inverted top-emitting OLED literature review is first given.

## 5.1 Inverted Top-Emitting OLED Literature Review

The first inverted top-emitting OLED was demonstrated in 1997 and consisted of vacuum-deposited organic materials [106]. The OLED contained a Mg:Al cathode and an $Alq_3$ emissive layer and exhibited an EQE of 0.30%. Next, Dobbertin *et al.* [107] made OLEDs with an Al cathode, an EIL of 4,7-diphenyl-1,10-phenathroline (BPhen) doped with Li, an ETL of undoped BPhen, and an emissive layer of $Alq_3$ doped with N,N'-diphenyl-substituted quinacridone (Ph-QAD). These devices exhibited a current efficiency of 4.2 cd/A and a power efficiency of 1.0 lm/W at 1,000 cd/m$^2$. Dobbertin *et al.* [108] demonstrated devices with a Mg/Au cathode and an $Alq_3$ emissive layer. Their current efficiency and power efficacy reached 3.9 cd/A and 0.7 lm/W, respectively, at a luminance of 1,500 cd/m$^2$. In all three of these early reports, the OLEDs contained anodes consisting of sputtered ITO. The authors recognized that sputtering ITO on top of

an OLED damaged the underlying organic layers, and they used various buffering materials on the organic layers to reduce this damage.

Previous groups have used EILs for interfacial doping and high-mobility ETLs to overcome the difficulty of delivering electrons into the emissive layer of inverted devices. Chen *et al.* [109] used a thin layer of $Cs_2CO_3$ on a bottom *n*-type Si cathode to enhance electron injection. $Alq_3$ is used as both the ETL and emissive layer, yielding a maximum current efficiency of is 1.5 cd/A at 100 cd/m$^2$. Meng *et al.* [110] used a Mg:Al/LiF cathode and an $Alq_3$ emissive layer to produce OLEDs with a maximum current efficiency of 3.7 cd/A at a luminance of 14,900 cd/m$^2$ and a maximum power efficiency of 0.8 lm/W. Wang *et al.* [111] compared OLEDs with Al cathodes and EILs of either PbO or LiF. The emissive layer used was $Alq_3$ doped with 10-(2-Benzothiazolyl)-2,3,6,7-tetrahydro-1,1,7,7-tetramethyl-1H,5H,11H (1)benzopyropyrano (6,7-8-I,j)quinolizin-11-one (C545T). The devices with PbO had a maximum current efficiency of 33.8 cd/A and a maximum power efficiency of 16.6 lm/W. The OLEDs with LiF had a maximum current efficiency of 22.9 cd/A and a maximum power efficiency of 7.3 lm/W. This same group also fabricated OLEDs with Al cathodes, an EIL of $PbO_2$, and emissive layers of $Alq_3$ doped with C545T [102]. The OLEDs had a maximum current efficiency of 31.6 cd/A and a power efficiency of 14.3 lm/W. Wang *et al.* [112] present a theoretical and experimental study of OLEDs with an Al/LiF cathode, an $Alq_3$ emissive layer, and a 2,9-dimethyl-4,7-diphenyl-1,10-phenanthroline (BCP) hole-blocking layer. The most efficient devices have a current efficiency of about 9 cd/A at about 100 cd/m$^2$. Ryu *et al.* [113] report on OLEDs with Mg/LiF cathodes and emissive layers consisting of bis(10-hydroxybenzo[h] quinolinato)beryllium ($Bebq_2$) doped with

tris(1-phenylisoquinoline)iridium ($Ir(piq)_3$). The most efficient device had a current efficacy of 10.3 cd/A at 1,000 cd/m$^2$. Hou *et al.* [81] present OLEDs with Al/LiF cathodes and emissive layers of $Alq_3$. The best performing device has a buffer layer of $MoO_3/C_{60}$ and a semitransparent Al anode. Their maximum EQE and power efficacy are 1.37% and 1.12 lm/W, respectively. Recently, Zhang *et al.* [114] made OLEDs with a Ag (100 nm)/Al (2 nm) bilayer cathode, LiF EIL and an $Alq_3$ emissive layer. The devices had a current efficiency of 5.9 cd/A.

### 5.2 State-of-the-Art in Inverted Top-Emitting OLEDs

The highest current efficiencies previously reported for inverted top-emitting OLEDs are from a report by Kroger *et al.* [80]. The cathode is Mg:Al, the EIL is BPhen:Li, the ETL is 1,3,5-tri(phenyl-2-benzimidazole)-benzene (TPBi), and emission takes place from two separate emissive layers: one is TBPi: tris(2-phenylpyridine)iridium(III) ($Ir(ppy)_3$) and the other is 4,4',4"-tris(carbazol-9-yl)-triphenylamine (TCTA):$Ir(ppy)_3$. For these devices, pentacene is used as an upper protective layer and spin-cast PEDOT:PSS with sputtered ITO is used as the anode. The maximum current efficiency reaches 55.4 cd/A at 140 cd/m$^2$ and the maximum power efficiency is 17.2 lm/W at 50 cd/m$^2$.

The highest EQEs published for inverted top-emitting OLEDs are from red-orange devices from Thomschke *et al.* [115, 116]. In [115] the authors fabricate a doped *n*-i-*p* OLED with an emissive layer of N,N'-di(naphthalene-1-yl)-N,N'-diphenyl-benzidine (α-NPD) doped with the red-orange phosphorescent emitter irdium(III)bis(2-methyldibenzo-[f,h]quinoxaline)(acetylacetonate) [$Ir(MDQ)_2(acac)$]. They contain a Ag cathode, a layer of BPhen:Cs:Ag as the EIL, and BPhen co-doped with Cs as their ETL.

They exhibit a maximum EQE of 15% at about 1,000 cd/m$^2$ after thermal annealing. In [116], OLEDs of a similar structure are presented with a maximum EQE of about 19% at about 500 cd/m$^2$.

The most efficient green electrophosphorescent inverted top-emitting OLEDs reported contains an Al cathode, a $Cs_2CO_3$ EIL, a BPhen ETL, and an emissive layer of 4,4'-bis(N-carbazolyl)-1,1'-biphenyl (CBP) doped with $Ir(ppy)_3$ [117]. When a ZnS optical outcoupling layer is added on its semitransparent Ag anode, an EQE of about 12% and a power efficacy of about 40 lm/W was attained at a luminance of 100 cd/m$^2$.

### 5.3 Development of the Green Inverted Top-Emitting OLED Architecture

As previously discussed, modern small-molecule OLEDs contain multiple layers of metal, inorganic material, and organic semiconductor material with each layer performing a specific function in order to decrease the voltage required to drive the OLED and to increase its efficiency. An example of such a multilayer conventional bottom-emitting OLED is described by Baldo *et al*. in one of the earliest papers on electrophosphorescent OLEDs [65]. It consisted of an ITO anode, a 40 nm-thick HTL of α-NPD, an emissive layer of $Ir(ppy)_3$ doped within CBP at a mass ratio of 6%, a thin layer of 6 nm of 2,9-dimethyl-4,7-diphenyl-1,10-phenanthroline (BCP) to confine excitons to the emissive layer, an ETL of 20 nm of $Alq_3$, and a 100 nm-thick Mg:Ag cathode. Chemical diagrams of these commonly-used organic materials are shown in Figure 5.1. This device exhibited an EQE of 7.5%, a current efficacy of 26 cd/A, and a power efficacy of 19 lm/W at 100 cd/m$^2$. This device exhibited an EQE of 7.5%, a current efficacy of 26 cd/A, and a power efficacy of 19 lm/W at 100 cd/m$^2$.

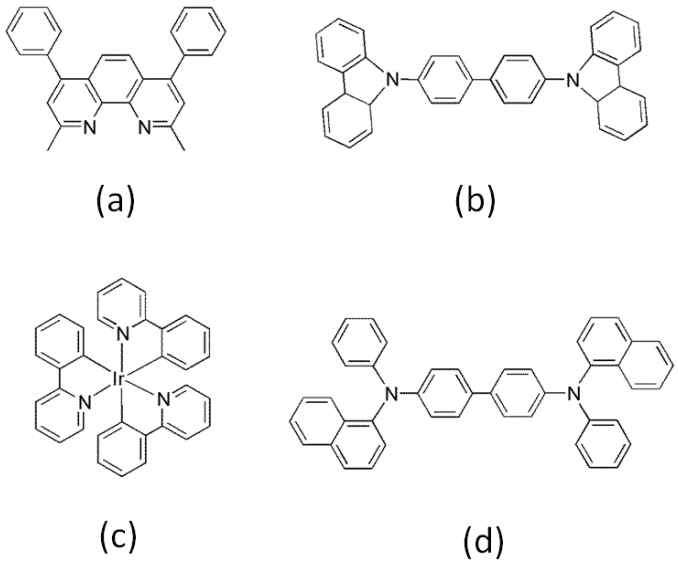


**Figure 5.1.** Chemical structures for (a) BCP (b) CBP (c) $Ir(ppy)_3$ and (d) α-NPD.

The efficiency of this conventional bottom-emitting OLED can be improved by making some modifications. It is well known that the barrier to hole injection from an ITO anode can be reduced by treating the ITO with $O_2$ plasma, which increases its work function from 4.2 eV to 4.7 eV [118]. The modified ITO work function of 4.7 eV still results in an injection barrier to many HTL materials, but the work function can be further increased by coating it with a conductive polymer with a higher work function, such as PEDOT:PSS [119]. The conductive polymer layer also smoothes the surface of the ITO and may act to prevent the diffusion of ions from the ITO into neighboring organic, enhancing the operational lifetime of the device [61, 120]. The process of electron injection can also be enhanced by replacing the Mg:Ag cathode with an Al/LiF cathode and by replacing the $Alq_3$ ETL with an ETL of BCP. Finally, the layer thicknesses can be optimized through experimentation.

An improved device structure is shown in Figure 5.2. It has an anode of 140 nm of ITO coated with a 40 nm of PEDOT:PSS, an HTL of 35 nm of α-NPD, an EML composed of 20 nm of CBP doped with $Ir(ppy)_3$ at a volume percentage of 6%, an ETL of 40 nm of BCP, a 2.5 nm EIL of LiF, and a cathode consisting of 50 nm of Al and 100 nm of Ag. The silver is used to supplement the thickness of the cathode to aid in contacting the OLED to electrical pins for measurement.

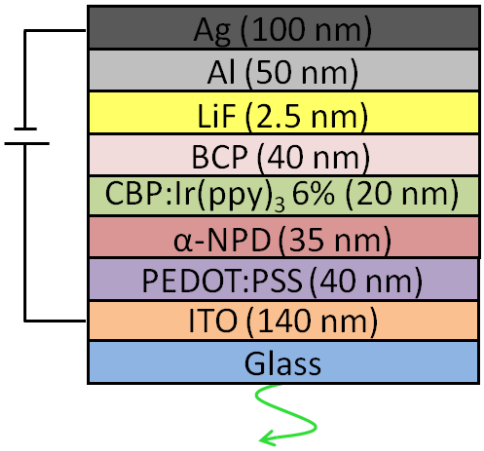


**Figure 5.2.** An optimized, highly efficient conventional bottom-emitting electrophosphorescent OLED.

Figure 5.3 shows the current density vs. voltage characteristics of this device, and Figure 5.4 shows the luminance vs. voltage and the EQE vs. voltage. These devices exhibit a low turn-on voltage (defined as the first voltage value resulting in a luminance value of more than 10 $cd/m^2$) of only 3.1 V and a high EQE of about 18.7% at a luminance of 175 $cd/m^2$. Figure 5.5 contains a plot of the current efficacy vs. luminance showing that the current efficacy of this optimized device has been increased to 67 cd/A at 175 $cd/m^2$. Figure 5.6 contains the EL spectrum taken in the direction of the surface for this device, which agrees well with other bottom-emitting OLEDs containing $Ir(ppy)_3$, and results in the CIE coordinates of (0.35, 0.61) [65].

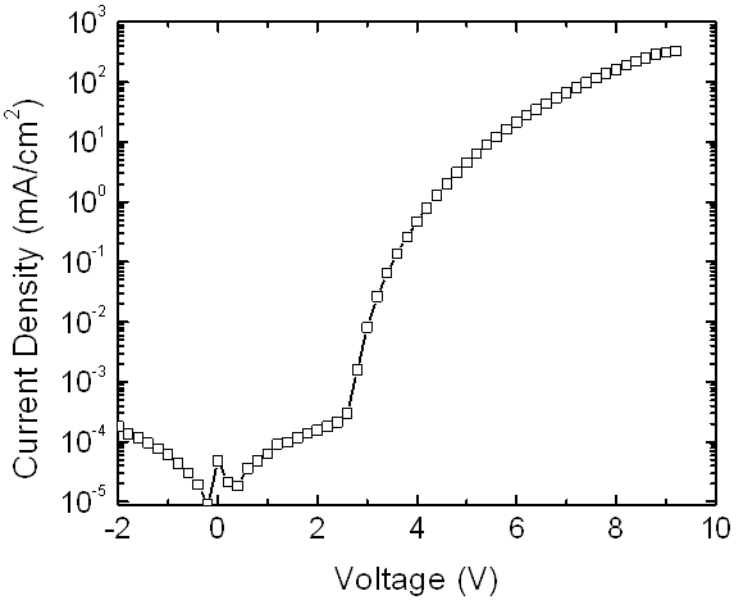


**Figure 5.3.** Current density vs. voltage curve for OLED with device structure: Glass/ITO/PEDOT:PSS/α-NPD/ CBP:Ir(ppy)$_3$/BCP/LiF/Al.

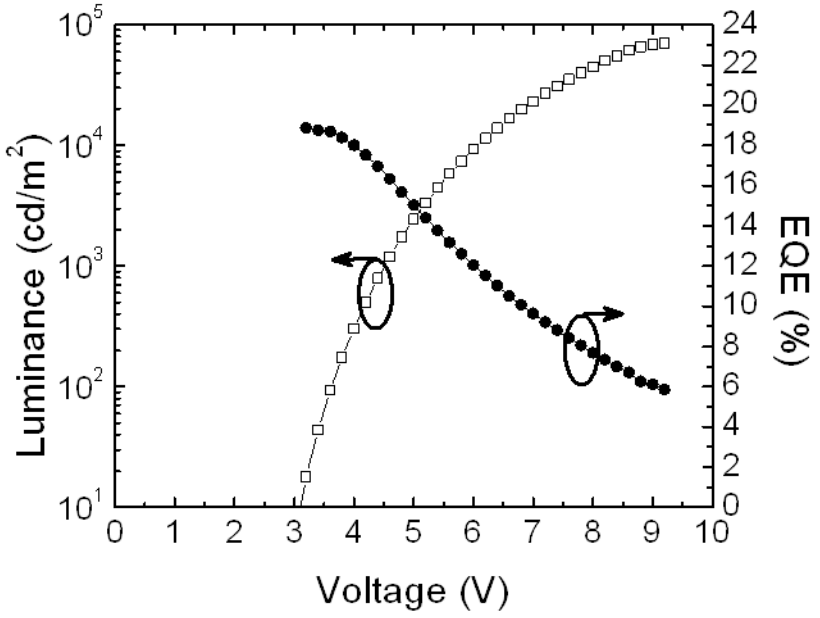


**Figure 5.4.** Luminance vs. voltage and EQE vs. V curves for OLED with device structure: Glass/ITO/PEDOT:PSS/α-NPD/ CBP:Ir(ppy)$_3$/BCP/LiF/Al.

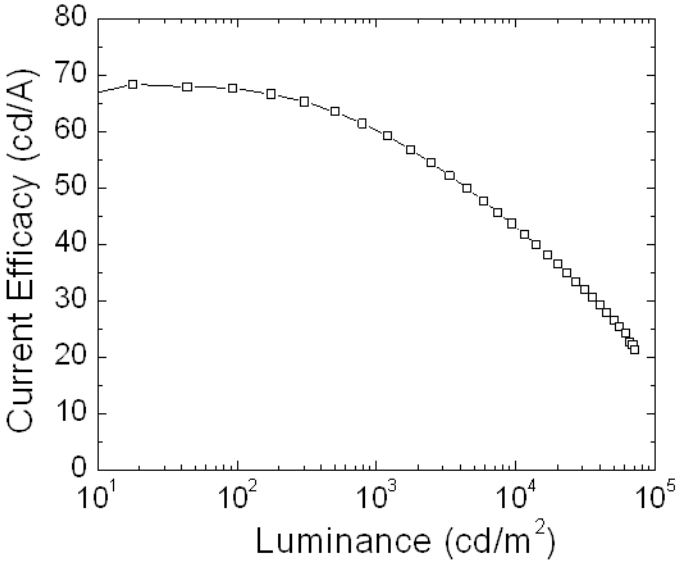


**Figure 5.5.** Current efficacy vs. luminance curve for OLED with device structure: Glass/ITO/PEDOT:PSS/α-NPD/ CBP:Ir(ppy)$_3$/BCP/LiF/Al.

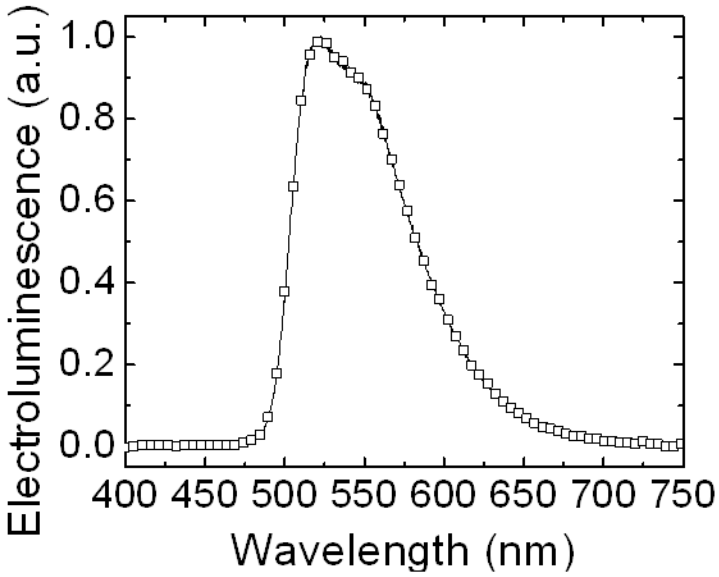


**Figure 5.6.** Electroluminescence spectrum of an OLED with device structure: Glass/ITO/PEDOT:PSS/α-NPD/ CBP:Ir(ppy)$_3$/BCP/LiF/Al taken in the direction of the surface normal of OLED.

By inverting this structure, efficient inverted OLEDs can be fabricated using an ETL of BCP with a bottom Al/LiF cathode. In fact, this is also true of other ETLs consisting of materials with high EA values and high electron mobility values. To illustrate this, a general inverted top-emitting green electrophosphorescent device structure is used (see Figure 5.7) where the ETL is chosen to consist of 40 nm of one of the following materials: BCP, BPhen, or TpPyPB. Table 3 contains the EA and electron mobility values (as measured by TOF) of the ETL materials used and of $Alq_3$ for comparison. The EML in these devices consists of 20 nm of CBP doped with $Ir(ppy)_3$ at a volume percentage of 6%, and the HTL is composed of 35 nm of α-NPD.

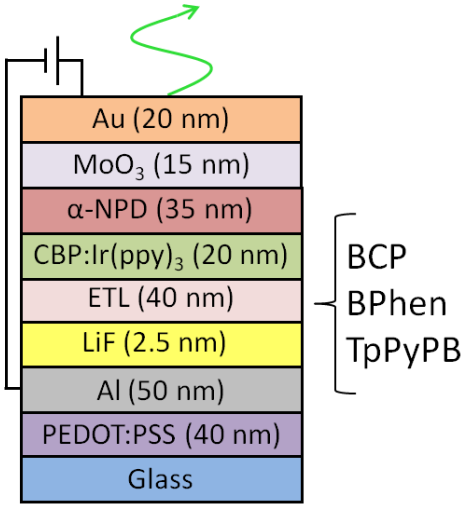


**Figure 5.7.** General inverted top-emitting device structure with different ETLs.

**Table 3.** EA and electron mobility values (determined by TOF measurements) for a variety of ETL materials.

| Material | EA (eV) | Mobility [$cm^2/Vs$] | References |
|---|---|---|---|
| $Alq_3$ | 3.0 | $7.2 \times 10^{-6}$ | [104, 121] |
| BCP | 3.0 | $5.6 \times 10^{-6}$ | [121, 122] |
| BPhen | 3.0 | $5.2 \times 10^{-4}$ | [123, 124] |
| TpPyPB | 3.0 | $7.9 \times 10^{-3}$ | [104] |

To make an inverted top-emitting OLED, the anode must be on the top of the device, and it must be semitransparent. Using the technique of radio frequency magnetron sputtering, it is possible to deposit a transparent top anode of ITO [106]. However, this technique damages the underlying fragile organic material and results in the degradation of the device. For the device in Figure 5.7, a design choice is made to deposit a 15 nm-thick layer of $MoO_3$ as an HIL with a semitransparent 20 nm-thick Au anode. Transition-metal oxides, such as $WO_3$, $V_2O_5$, and $MoO_3$ have been used to make very effective HILs. They provide the additional benefits of being stable, low-cost, and easily processed through VTE [125]. When deposited on an anode, $MoO_3$ has been shown to strongly modify the anode's work function. For instance, the deposition of 1.6 nm of $MoO_3$ on ITO has been shown to increase the work function of ITO from 4.4 eV to nearly 6.9 eV [126]. This is because the EA of $MoO_3$ is 6.7 eV and the material is strongly *n*-type, with its Fermi level very close to its conduction band. When $MoO_3$ is used in conjunction with α-NPD, the Fermi level gets pinned to about 0.6 eV above the HOMO level of α-NPD. Thus, when $MoO_3$ is used as an HIL, hole injection proceeds by electron extraction from the HOMO level of the hole-transport material [126].

A thin layer of Au is chosen as the anode for both its high work function (5.1 eV [94]) and the reduced damage depositing it by VTE causes when compared to depositing ITO by radio frequency magnetron sputtering. The thickness is chosen to be 20 nm to simultaneously provide sufficiently high conductivity and high transmittance. The transmittance of $MoO_3$ and Au on glass is shown in Figure 5.8. Across the visible wavelengths, the glass substrate has a high transmittance of 95% and a 15 nm $MoO_3$ layer

on glass maintains a transmittance of about 90%. When 20 nm of Au is deposited on the $MoO_3$, the transmittance drops below 50% in the blue wavelengths.

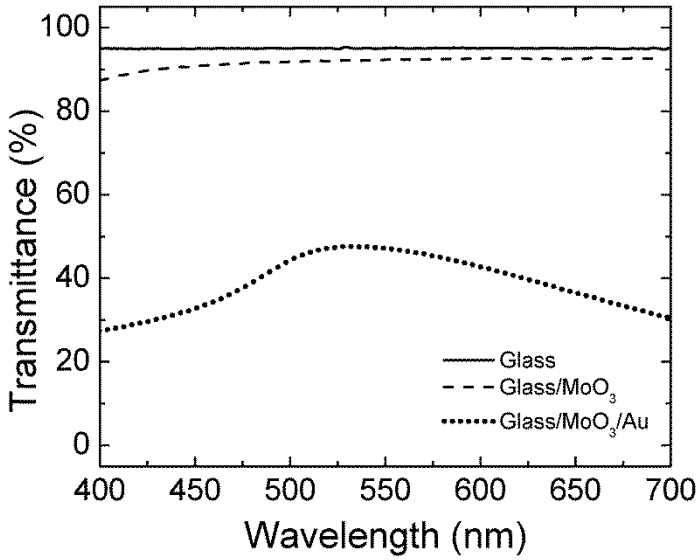


**Figure 5.8.** Transmission of the glass substrate, Glass/MoO3 (15 nm), and Glass/$MoO_3$ (15 nm)/Au (20 nm).

The use of a thin semitransparent layer of gold as the anode leads to the formation of a microcavity between it and the reflective Al cathode. Microcavity OLEDs exhibit microcavity effects such as spectral narrowing and spectral shifting [127].

### 5.4 Green Inverted OLED Results and Discussion

The current density vs. voltage, luminance vs. voltage, and current efficacy vs. luminance characteristics for the devices in Figure 5.7 are shown in Figure 5.9, Figure 5.10, and Figure 5.11, respectively. All of these inverted devices show high performance, with turn on voltages below 5 V and current efficacies above 30 cd/A for luminance values up to 1000 cd/$m^2$. The performance of these devices increases as the electron mobility values of the ETL material increases. This trend is consistent with the traditionally held belief that the major factor limiting the performance of inverted OLEDs

is carrier imbalanced due to an insufficient number of electrons being delivered to the EL relative to the number of holes. The device with the lowest turn-on voltage and the highest current efficacy up to luminance values of about 500 cd/m$^2$ has TpPyPB as the ETL. This device has a low turn-on voltage of 3.6 V and current efficacies of 47.6 cd/A at 122.4 cd/m$^2$ and 33.5 cd/A at 1,167.1 cd/m$^2$.

Here, measurements of EQE and power efficacy have not been reported. In conventional bottom-emitting OLEDs these values are typically calculated from a single measurement of the luminance at the surface normal of the OLED with the assumption that the device is a Lambertian emitter. However, microcavity devices cannot simply be assumed to be Lambertian emitters [79, 128]. Figure 5.12 contains the EL spectrum taken at the direction of the surface normal for the OLED with an ETL of BCP. It has CIE coordinates of (0.32, 0.59). When compared to the spectrum of the conventional bottom-emitting device in Figure 5.6, the peak of the inverted top-emitting OLED's spectrum has shifted from 523 nm to 547 nm which can be attributed to resonance effects within the microcavity [127].

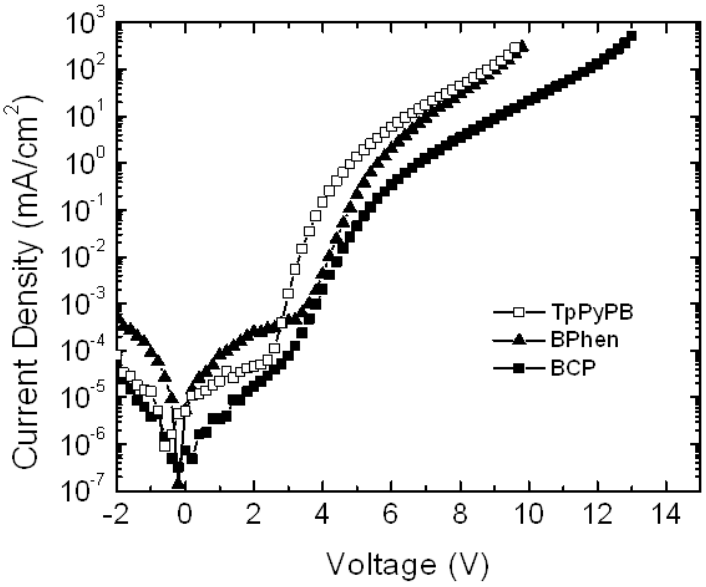


**Figure 5.9.** Current density vs. voltage curves for OLEDs with the general inverted top-emitting device structure: Glass/PEDOT:PSS/Al/LiF/ETL/CBP:Ir(ppy)$_3$/α-NPD/$MoO_3$/Au.

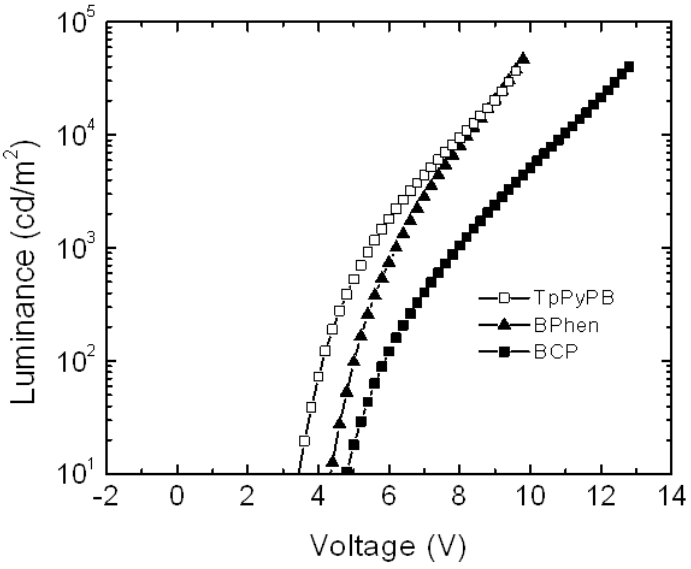


**Figure 5.10.** Luminance vs. voltage for OLEDs with the general inverted top-emitting device structure: Glass/PEDOT:PSS/Al/LiF/ETL/CBP:Ir(ppy)$_3$/α-NPD/$MoO_3$/Au.

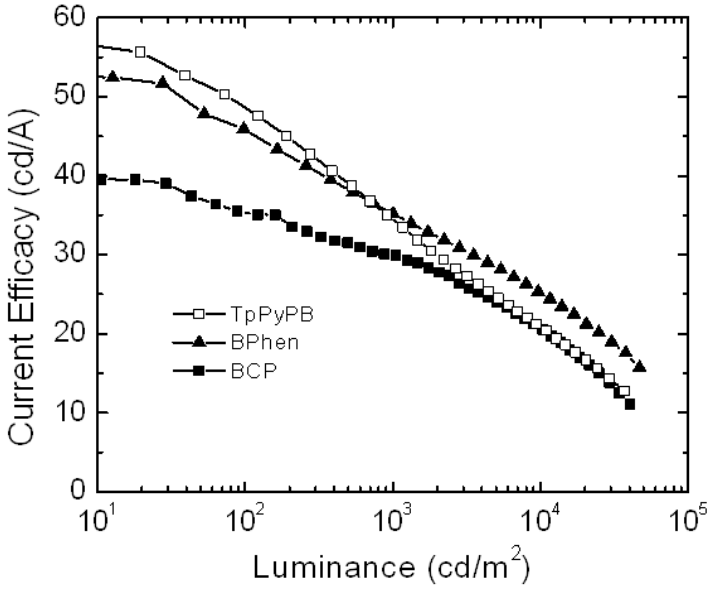


**Figure 5.11.** Current efficacy vs. luminance for OLEDs with the general inverted top-emitting device structure: Glass/PEDOT:PSS/Al/LiF/ETL/CBP:Ir(ppy)$_3$/α-NPD/$MoO_3$/Au.

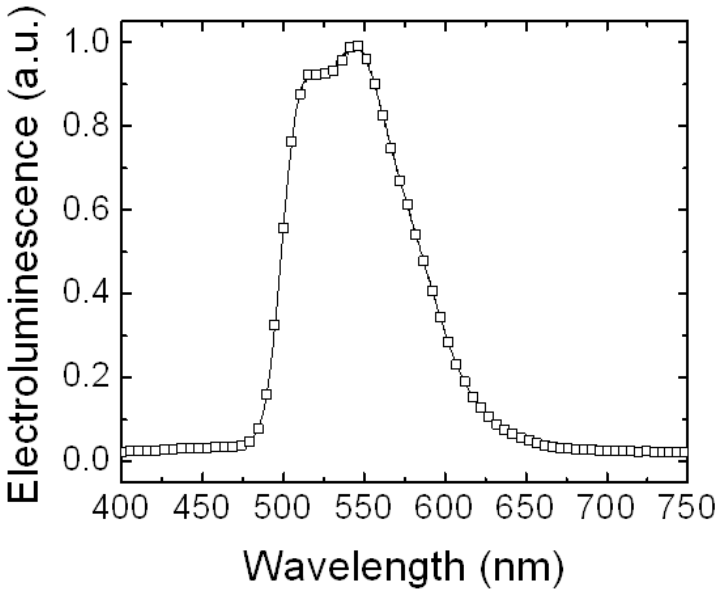


**Figure 5.12.** Electroluminescence spectrum of OLED with device structure: Glass/PEDOT:PSS/Al/LiF/BCP/CBP:Ir(ppy)$_3$/α-NPD/$MoO_3$/Au.

It should be noted in passing that these inverted top-emitting green electrophosphorescent OLEDs were subsequently optimized by using an ETL of TpPyPB together with an HTL of CBP [105]. It is believed that the semitransparent $MoO_3$/Au anode injects holes very effectively into the HOMO level of the CBP HTL (corresponding to an IE of 6.3 eV [129]). With these devices, a high current efficacy of 60.6 cd/A was achieved at a luminance of 1,073 cd/m$^2$, and when an additional optical outcoupling layer of 120 nm of α-NPD was deposited on top of the anode, the current efficacy increased to 92.5 cd/A at 1,300 cd/m$^2$. The optical outcoupling layer increases the efficiency of the device by modifying its optical structure and increasing the amount of light extracted from the device [82]. These OLEDs were demonstrated on both glass and flexible polyethersulfone (PES) substrates.

# CHAPTER 6

# Blue Inverted Top-Emitting OLEDs

This chapter presents the experimental results of highly efficient inverted top-emitting blue electrophosphorescent OLEDs. To place the significance and impact of our research into a broader perspective, the challenges of producing OLEDs with blue emission are first reviewed. Next, the prior art of conventional and inverted blue OLEDs is reviewed. Then, using the general inverted OLED developed in the previous chapter, different blue inverted top-emitting OLEDs are presented along with the design rationale that led to their eventual optimization.

## 6.1 Challenges of Blue Emission

In both conventional and inverted architectures, there is a scarcity of highly efficient blue OLEDs with long lifetimes. The first multilayer blue fluorescent OLEDs were fabricated by Adachi *et al.* in 1990 and achieved a luminance of 700 cd/m$^2$ with a power efficacy of 0.22 lm/W at a voltage of 10 V [130]. Highly efficient blue electrophosphorescent OLEDs are difficult to produce for two reasons. First, it is difficult to synthesize blue phosphors that are stable and have high luminescent quantum yield. Second, the high triplet energy of blue phosphors requires that the host also have a high triplet energy [19]. Hosts with high triplet energies have large bandgaps, and these host often have unfavorable transport level alignment with the adjacent transport layers, leading to devices with low efficiencies [131]. In 2001, the first blue electrophosphorescent OLEDs were demonstrated by Adachi *et al.*, and they had a maximum EQE of 5.7% and a power efficacy of 6.3 lm/W [131]. The low efficiency was in part due to the devices relying on endothermic energy transfer between the CBP host

and the iridium(III)bi[(4,6-di-fluorophenyl)-pyridinato-N,$C^{2'}$]picolinate (FIrpic) dopant. Later, the EQE and power efficacy of these devices were improved to 7.5% and 8.9 lm/W by switching to a higher triplet energy host, N,N'-dicarbazolyl-3,5-benzene (mCP), allowing for exothermic energy transfer to the FIrpic dopant [132].

### 6.2 State-of-the-Art of Blue Conventional and Inverted OLEDs

At the time of writing of this thesis, state-of-the-art bottom-emitting blue electrophosphorescent OLEDs in the conventional architecture have achieved an EQE as high as 25.6%, a power efficacy of 27.2 lm/W, and a current efficacy of 44 cd/A at a luminance of 100 cd/$m^2$ [133]. Reports of blue OLEDs in the inverted architecture are considerably scarcer [134-136]. The most efficient inverted blue electrophosphorescent OLEDs are bottom-emitting and partially solution-processed. They have a maximum current efficacy of 34.3 cd/A, EQE 15.2%, and power efficacy of 20.5 lm/W [134]. All-vacuum evaporated inverted bottom-emitting blue electrophosphorescent OLEDs have achieved a maximum current efficacy of 16.5 cd/A and an EQE of 8.2% [135]. The most efficient blue inverted top-emitting OLED reported has a fluorescent emitter and exhibits a maximum current efficacy of 9 cd/A [136]**.**

### 6.3 Design Choices

After demonstrating that bottom Al/LiF cathodes can be used to produce highly efficient inverted top-emitting green electrophosphorescent OLEDs, we attempted to design and optimize inverted top-emitting blue electrophosphorescent OLEDs. Prior to our work [137], there were no reports to the best of our knowledge on blue electrophosphorescent OLEDs with an inverted top-emitting geometry.

Here, results are presented on two inverted top-emitting blue electrophosphorescent OLED devices differing only in the material used in their ETLs. The ETL consists of 40 nm of either TpPyPB or TmPyPB. These materials were used in the electron-dominated devices in section 4.3 to show that bottom Al/LiF cathodes could inject electrons nearly as effectively as top Al/LiF cathodes. The EML has a total thickness of 20 nm and is composed of mCP coevaporated with FIrpic at a volume percentage of 12%. Chemical diagrams of mCP and FIrpic are shown in Figure 6.1. Here a design choice is made to use mCP as the host instead of CBP. Using mCP as the host material allows for exothermic energy transfer to the FIrpic guest, because the FIrpic triplet energy level is estimated at 2.62 eV [131] and the triplet energy level of mCP is 2.90 eV [132]. The value of the triplet energy of CBP is only 2.56 eV [131], and is thus too low to allow CBP to be used as a host for exothermic energy transfer from host to guest. However, an HTL of 35 nm of CBP is still used as it has been shown that $MoO_3$/Au anode injects holes very effectively into the HOMO level (IE of 6.3 eV [129]) of CBP [105]. The resulting optimized device structure is shown in Figure 6.2.

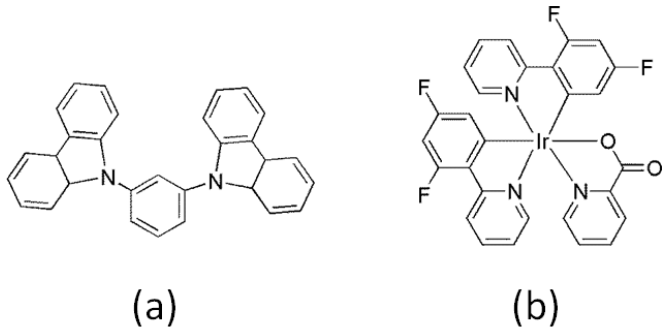


**Figure 6.1.** Chemical structures for (a) mCP and (b) FIrpic.

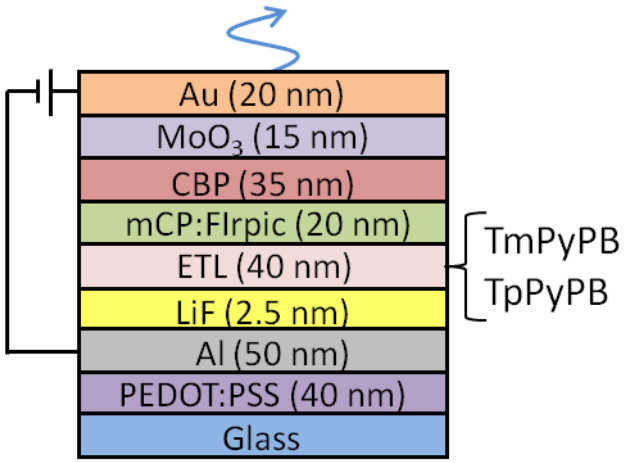


**Figure 6.2.** Inverted top-emitting blue electrophosphorescent OLED structure where either TpPyPB or TmPyPB is used as the ETL material.

### 6.4 Results and Discussion

Figure 6.3 shows a plot of the current density vs. voltage of the OLEDs, and Figure 6.4 shows the luminance and current efficacy vs. voltage. The performance of these devices has been verified in separate batches with multiple OLEDs per batch. The average performance and standard deviation of the OLEDs from a typical batch are contained in Table 4. The devices with TmPyPB have a much higher current efficacy than the devices with TpPyPB. Devices with TpPyPB had a maximum current efficacy of 7.3 cd/A at 20.2 cd/m$^2$, and an average current efficacy of 5.2 cd/A at 100 cd/m$^2$, while devices with TmPyPB had a maximum current efficacy of 43.1 cd/A at 36.8 cd/m$^2$, and an average current efficacy of 39.1 cd/A at 100 cd/m$^2$. The TmPyPB devices represent a significant improvement over previously reported blue inverted OLEDs in both the bottom-emitting and top-emitting architectures.

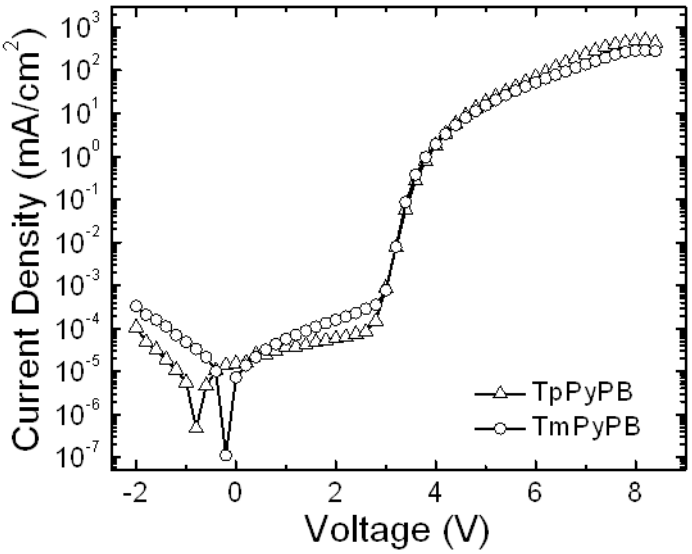


**Figure 6.3.** Current density vs. voltage curves for OLEDs with device structure: Substrate/PEDOT:PSS/Al/LiF/TpPyPB or TmPyPB/mCP:FIrpic/CBP/$MoO_3$/Au.

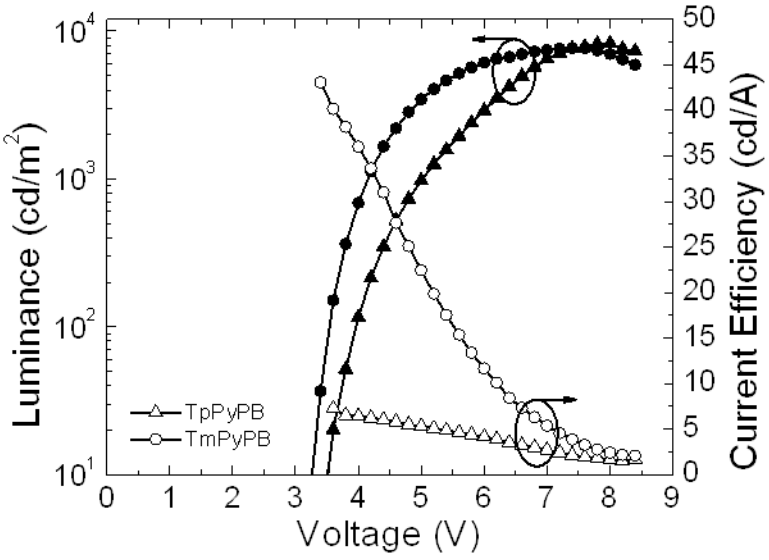


**Figure 6.4.** Luminance and current efficacy vs. voltage of OLEDs with device structure: Substrate/PEDOT:PSS/Al/LiF/TpPyPB or TmPyPB/mCP:FIrpic/CBP/$MoO_3$/Au.

**Table 4.** Average performance with standard deviation of OLEDs with device structure: Substrate/PEDOT:PSS/Al/LiF/TpPyPB or TmPyPB/mCP:FIrpic/CBP/$MoO_3$/Au..

| ETL | Luminance [cd/m$^2$] | Voltage [V] | Current Density [mA/cm$^2$] | Current Efficacy [cd/A] |
|---|---|---|---|---|
| **TpPyPB** (28 devices) | 100 | 4.0 (± 0.4) | 2.69 (± 0.78) | 5.2 (± 1.2) |
| | 1,000 | 5.0 (± 0.2) | 33.04 (± 6.72) | 3.6 (± 0.7) |
| **TmPyPB** (22 devices) | 100 | 3.6 (± 0.1) | 0.36 (± 0.04) | 39.1 (± 2.1) |
| | 1,000 | 4.2 (± 0.1) | 3.49 (± 0.29) | 32.0 (± 0.9) |

There are two possible reasons for the superior performance of the devices containing TmPyPB. One likely reason is TmPyPB's more favorable triplet energy. To minimize exciton transfer to the electron transport material and subsequent non-radiative decay, the triplet energy of the electron transport material should be higher than the triplet energy of the phosphorescent dopant. The triplet energy levels of TpPyPB, TmPyPB, and FIrpic are 2.57 eV, 2.78 eV, and 2.65 eV, respectively [104, 132]. Consequently, TmPyPB is more effective than TpPyPB at preventing excitons transfer to the ETL, leading to better performance. Another possible reason for the difference in performance of devices with TmPyPB is altered charge balance in the OLEDs. Decreasing electron injection and transport by using TmPyPB as an ETL likely leads to a different charge balance in these devices, as is supported by the single-carrier device data shown in Figure 4.4.

The angular electroluminescent spectra of an OLED with TmPyPB are shown in Figure 6.5. The spectra are taken at 20° increments from the surface normal and are normalized to the maximum intensity of the spectrum at normal viewing. Despite the microcavity formed between the Al cathode and Au anode, common microcavity effects such as spectral narrowing and spectral shifting [127] are not apparent with increasing

angle. Therefore, the color of the OLED does not substantially change with the angle-of-view. The CIE coordinates are (0.24, 0.44) at 0° and shift to (0.19, 0.45) at 60°.

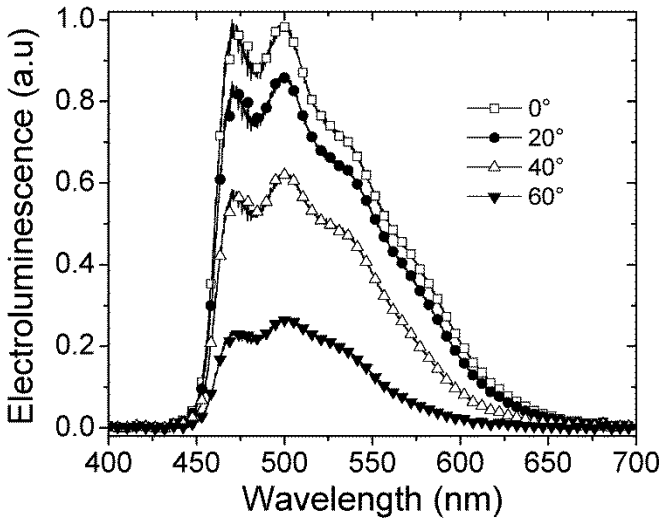


**Figure 6.5.** EL intensity of an OLED with device structure: Substrate/PEDOT:PSS/Al/LiF/TmPyPB/mCP:FIrpic/CBP/$MoO_3$/Au.

# CHAPTER 7

# STACKED INVERTED TOP-EMITTING OLEDs

## 7.1 Introduction

The OLEDs previously presented in this work are known as single-unit OLEDs because they contain a single emissive unit. This chapter explains the concept of a stacked OLED, which contains several vertically-stacked emissive units, and describes the advantages that they offer over single-unit OLEDs. Previously published state-of-the-art stacked OLED results are discussed; however, all of the stacked OLEDs previously reported are of the conventional bottom-emitting variety. To the best of our knowledge, there have been no previous reports in the scientific literature of inverted top-emitting stacked OLEDs, despite the fact that such an OLED would offer some important advantages over conventional bottom-emitting stacked OLEDs. Here, by expanding the art developed in the previous chapters, the first stacked inverted top-emitting OLEDs are demonstrated, and their performance is found superior to any two-unit stacked OLED previously reported.

## 7.2 Single-Unit vs. Stacked OLEDs

In a stacked OLED, separate light-emitting units (LEUs), each consisting of an ETL/EML/HTL structure (See Figure 7.1), are vertically stacked and connected together by connecting units (CUs). Free charges are generated by the CUs and injected into the neighboring LEUs. Because free charges are generated at each CU in the stacked OLED, a single electron injected into the cathode of an *N*-unit stacked OLED can result in the production of *N* photons. Thus, at a given current density, stacked OLEDs have an *N*-fold

enhancement in luminance over a single-unit OLED and an enhanced operational lifetime at a given luminance, because the same level of luminance can be achieved at a lower current density and thermal degradation that leads to device failure scales with the current density [32]. Figure 7.2 shows a single-unit OLED and a stacked OLED; at twice the voltage, the stacked OLED produces twice the luminance of the single-unit OLED at the same current density.

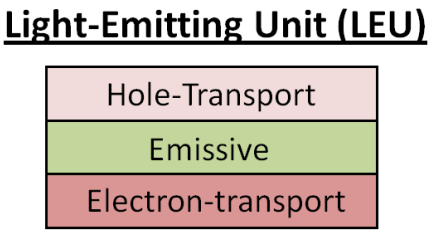


**Figure 7.1.** Light-emitting unit consisting of a HTL, EL, and ETL.

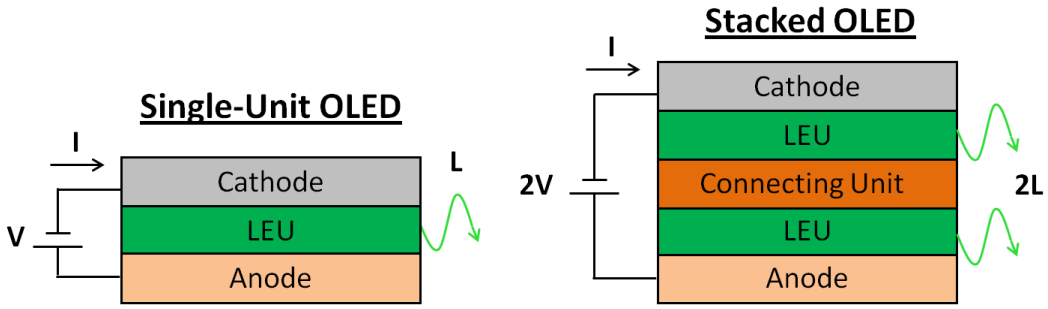


**Figure 7.2.** A single-unit OLED vs. a stacked OLED.

Stacked OLEDs possess other advantages over single-unit OLEDs. They can be operated at higher efficiencies, because at any given luminance for the overall stack, each LEU suffers from less efficiency roll-off as compared to a single-unit device [138]. Also, the color of the light generated by the independent emissive units within the stack can be conveniently chosen to reduce the complexity of color mixing. Color mixing can be used

to produce stacked white OLEDs [139]. In fact, stacked OLEDs have been widely used for white OLED lighting panels because they offer a solution to many of the problems in wide-area OLED applications. The greater overall thickness of the stack results in less shorting as well as a reduced horizontal-resistance effect from the transparent electrode [18].

### 7.3 State-of-the-Art Stacked OLEDs

Many different bottom- and top-emitting stacked OLEDs in the conventional architecture have been previously reported [140-142]. The highest current efficacy reported to date for a two-unit stacked OLED is 200 cd/A (at a luminance of about 500 $cd/m^2$), and it has a conventional bottom-emitting structure [143]. This device uses two luminance-enhancing techniques. The first is the use of a stacked architecture, and the second is the use of a well-designed microcavity consistent with resonant conditions. The combination of these two techniques provides a five-fold enhancement in luminance over the constituent single-unit OLEDs. It has doped transport layers, LEUs containing $Ir(ppy)_3$, and a CU consisting of α-NPD:$F_4$-TCNQ/BPhen:Cs, forming a *p*-*n* junction.

### 7.4 Connecting-Units

The CU plays a critical role in the operation of stacked OLEDs. Many methods have been used to form CUs. One is the use of ITO as an intermediate electrode to connect the lower and upper LEUs, but sputtering ITO damages the underlying fragile organic materials. Another approach is to use two adjacent layers, consisting of an electron-acceptor and an electron donor, to lead to the generation of free charges at their interface. The operation of such an interface is graphically depicted in Figure 7.3. If the EA of the acceptor is sufficiently high such that its LUMO level aligns well with the

HOMO level of the electron donor, under bias, electrons from the donor's occupied HOMO level can be transferred to the unoccupied LUMO of the acceptor. The resulting free electron and hole can migrate under the influence of the electric field and be injected into the neighboring LEUs [138].

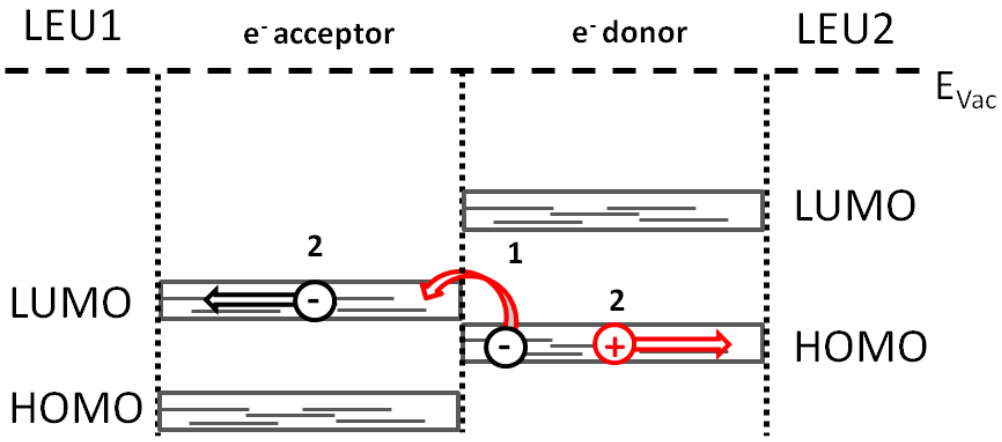


**Figure 7.3.** The operation of a CU consisting of an electron acceptor and an electron donor.

Many different material combinations have been used in two-layer CUs. Electron-accepting materials include metal-oxides such as $V_2O_5$ [144], $MoO_3$ [145], and $WO_3$ [146], as well as hole-transport materials doped with *p*-type dopants [147, 148]. The electron-donating materials used are typically electron transport materials with *n*-type dopants [144-149]. Of particular interest to this work is the recent use by Chiba *et al.* of a CU consisting of 1,4,5,8,9,11-hexaazatriphenylene hexacarbonitrile (HAT-CN) and 1,1-bis-(4-bis(4-tolyl)-aminophenyl)cyclohexene (TAPC) to make highly efficient stacked OLEDs [138]. The chemical structures of HAT-CN and TAPC are shown in Figure 7.4. HAT-CN is an electron acceptor with a large EA value comparable to the IE of many common HTLs. Reported values for the EA of HAT-CN range from 4.4 eV [138] to 6.0

eV [150], and the ionization potential of TAPC is 5.4 eV [151]. Thus, it is believed that when these materials are used in the CU of a stacked OLED, there is sufficient energy-level alignment for efficient electron transfer between the HOMO level of TAPC to the LUMO level of HAT-CN upon the application of an electric field [138].

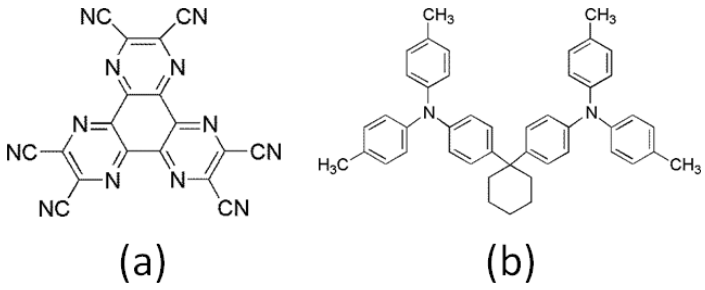


**Figure 7.4.** Chemical structures for (a) HATCN and (b) TAPC.

### 7.5 Stacked Green Inverted Top-Emitting OLEDs

Stacked inverted top-emitting were designed using the previously presented single-unit inverted top-emitting OLEDs as building blocks. Single-unit OLEDs were also fabricated in order to compare their performance to that of the stacked OLEDs.

The device structures of the single-unit and double-unit OLEDs are shown in Figure 7.5a and Figure 7.5b, respectively. Some double-unit OLEDs had an additional optical outcoupling layer consisting of 100 nm of α-NPD deposited upon their semitransparent Au anode (Figure 7.5c).

A CU consisting of HAT-CN/TAPC was chosen for a few reasons. First, it has been demonstrated that the HAT-CN/TAPC leads to an efficient charge-generation interface in stacked OLEDs [138]. Second, these two materials are undoped, processable using VTE, and highly transparent over visible wavelengths. In addition, thin interlayers of Al/LiF are also used in the CU to enhance electron injection into the top LEU,

lowering the energetic barrier that would otherwise exist between the LUMO level of TpPyPB (3.04 eV [104]) and the LUMO level of HAT-CN.

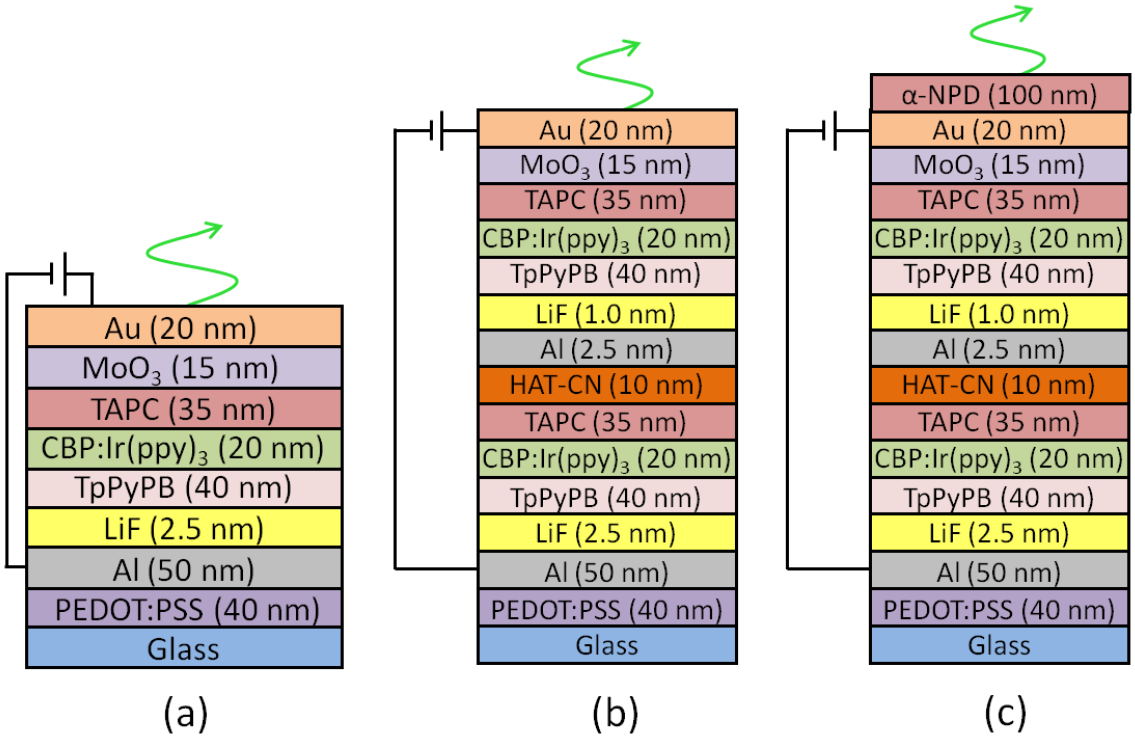


**Figure 7.5.** Device structures of the (a) single-unit, (b) double-unit OLEDs, and (c) double-unit OLEDs with an additional optical outcoupling layer.

## 7.6 Results and Discussion

A plot of the current density vs. voltage of a single-unit OLED and a double-unit OLED is shown in Figure 7.6. Figure 7.7 displays the luminance vs. voltage of a single-unit OLED, a double-unit OLED, and a double-unit OLED with an optical outcoupling layer. The turn-on voltages are 3.2 V for the single-unit OLED and 6.6 V for the double-unit OLED without the optical outcoupling layer. The fact that the turn-on voltage of the double-unit OLED is about twice that of the single-unit OLED suggests that the CU is very effective at generating electrons and holes. The current density vs. voltage and

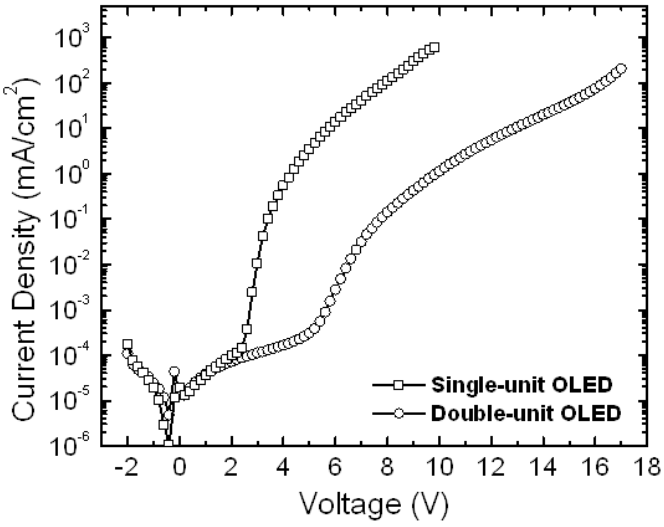


**Figure 7.6.** Current-density versus voltage of single-unit and double-unit OLEDs.

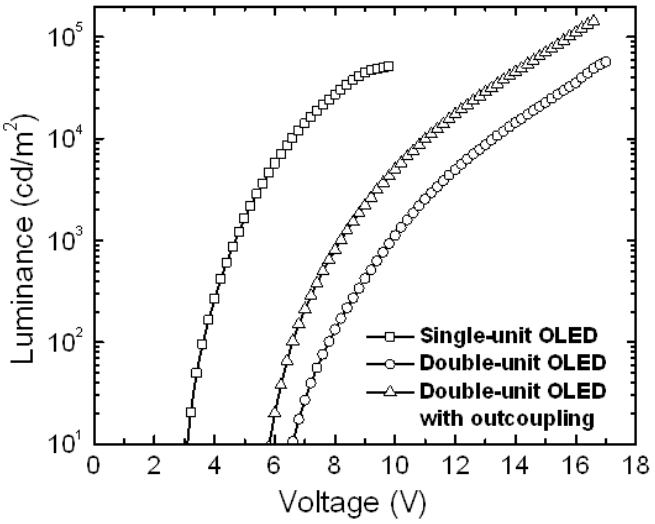


**Figure 7.7.** Luminance versus voltage of single and double-unit OLEDs, as well as a double-unit OLED with an optical outcoupling layer.

luminance vs. voltage characteristics demonstrate that the double-unit OLED electrically and optically operates like two single-unit OLEDs connected in series and stacked upon

each other. When an optical outcoupling layer is added to the double- unit OLED, a noticeable increase in luminance is achieved at all voltages.

Figure 7.8 shows the current efficacy vs. luminance plot for single-unit and double-unit OLEDs as well as double-unit OLEDs with an optical outcoupling layer. As expected, the double-unit OLEDs have about twice the current efficacy of the single-unit OLEDs. The single-unit OLED has a current efficacy of 46.8 cd/A at a luminance of 1215 cd/m$^2$, while the double-unit OLED exhibits a current efficacy of 97.8 cd/A at a luminance of 1,119 cd/m$^2$. Adding an optical outcoupling layer to the double-unit OLEDs leads to a further enhancement of a factor of about two. This remarkable enhancement is due to the microcavity effects of the Al cathode, Au anode, and optical outcoupling layer. It has been previously shown that a two-unit microcavity OLED can achieve up to a five-fold efficiency enhancement over a single-unit OLED if resonant conditions are met [143]. It is also known that adding a dielectric layer on top of a top-emitting OLED changes the optical structure of the device [38]. Adding an outcoupling layer to our two-unit top-emitting OLED has likely altered the complex interference effects within the OLED, leading to the observed outcoupling enhancement. These OLEDs have a current efficacy of 200 cd/A at a luminance of 1011 cd/m$^2$, attaining a maximum current efficacy of 205 cd/A at luminance of 103 cd/m$^2$. Table 5 contains the average performance and standard deviation of a total of seven double-unit OLEDs with optical outcoupling.

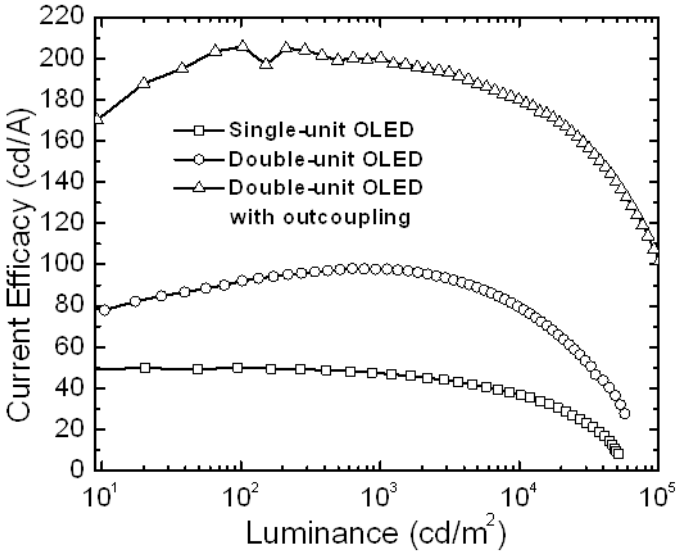


**Figure 7.8**. Current efficacy vs. luminance of single and double-unit OLEDs, and a double-unit OLED with an optical outcoupling layer.

**Table 5.** Average performance and standard deviation calculated from seven double-unit OLEDs with optical outcoupling.

| Luminance [cd/m$^2$] | Voltage [V] | Current Density [mA/cm$^2$] | Current Efficacy [cd/A] |
|---|---|---|---|
| 10 | 6.0 (± 0.1) | 0.01 (± 0.1) | 155.6 (± 27.5) |
| 100 | 6.8 (± 0.2) | 0.06 (± 0.01) | 189.9 (± 10.6) |
| 1,000 | 8.4 (± 0.1) | 0.50 (± 0.06) | 191.8 (± 5.6) |
| 1,0000 | 11.3 (± 0.1) | 5.3 (± 0.1) | 174.1 (± 3.0) |

The angular spectra of the double-unit OLEDs with an outcoupling layer are presented in

Figure 7.9. The measurements are normalized to the maximum intensity of the spectrum collected at 0°. The inset shows the change in the CIE coordinates (*x*,*y*) as a function of viewing-angle. Figure 7.10 compares the angular electroluminescent intensity of these OLEDs to what would be expected from a Lambertian emitter. The electroluminescent intensity values are normalized with respect to the intensity at the

peak wavelength of the 0° spectrum. The wavelength is kept fixed at each angle during normalization. It is clear that the angular viewing characteristics of these OLEDs differ significantly from a Lambertian emitter. Thus, measurements of EQE and power efficacy have not been reported.

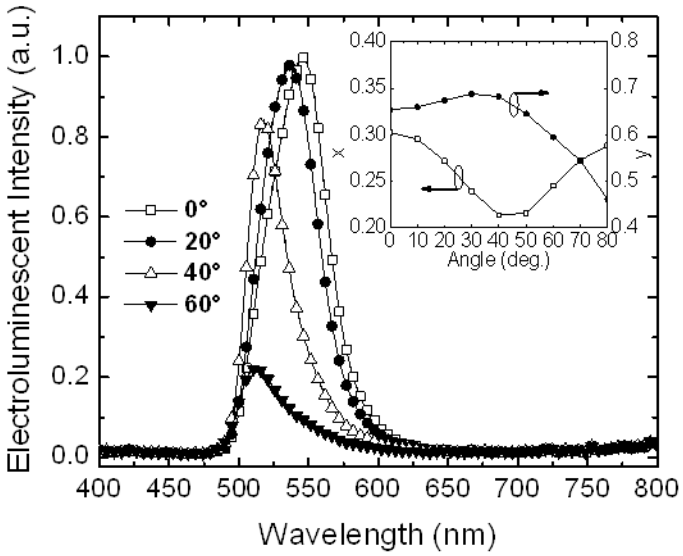


**Figure 7.9.** Electroluminescent intensity of double-unit OLEDs with an optical outcoupling layer with an inset showing the change in the CIE coordinates as a function of angle.

Figure 7.11a is a top-view photograph of a double-unit inverted top-emitting OLED on flexible glass (Corning). The flexible glass substrates have a thickness of about 100 μm (side-view shown in Figure 7.11b). When benchmark substrates of glass are loaded in the same batch as flexible glass substrates, the performance of OLEDs on both substrates is similar.

It should be noted that we have recently used this stacking methodology to produce stacked inverted top-emitting white electrophosphorescent OLEDs. They consist

of orange and blue light-emitting units connected by an HATCN/TAPC CU and have a current efficacy of 26.5 cd/A at a luminance of 100 cd/m$^2$ [152].

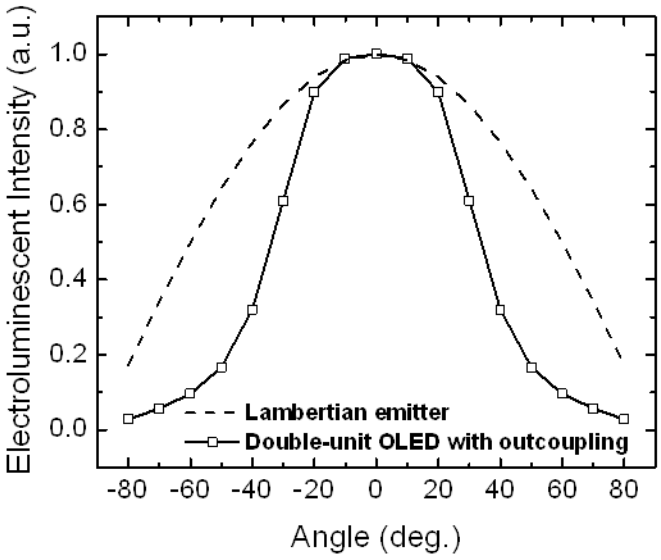


**Figure 7.10.** Normalized electroluminescent intensity versus angle compared with a Lambertian emitter.

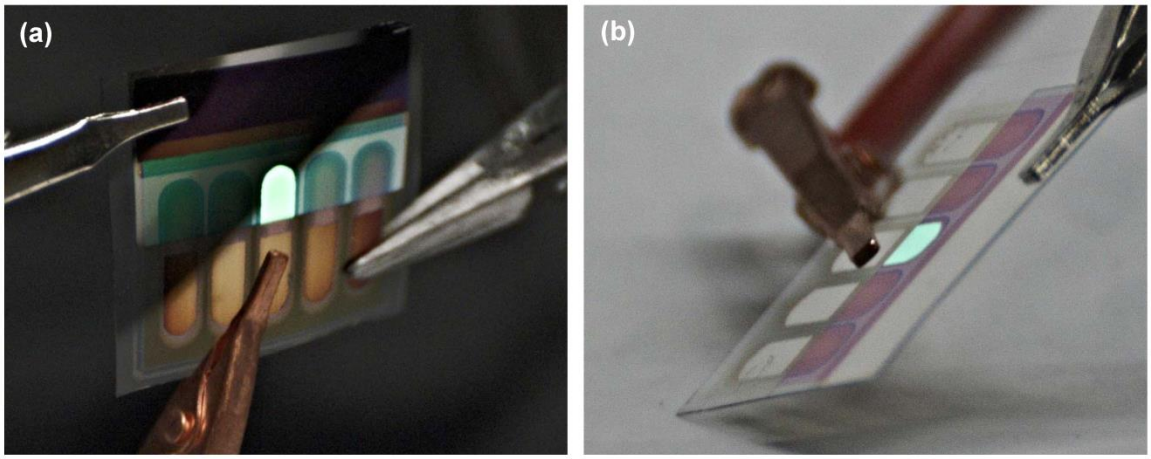


**Figure 7.11.** Picture of a double-unit stacked inverted top-emitting OLED with an optical outcoupling layer on flexible glass. The views of the substrate are from the (a) top and from the (b) side.

# CHAPTER 8

# Conclusions and Outlook

## 8.1 Conclusions

In conclusion this work reports on the design, fabrication, and testing of state-of-the-art, high-performance OLEDs. The particular device architecture emphasized is one in which the devices are inverted (i.e. their cathode is on the bottom) and top-emitting. Despite the advantages that inverted top-emitting OLEDs possess over conventional bottom-emitting OLEDs, the development of this type of device has been hampered by the difficulty of injecting electrons effectively into the device.

Chapter 4 detailed the discovery of a novel method of injecting electrons from bottom cathodes into electron-transport materials. In several previous reports, bottom Al/LiF cathodes had been used with $Alq_3$ to produce inverted OLEDs, but the resulting inverted OLEDs exhibited inferior performance to conventional OLEDs with top cathodes of Al/LiF. Electron-dominated devices were presented that show that if a high-mobility ETL is used, bottom Al/LiF cathodes are nearly as effective at injecting electrons as top Al/LiF cathodes.

This discovery opened a new route for producing highly efficient inverted top-emitting OLEDs for potential use in displays. In chapter 5, a general inverted top-emitting device architecture was presented. Various green inverted top-emitting OLEDs were demonstrated with ETLs with the same EA but different electron mobility values. It was shown that for the architecture chosen, as the mobility of the ETL increases, the performance of the OLEDs also increases showing improved carrier balance. Once

optimized through the choice of material, the thickness of the layers, and the addition of an optical outcoupling layer, these green devices achieved unprecedented current efficacy for inverted OLEDs.

In chapter 6, blue inverted top-emitting OLEDs were developed. Blue emission presents its own design challenges, and these challenges were overcome through material choices. To ensure efficient energy transfer and exciton to the phosphorescent blue dopant FIrpic, the lower triplet energy CBP host was replaced with the higher triplet energy host of mCP. In addition, it was shown that using TmPyPB as the ETL material increased device efficiency over devices with TpPyPB most likely through a combination of improved charge carrier balance and enhanced exciton confinement to the host.

Finally, chapter 7 used the knowledge gained from the previous chapters to develop stacked inverted top-emitting OLED for the first time. These devices combine all of the advantages offered by an inverted architecture, a top-emissive design, and a stacked structure. The inverted OLED architecture previously presented was shown to be amenable to stacking through the use of a CU consisting of HAT-CN/TAPC. This interface leads to efficient free-carrier generation, as the two-unit devices were shown to electrically behave as two OLEDs electrically connected in series and vertically stacked upon each other. When an optical outcoupling layer was added, the performance of these OLEDs surpassed all previous two-unit stacked OLEDs in terms of current efficacy.

## 8.2 Recommendations for Future Work

There are several opportunities to further develop the work presented in this thesis in order to better understand inverted top-emitting OLEDs and improve their performance. These opportunities include analyzing the interfaces that have been shown

to be critical to their performance, taking measurements of their EQE and power efficacy, and assessing their operational lifetime.

### 8.2.1 Interface Analysis

The high performance of the devices presented results from judicious material choices such as the combination of Al/LiF/ETL when used as at the bottom of inverted OLEDs and HAT-CN/TAPC when used in the CU of stacked OLEDs. Much can be learned through the use of material science techniques to study the properties of the interfaces between these materials. In particular, UPS can reveal detailed information about the energetic structure of material interfaces such as the values of the Fermi level, ionization energy, and vacuum level. In addition, X-ray photoelectron spectroscopy (XPS) would provide insight into any chemical interactions that might be occurring between the materials. Ideally, a system capable of both sample growth and analysis under ultra-high vacuum should be used [45]. With this data, a greater understanding would be gained of how charges are being injected, generated, and transported in these inverted OLEDs.

### 8.2.2 EQE and Power Efficacy Measurements

The inverted top-emitting OLEDs presented in this work contain a microcavity, and microcavity devices cannot be assumed to be Lambertian emitters [79, 128]. Unlike Lambertian emitters, their EQE and power efficacy values cannot be calculated from a single optical measurement of the light output over a small solid angle in the direction of the OLED's surface normal. Obtaining the EQE and power efficacy values would allow for very useful comparisons to other reported devices, especially Lambertian bottom-emitting devices.

The EQE and power efficacy values of non-Lambertian OLEDs can be directly measured by methods using instrumentation that captures all of the light emitted from the surface of the devices. One possible approach is to use an integrating sphere with a calibrated photodiode. An integrating sphere consists of a hollow chamber with an interior that is coated by a diffusively reflective material. Light emitted within the integrating sphere is diffusely reflected and isotropically redistributed over its interior surface [153]. Another method of determining the EQE and power efficacy of non-Lambertian OLEDs is to measure them in a setup that ensures every photon emitted is detected by a large-area photodetector that has been placed very close to the OLED [76].

### 8.2.3 Operational Lifetime

A final fruitful area of future work would be focused on answering the following questions: *How long do these inverted top-emitting OLEDs operate? What are the dominant mechanisms leading to their degradation? How can the operational lifetime of these OLEDs be extended?* Answering these questions is critical because both high efficiency and long operation lifetime are required for OLEDs to be use in most OLED-based application [32].

Few studies of inverted OLEDs have been undertaken by others [154, 155]. The longest-lived inverted devices had a structure of ITO/Mg/$Cs_2O$:BPhen/C545T:$Alq_3$/NPB/$WO_3$/Al and possessed an operational lifetime of 104,000 h at 100 cd/$m^2$ [155]. These fluorescent OLEDs had a current efficacy of about 24 cd/A at 100 cd/$m^2$. This demonstrates that inverted OLEDs with long device lifetimes can be made. However, the efficiency is significantly lower than the efficiencies attainable with devices containing phosphorescent dopants. For instance, our inverted

top-emitting electrophosphorescent OLEDs have a current efficacy as high as 124.7 cd/A at 100 cd/m$^2$ [156]. Though we have achieved high efficiencies with our inverted top-emitting OLEDs, the operational lifetimes of our devices are unknown. Future reports will have a greater impact if the OLEDs are optimized for both high efficiency and long operational lifetime. Some degradation mechanisms might be isolated and better understood by fabricating hole- and electron-dominated devices composed of the constituent materials within the OLEDs. By measuring these simpler devices under constant current and voltage conditions over time, the stability of single organic layers and organic-electrode heterojunctions can be studied.

### 8.3 List of Publications

Knauer, K. A., Najafabadi E., Haske W., and Kippelen B. (2012). Inverted top-emitting blue electrophosphorescent organic light-emitting diodes with high current efficacy. *Applied Physics Letters,* 101(10), 103304.

Najafabadi E., Knauer K.A., Haske W., Fuentes-Hernandez C., and Kippelen B. (2012). Highly efficient inverted top-emitting green phosphorescent organic light-emitting diodes on glass and flexible substrates. *Applied Physics Letters,* 101(2), 023304.

Najafabadi E., Knauer K. A., Haske W., and Kippelen B. (2013). High-performance inverted top-emitting green electrophosphorescent organic light-emitting diodes with a modified top Ag anode. *Organic Electronics,* 14(5), 1271-1275.

Knauer K. A., Najafabadi E., Haske W., Gaj M. P., Davis K. C., Fuentes-Hernandez C., Carrasco U., and Kippelen B. (2013). Stacked inverted top-emitting green electrophosphorescent organic light-emitting diodes on glass and flexible glass substrates. *Organic Electronics,* 14(10), 2418-2423.

Najafabadi E., Knauer K. A., Haske W., Fuentes-Hernandez C., and Kippelen B. (2013) Stacked inverted top-emitting white organic light-emitting diodes composed of orange and blue light-emitting units. *Applied Physics Letters*, 103(19), 193303.

# APPENDIX A

## A.1 Thermally Activated Delayed Fluorescence

In the process of TADF (see Figure A.1), triplets are converted into singlets by harvesting thermal energy from the environment. Converting triplets to singlets relies on reverse ISC, so spin-orbit coupling is required. The first-order mixing coefficient between triplet and singlet states, $\lambda$, is given by,

$$\lambda \propto \frac{\boldsymbol{H_{SO}}}{\Delta E_{ST}} \qquad (8.1)$$

where $H_{SO}$ is the spin-orbit interaction and $\Delta E_{ST}$ is the energy difference between the first excited singlet and triplet states. The value of $\lambda$ is inversely proportional to $\Delta E_{ST}$, so if $\Delta E_{ST}$ is sufficiently small (<100 meV), adequate mixing between triplet and singlet states occurs. For most organic molecules, $\Delta E_{ST}$ is typically about 0.5 eV – 1.0 eV, but by careful molecular design, both of a sufficiently small $\Delta E_{ST}$ and relatively high radiative decay constant can be simultaneously achieved [72].

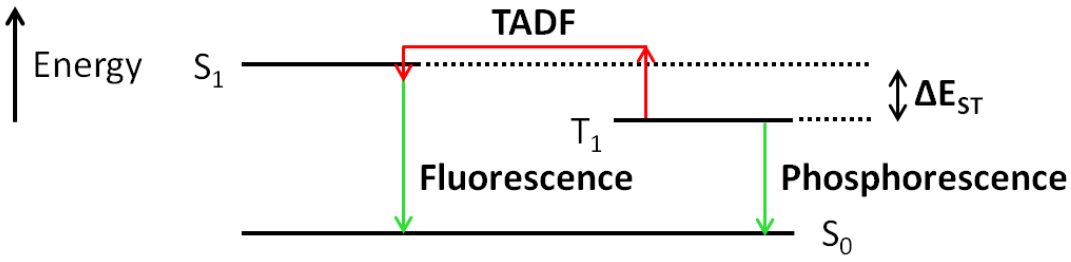


**Figure A.1.** Graphical illustration of TADF in which triplet excitons are thermally excited with enough energy to convert to singlet excitons through reverse intersystem crossing.

In OLEDs containing TADF emitters, a host-guest system is used in to prevent nonradiative decay due concentration quenching, and the host must possess a higher triplet level energy than the guest for triplet confinement on the guest [74]. One class of

efficient TADF emitters has been designed based on carbazolyl dicyanobenzene, and have yielded OLEDs a maximum EQE as high as 19.3% [72]. In addition, OLEDs with TADF have been shown to have an operational lifetime of over 2500 h at an initial luminance of 1,000 cd/$m^2$.

### A.2 Organic Vapor Phase Deposition

OVPD differs from VTE in that the evaporation sources are decoupled from the evaporation process. Organic material is heated in separate, valve-actuated source cells and thermally evaporated into a stream of inert carrier gas. The carrier gas flows through a heated chamber, transporting the organic material to a cooled substrate where it is deposited by physisorption. A showerhead is used to introduce the organic material to the substrate in order to provide homogenous deposition, high material utilization, and simplified scaling rules. The deposition rate is precisely controlled by changing the flow of the carrier gas, and the thickness of the material deposited is read by a quartz crystal microbalance. Of significant interest is the fact that this method of rate control allows for the codeposition of materials to form layers with continuous concentration gradings. OLEDs with these layers show improved charge balance, resulting in enhanced performance and thus possibility improved operational lifetimes [89, 157]. The walls of the chamber are kept at a high enough temperature to prevent material from being deposited on them, which reduces material waste, improves system cleanliness, and reduced system downtime for cleaning [89]. These advantages, along with the fact that the process is scalable to very large substrates, may make OVPD a key technology for advancing the organic electronics industry [158].

# References


[1] Tang, C. W., & Van Slyke, S. A. (1987). Organic electroluminescent diodes. *Applied Physics Letters, 51,* 913-915.

[2] http://www.samsung.com/us. Retrieved January 17, 2014.

[3] www.lg.com/us. Retrieved January 17, 2014.

[4] http://displays.mitsubishielectric.eu/. Retrieved January 17, 2014.

[5] Perry, T. S. (2013). Oled TV arrives. *Spectrum, IEEE, 50*, 46-47.

[6] Boer, W. d. (2005). *Active Matrix Liquid Crystal Displays* (1st ed.). Burlington, MA: Newnes.

[7] Heilmeier, G. H., Zanoni, L. A., & Barton, L. A. (1968). Dynamic scattering - A new electrooptic effect in certain classes of nematic liquid crystals. *Proceedings of the Institute of Electrical and Electronics Engineers, 56*, 1162-1171.

[8] Schadt, M., & Helfrich, W. (1971). Voltage-dependent optical activity of a twisted nematic liquid crystal. *Applied Physics Letters, 18,* 127-128.

[9] Lechner, B. J., Marlowe, F. J., Nester, E. O., & Tults, J. (1971). Liquid crystal matrix displays. *Proceedings of the Institute of Electrical and Electronics Engineers, 59*, 1566-1579.

[10] Tsujimura, T. (2013). *OLED Displays: Fundamentals and Applications* (1st Ed. ed.). Hoboken, N.J.: Wiley.

[11] Forrest, S. R. (2003). The road to high efficiency organic light emitting devices. *Organic Electronics, 4,* 45-48.

[12] Humphreys, C. J. (2008). Solid-state lighting. *Mrs Bulletin, 33,* 459-470.

[13] *Solid-State Lighting Research and Development: Multi-Year Program Plan*. (2013). U.S. Department of Energy.

[14] http://www.lighting.philips.com/. Retrieved January 19, 2014.

[15] http://www.lgchem.com/. Retrieved January 19, 2014.

[16] http://www.panasonic.net/. Retrieved January 19, 2014.

[17] Holonyak, N., & Bevacqua, S. F. (1962). Coherent (visible) light emission from $Ga(As_{1-x}P_x)$ junctions. *Applied Physics Letters, 1*, 82-83.

[18] Park, J. W., Shin, D. C., & Park, S. H. (2011). Large-area OLED lightings and their applications. *Semiconductor Science and Technology*, *26*, 034002.

[19] Gather, M. C., Köhnen, A., & Meerholz, K. (2011). White organic light-emitting diodes. *Advanced Materials*, *23*, 233-248.

[20] http://www.displaysearch.com/. Retrieved January 21, 2014.

[21] Pope, M., Magnante, P., & Kallmann, H. P. (1963). Electroluminescence in organic crystals. *Journal of Chemical Physics*, *38*, 2042-2043.

[22] Partridge, R. H. (1983). Electro-luminescence from polyvinylcarbazole films: 3. Electrolluminescent devices. *Polymer*, *24*, 748-754.

[23] Burroughes, J. H., Bradley, D. D. C., Brown, A. R., Marks, R. N., Mackay, K., Friend, R. H., Burns, P. L., & Holmes, A. B. (1990). Light-emitting diodes based on conjugated polymers. *Nature*, *347*, 539-541.

[24] Forrest, S. R. (2004). The path to ubiquitous and low-cost organic electronic appliances on plastic. *Nature*, *428*, 911-918.

[25] Tang, C. W., Van Slyke, S. A., & Chen, C. H. (1989). Electroluminescence of doped organic thin-films. *Journal of Applied Physics*, *65*, 3610-3616.

[26] Baldo, M. A., O'Brien, D. F., You, Y., Shoustikov, A., Sibley, S., Thompson, M. E., & Forrest, S. R. (1998). Highly efficient phosphorescent emission from organic electroluminescent devices. *Nature*, *395*, 151-154.

[27] Wang, Z. B., Helander, M. G., Qiu, J., Puzzo, D. P., Greiner, M. T., Hudson, Z. M., Wang, S., Liu, Z. W., & Lu, Z. H. (2011). Unlocking the full potential of organic light-emitting diodes on flexible plastic. *Nature Photonics*, *5*, 753-757.

[28] Chen, S. F., Deng, L. L., Xie, J., Peng, L., Xie, L. H., Fan, Q. L., & Huang, W. (2010). Recent developments in top-emitting organic light-emitting diodes. *Advanced Materials*, *22*, 5227-5239.

[29] Hamada, Y., Adachi, C., Tsutsui, T., & Saito, S. (1992). Blue light-emitting organic electroluminescent devices with oxadiazole dimer dyes as an emitter. *Japanese Journal of Applied Physics Part 1-Regular Papers Short Notes & Review Papers*, *31*, 1812-1816.

[30] Park, J.-S., Chae, H., Chung, H. K., & Lee, S. I. (2011). Thin film encapsulation for flexible AM-OLED: a review. *Semiconductor Science and Technology*, *26*, 034001.

[31] Burrows, P. E., Bulovic, V., Forrest, S. R., Sapochak, L. S., McCarty, D. M., & Thompson, M. E. (1994). Reliability and Degradation of Organic Light-Emitting Devices. *Applied Physics Letters, 65,* 2922-2924.

[32] Van Slyke, S. A., Chen, C. H., & Tang, C. W. (1996). Organic electroluminescent devices with improved stability. *Applied Physics Letters, 69,* 2160-2162.

[33] Aziz, H., & Popovic, Z. D. (2002). Study of organic light emitting devices with a 5,6,11,12-tetraphenylnaphthacene (rubrene)-doped hole transport layer. *Applied Physics Letters, 80,* 2180-2182.

[34] Orselli, E., Maunoury, J., Bascour, D., & Catinat, J. P. (2012). Orange phosphorescent organic light-emitting diodes with high operational stability. *Organic Electronics, 13,* 1506-1510.

[35] Meerheim, R., Walzer, K., Pfeiffer, M., & Leo, K. (2006). Ultrastable and efficient red organic light emitting diodes with doped transport layers. *Applied Physics Letters, 89,* 061111.

[36] Cusumano, P., Buttitta, F., Di Cristofalo, A., & Cali, C. (2003). Effect of driving method on the degradation of organic light emitting diodes. *Synthetic Metals, 139,* 657-661.

[37] Wellmann, P., Hofmann, M., Zeika, O., Werner, A., Birnstock, J., Meerheim, R., He, G. F., Walzer, K., Pfeiffer, M., & Leo, K. (2005). High-efficiency p-i-n organic light-emitting diodes with long lifetime. *Journal of the Society for Information Display, 13,* 393-397.

[38] Wu, C. C., Chen, C. W., Lin, C. L., & Yang, C. J. (2005). Advanced organic light-emitting devices for enhancing display performances. *Journal of Display Technology, 1,* 248-266.

[39] http://www.udcoled.com/. Retrieved January 19, 2014

[40] Griffiths, D. J. (1995). *Introduction to Quantum Mechanics* (2nd ed.). Upper Saddle River, NJ: Prentice Hall.

[41] Carey, F. A. (2004). *Organic Chemistry* (5th ed.). New York, NY: McGraw-Hill.

[42] Bredas, J.-L. (2014). Mind the gap! *Materials Horizons, 1,* 17-19.

[43] Scott, J. C. (2003). Metal-organic interface and charge injection in organic electronic devices. *Journal of Vacuum Science & Technology A, 21,* 521-531.

[44] Ishii, H., Sugiyama, K., Ito, E., & Seki, K. (1999). Energy level alignment and interfacial electronic structures at organic metal and organic organic interfaces. *Advanced Materials, 11,* 605-625.

[45] Hill, I. G., Milliron, D., Schwartz, J., & Kahn, A. (2000). Organic semiconductor interfaces: Electronic structure and transport properties. *Applied Surface Science, 166,* 354-362.

[46] Hwang, J., Wan, A., & Kahn, A. (2009). Energetics of metal-organic interfaces: New experiments and assessment of the field. *Materials Science & Engineering R-Reports, 64,* 1-31.

[47] Hung, L. S., & Chen, C. H. (2002). Recent progress of molecular organic electroluminescent materials and devices. *Materials Science & Engineering R-Reports, 39,* 143-222.

[48] Haldi, A., Sharma, A., Potscavage, W. J., & Kippelen, B. (2008). Equivalent circuit model for organic single-layer diodes. *Journal of Applied Physics, 104,* 064503.

[49] Fowler, R. H., & Nordheim, L. (1928). Electron emission in intense electric fields. *Proceedings of the Royal Society of London Series a-Containing Papers of a Mathematical and Physical Character, 119,* 173-181.

[50] Malliaras, G. G., & Scott, J. C. (1998). The roles of injection and mobility in organic light emitting diodes. *Journal of Applied Physics, 83,* 5399-5403.

[51] Coropceanu, V., Cornil, J., da Silva, D. A., Olivier, Y., Silbey, R., & Brédas, J. L. (2007). Charge transport in organic semiconductors. *Chemical Reviews, 107,* 926-952.

[52] Marcus, R. A. (1993). Electron-transfer reactions in chemistry - theory and experiment. *Reviews of Modern Physics, 65,* 599-610.

[53] Lampert, M. (1970). *Current Injection in Solids*. New York, NY: Academic Press.

[54] Jurchescu, O. D., Popinciuc, M., van Wees, B. J., & Palstra, T. T. M. (2007). Interface-controlled, high-mobility organic transistors. *Advanced Materials, 19,* 688-692.

[55] Sundar, V. C., Zaumseil, J., Podzorov, V., Menard, E., Willett, R. L., Someya, T., Gershenson, M. E., & Rogers, J. A. (2004). Elastomeric transistor stamps: Reversible probing of charge transport in organic crystals. *Science, 303,* 1644-1646.

[56] Itaka, K., Yamashiro, M., Yamaguchi, J., Haemori, M., Yaginuma, S., Matsumoto, Y., Kondo, M., & Koinuma, H. (2006). High-mobility C-60 field-effect molecular-wetting controlled transistors fabricated on substrates. *Advanced Materials*, *18*, 1713-1716.

[57] Bässler, H. (1993). Charge transport in disordered organic photoconductors - a monte-carlo simulation study. *Physica Status Solidi B-Basic Research*, *175*, 15-56.

[58] Miller, A., & Abrahams, E. (1960). Impurity conduction at low concentrations. *Physical Review*, *120*, 745-755.

[59] Borsenberger, P. M., Pautmeier, L., & Bässler, H. (1991). Charge transport in disordered molecular solids. *Journal of Chemical Physics*, *94*, 5447-5454.

[60] Borsenberger, P. M., Gruenbaum, W. T., & Magin, E. H. (1996). Hole transport in vapor deposited bis(ditolylaminostyryl)benzene. *Physica B*, *228*, 226-232.

[61] Patel, N. K., Cinà, S., & Burroughes, J. H. (2002). High-efficiency organic light-emitting diodes. *Ieee Journal of Selected Topics in Quantum Electronics*, *8*, 346-361.

[62] Murgatroyd, P. N. (1970). Theory of space-charge-limited current enhanced by Frenkel effect. *Journal of Physics D-Applied Physics*, *3*, 151-&.

[63] Pope, M., & Swenberg, C. E. (1999). *Electronic Processes in Organic Crystals and Polymers* (2nd ed.). New York: Oxford University Press.

[64] Langevin, P. (1903). The ionisation of gases. *Annales De Chimie Et De Physique*, *28*, 289-384.

[65] Baldo, M. A., Lamansky, S., Burrows, P. E., Thompson, M. E., & Forrest, S. R. (1999). Very high-efficiency green organic light-emitting devices based on electrophosphorescence. *Applied Physics Letters*, *75*, 4-6.

[66] Förster, T. (1959). 10th spiers memorial lecture - transfer mechanisms of electronic excitation. *Discussions of the Faraday Society*, 7-17.

[67] Dexter, D. L. (1953). A theory of sensitized luminescence in solids. *Journal of Chemical Physics*, *21*, 836-850.

[68] Adachi, C., Baldo, M. A., Thompson, M. E., & Forrest, S. R. (2001). Nearly 100% internal phosphorescence efficiency in an organic light-emitting device. *Journal of Applied Physics*, *90*, 5048-5051.

[69] Beljonne, D., Shuai, Z., Cornil, J., Calbert, J. P., & Bredas, J. L. (2001). On the luminescence efficiency of polymer light-emitting diodes: a quantum-chemical investigation. *Journal of Photochemistry and Photobiology a-Chemistry, 144*, 57-62.

[70] Thompson, M. E., Burrows, P. E., & Forrest, S. R. (1999). Electrophosphorescence in organic light emitting diodes. *Current Opinion in Solid State & Materials Science, 4*, 369-372.

[71] Nakanotani, H., Masui, K., Nishide, J., Shibata, T., & Adachi, C. (2013). Promising operational stability of high-efficiency organic light-emitting diodes based on thermally activated delayed fluorescence. *Scientific Reports, 3*, 2127.

[72] Uoyama, H., Goushi, K., Shizu, K., Nomura, H., & Adachi, C. (2012). Highly efficient organic light-emitting diodes from delayed fluorescence. *Nature*, *492*, 234-240.

[73] Endo, A., Ogasawara, M., Takahashi, A., Yokoyama, D., Kato, Y., & Adachi, C. (2009). Thermally activated delayed fluorescence from $Sn4^{+}$-porphyrin complexes and their application to organic light-emitting diodes - a novel mechanism for electroluminescence. *Advanced Materials, 21*, 4802-4806.

[74] Endo, A., Sato, K., Yoshimura, K., Kai, T., Kawada, A., Miyazaki, H., & Adachi, C. (2011). Efficient up-conversion of triplet excitons into a singlet state and its application for organic light emitting diodes. *Applied Physics Letters, 98*, 083302.

[75] Adachi, C., Baldo, M. A., Forrest, S. R., & Thompson, M. E. (2000). High-efficiency organic electrophosphorescent devices with tris(2-phenylpyridine)iridium doped into electron-transporting materials. *Applied Physics Letters, 77*, 904-906.

[76] Forrest, S. R., Bradley, D. D. C., & Thompson, M. E. (2003). Measuring the efficiency of organic light-emitting devices. *Advanced Materials, 15*, 1043-1048.

[77] Kim, J. S., Ho, P. K. H., Greenham, N. C., & Friend, R. H. (2000). Electroluminescence emission pattern of organic light-emitting diodes: Implications for device efficiency calculations. *Journal of Applied Physics, 88*, 1073-1081.

[78] Saxena, K., Jain, V. K., & Mehta, D. S. (2009). A review on the light extraction techniques in organic electroluminescent devices. *Optical Materials, 32*, 221-233.

[79] Hofmann, S., Thomschke, M., Lüssem, B., & Leo, K. (2011). Top-emitting organic light-emitting diodes. *Optics Express, 19*, A1250-A1264.

[80] Kröger, M., Dobbertin, T., Schneider, D., Rabe, T., Becker, E., Johannes, H. H., & Kowalsky, W. (2004). Highly efficient guest-host-systems for hybrid inverted organic light-emitting diodes with sputtered indium-tin-oxide anodes. *Organic Light-Emitting Materials and Devices VIII, 5519*, 143-152.

[81] Hou, J. H., Wu, J., Xie, Z. Y., & Wang, L. X. (2009). Efficient inverted top-emitting organic light-emitting diodes using ultrathin $MoO_3/C_{60}$ bilayer structure to enhance hole injection. *Applied Physics Letters*, *95*, 203508.

[82] Huang, Q., Walzer, K., Pfeiffer, M., Leo, K., Hofmann, M., & Stubinger, T. (2006). Performance improvement of top-emitting organic light-emitting diodes by an organic capping layer: An experimental study. *Journal of Applied Physics*, *100*, 064507.

[83] Riel, H., Karg, S., Beierlein, T., Ruhstaller, B., & Rieß, W. (2003). Phosphorescent top-emitting organic light-emitting devices with improved light outcoupling. *Applied Physics Letters*, *82*, 466-468.

[84] Möller, S., & Forrest, S. R. (2002). Improved light out-coupling in organic light emitting diodes employing ordered microlens arrays. *Journal of Applied Physics*, *91*, 3324-3327.

[85] Sun, Y., & Forrest, S. R. (2008). Enhanced light out-coupling of organic light-emitting devices using embedded low-index grids. *Nature Photonics*, *2*, 483-487.

[86] McCluney, W. R. (1994). *Introduction to Radiometry and Photometry*. Boston, MA: Artech House, Inc.

[87] Greenham, N. C., Friend, R. H., & Bradley, D. D. C. (1994). Angular-dependence of the emission from a conjugated polymer light-emitting diode - Implications for efficiency calculations. *Advanced Materials*, *6*, 491-494.

[88] Forrest, S. R. (1997). Ultrathin organic films grown by organic molecular beam deposition and related techniques. *Chemical Reviews*, *97*, 1793-1896.

[89] Kreis, J., Schwambera, M., Keiper, D., Gersdorff, M., Long, M., & Heuken, M. (2012). Organic vapor phase deposition (OVPD ®) for efficient OLED manufacturing: The specific advantages and possibilities of carrier-gas enhanced vapor phase deposition for the manufacturing of organic thin film devices. *Organic Light Emitting Materials and Devices XVI, 8476*, 84761.

[90] Burrows, P. E., Forrest, S. R., Sapochak, L. S., Schwartz, J., Fenter, P., Buma, T., Ban, V. S., & Forrest, J. L. (1995). Organic vapor-phase deposition - A new method for the growth of organic thin-films with large optical nonlinearities. *Journal of Crystal Growth*, *156*, 91-98.

[91] Baldo, M. A., Kozlov, V. G., Burrows, P. E., Forrest, S. R., Ban, V. S., Koene, B., & Thompson, M. E. (1997). Low pressure organic vapor phase deposition of small molecular weight organic light emitting device structures. *Applied Physics Letters*, *71*, 3033-3035.

[92] Steyrleuthner, R., Bange, S., & Neher, D. (2009). Reliable electron-only devices and electron transport in n-type polymers. *Journal of Applied Physics*, *105*, 064509.

[93] Matsushima, T., Goushi, K., & Adachi, C. (2007). Charge-carrier injection characteristics at organic/organic heterojunction interfaces in organic light-emitting diodes. *Chemical Physics Letters*, *435*, 327-330.

[94] Michaelson, H. B. (1977). Work function of elements and its periodicity. *Journal of Applied Physics*, *48*, 4729-4733.

[95] Mason, M. (2001). Interfacial chemistry of $Alq_3$ and LiF with reactive metals. *Journal of Applied Physics*, *89*, 2756-2765.

[96] Walzer, K., Maennig, B., Pfeiffer, M., & Leo, K. (2007). Highly efficient organic devices based on electrically doped transport layers. *Chemical Reviews*, *107*, 1233-1271.

[97] Hung, L. S., Tang, C. W., & Mason, M. G. (1997). Enhanced electron injection in organic electroluminescence devices using an Al/LiF electrode. *Applied Physics Letters*, *70*, 152-154.

[98] Piromreun, P., Oh, H., Shen, Y. L., Malliaras, G. G., Scott, J. C., & Brock, P. J. (2000). Role of CsF on electron injection into a conjugated polymer. *Applied Physics Letters*, *77*, 2403-2405.

[99] Heil, H., Steiger, J., Karg, S., Gastel, M., Ortner, H., von Seggern, H., & Stößel, M. (2001). Mechanisms of injection enhancement in organic light-emitting diodes through an Al/LiF electrode. *Journal of Applied Physics*, *89*, 420-424.

[100] Choudhury, K. R., Yoon, J. H., & So, F. (2008). LiF as an n-dopant in tris(8-hydroxyquinoline) aluminum thin films. *Advanced Materials*, *20*, 1456-1461.

[101] Kim, K. H., Huh, S. Y., Seo, S. M., & Lee, H. H. (2008). Inverted top-emitting organic light-emitting diodes by whole device transfer. *Organic Electronics*, *9*, 1118-1121.

[102] Wang, Q., Wang, F. X., Qiao, X. F., & Ma, D. G. (2009). Lead(IV) dioxide: An effective electron injection material to realize high-efficiency inverted top-emitting organic light-emitting diodes. *Semiconductor Science and Technology*, *24*, 105027.

[103] Davids, P. S., Campbell, I. H., & Smith, D. L. (1997). Device model for single carrier organic diodes. *Journal of Applied Physics, 82*, 6319-6325.

[104] Su, S. J., Chiba, T., Takeda, T., & Kido, J. (2008). Pyridine-containing triphenylbenzene derivatives with high electron mobility for highly efficient phosphorescent OLEDs. *Advanced Materials*, *20*, 2125-2130.

[105] Najafabadi, E., Knauer, K. A., Haske, W., Fuentes-Hernandez, C., & Kippelen, B. (2012). Highly efficient inverted top-emitting green phosphorescent organic light-emitting diodes on glass and flexible substrates. *Applied Physics Letters, 101*, 023304.

[106] Bulović, V., Tian, P., Burrows, P. E., Gokhale, M. R., Forrest, S. R., & Thompson, M. E. (1997). A surface-emitting vacuum-deposited organic light emitting device. *Applied Physics Letters*, *70*, 2954-2956.

[107] Dobbertin, T., Werner, O., Meyer, J., Kammoun, A., Schneider, D., Riedl, T., Becker, E., Johannes, H. H., & Kowalsky, W. (2003). Inverted hybrid organic light-emitting device with polyethylene dioxythiophene-polystyrene sulfonate as an anode buffer layer. *Applied Physics Letters*, *83*, 5071-5073.

[108] Dobbertin, T., Kroeger, M., Heithecker, D., Schneider, D., Metzdorf, D., Neuner, H., Becker, E., Johannes, H. H., & Kowalsky, W. (2003). Inverted top-emitting organic light-emitting diodes using sputter-deposited anodes. *Applied Physics Letters*, *82*, 284-286.

[109] Chen, S. M., Yuan, Y. B., Lian, J. R., Xie, Z. F., & Zhou, X. (2008). Enhanced electron injection in inverted top-emitting OLEDs with *n*-Si cathode by using-$CS_2CO_3$ buffer layer. *Light-Emitting Diode Materials and Devices II*, *6828*, 68280O.

[110] Meng, Y. L., Xie, W. F., Zhang, N., Chen, S. F., Li, J., Hu, W., Zhao, Y., Hou, J. Y., & Liu, S. Y. (2008). Effective hole-injection layer for non-doped inverted top-emitting organic light-emitting devices. *Microelectronics Journal*, *39*, 723-726.

[111] Wang, Q., Deng, Z. Q., & Ma, D. G. (2009). Highly efficient inverted top-emitting organic light-emitting diodes using a lead monoxide electron injection layer. *Optics Express*, *17*, 17269-17278.

[112] Wang, Q., Deng, Z., Chen, J., & Ma, D. (2010). Manipulating the microcavity structure for highly efficient inverted top-emitting organic light-emitting diodes: Simulation and experiment. *IEEE Transactions on Electron Devices*, *57*, 2221-2226.

[113] Ryu, S. Y., Lee, C. H., Oh, I. S., Song, S. Y., Hwang, K. H., Hwang, H. S., Han, M. H., Hwang, B. H., Baik, H. K., Kim, Y. S., & Lee, J. Y. (2010). Efficient inverted top-emitting organic light emitting diodes with transparent and surface-modified multilayer anodes. *Electrochemical and Solid State Letters*, *13*, J43-J46.

[114] Zhang, X.-W., Lin, H.-P., Li, J., Zhang, L., Wei, B., Jiang, X.-Y., & Zhang, Z.-L. (2012). A very simple method of constructing efficient inverted top-emitting organic light-emitting diode based on Ag/Al bilayer reflective cathode. *Journal of Luminescence*, *132*, 1-5.

[115] Thomschke, M., Hofmann, S., Olthof, S., Anderson, M., Kleemann, H., Schober, M., Lüssem, B., & Leo, K. (2011). Improvement of voltage and charge balance in inverted top-emitting organic electroluminescent diodes comprising doped transport layers by thermal annealing. *Applied Physics Letters*, *98*, 083304.

[116] Thomschke, M., Furno, M., Lüssem, B., & Leo, K. (2010). Highly efficient inverted top-emitting organic electroluminescent devices with doped charge transport layers. *Organic Photonics IV*, *7722*, 77220.

[117] Yun, C., Cho, H., Koh, T. W., Kim, J. H., Kim, J. W., Park, Y., & Yoo, S. (2012). Doping-free inverted top-emitting organic light-emitting diodes with high power efficiency and near-ideal emission characteristics. *IEEE Transactions on Electron Devices*, *59*, 159-166.

[118] Milliron, D. J., Hill, I. G., Shen, C., Kahn, A., & Schwartz, J. (2000). Surface oxidation activates indium tin oxide for hole injection. *Journal of Applied Physics*, *87*, 572-576.

[119] Elschner, A., Bruder, F., Heuer, H. W., Jonas, F., Karbach, A., Kirchmeyer, S., & Thurm, S. (2000). PEDT/PSS for efficient hole-injection in hybrid organic light-emitting diodes. *Synthetic Metals*, *111*, 139-143.

[120] de Jong, M. P., van Ijzendoorn, L. J., & de Voigt, M. J. A. (2000). Stability of the interface between indium-tin-oxide and poly(3,4-ethylenedioxythiophene)/poly(styrenesulfonate) in polymer light-emitting diodes. *Applied Physics Letters*, *77*, 2255-2257.

[121] Tao, Y., Yang, C., & Qin, J. (2011). Organic host materials for phosphorescent organic light-emitting diodes. *Chemical Society Reviews*, *40*, 2943-2970.

[122] Park, Y. W., Kim, Y. M., Choi, J. H., Park, T. H., Jeong, J. W., Choi, H. J., & Ju, B. K. (2010). Enhanced electroluminescence efficiency of phosphorescent organic light-emitting diodes by controlling the triplet energy of the hole-blocking layer. *IEEE Electron Device Letters*, *31*, 452-454.

[123] Zhou, X., Pfeiffer, M., Huang, J. S., Blochwitz-Nimoth, J., Qin, D. S., Werner, A., Drechsel, J., Maennig, B., & Leo, K. (2002). Low-voltage inverted transparent vacuum deposited organic light-emitting diodes using electrical doping. *Applied Physics Letters*, *81*, 922-924.

[124] Naka, S., Okada, H., Onnagawa, H., & Tsutsui, T. (2000). High electron mobility in bathophenanthroline. *Applied Physics Letters*, *76*, 197-199.

[125] Wang, Z. B., Helander, M. G., Greiner, M. T., Qiu, J., & Lu, Z. H. (2009). Analysis of charge-injection characteristics at electrode-organic interfaces: Case study of transition-metal oxides. *Physical Review B, 80*, 235325.

[126] Kröger, M., Hamwi, S., Meyer, J., Riedl, T., Kowalsky, W., & Kahn, A. (2009). Role of the deep-lying electronic states of $MoO_3$ in the enhancement of hole-injection in organic thin films. *Applied Physics Letters*, *95*, 123301.

[127] Hofmann, S., Thomschke, M., Freitag, P., Furno, M., Lüssem, B., & Leo, K. (2010). Top-emitting organic light-emitting diodes: Influence of cavity design. *Applied Physics Letters*, *97*, 253308.

[128] Lee, J., Hofmann, S., Furno, M., Thomschke, M., Kim, Y. H., Lüssem, B., & Leo, K. (2011). Systematic investigation of transparent organic light-emitting diodes depending on top metal electrode thickness. *Organic Electronics*, *12*, 1383-1388.

[129] Wang, Z. B., Helander, M. G., Qiu, J., Liu, Z. W., Greiner, M. T., & Lu, Z. H. (2010). Direct hole injection in to 4,4'-N,N'-dicarbazole-biphenyl: A simple pathway to achieve efficient organic light emitting diodes. *Journal of Applied Physics*, *108*, 024510.

[130] Adachi, C., Tsutsui, T., & Saito, S. (1990). Blue light-emitting organic electroluminescent devices. *Applied Physics Letters*, *56*, 799-801.

[131] Adachi, C., Kwong, R. C., Djurovich, P., Adamovich, V., Baldo, M. A., Thompson, M. E., & Forrest, S. R. (2001). Endothermic energy transfer: A mechanism for generating very efficient high-energy phosphorescent emission in organic materials. *Applied Physics Letters*, *79*, 2082-2084.

[132] Holmes, R. J., Forrest, S. R., Tung, Y. J., Kwong, R. C., Brown, J. J., Garon, S., & Thompson, M. E. (2003). Blue organic electrophosphorescence using exothermic host-guest energy transfer. *Applied Physics Letters*, *82*, 2422-2424.

[133] Bin, J.-K., Cho, N.-S., & Hong, J.-I. (2012). New host material for high-performance blue phosphorescent organic electroluminescent devices. *Advanced Materials*, *24*, 2911-2915.

[134] Chen, J. S., Shi, C. S., Fu, Q., Zhao, F. C., Hu, Y., Feng, Y. L., & Ma, D. G. (2012). Solution-processable small molecules as efficient universal bipolar host for blue, green and red phosphorescent inverted OLEDs. *Journal of Materials Chemistry*, *22*, 5164-5170.

[135] Lee, H., Park, I., Kwak, J., Yoon, D. Y., & Lee, C. (2010). Improvement of electron injection in inverted bottom-emission blue phosphorescent organic light emitting diodes using zinc oxide nanoparticles. *Applied Physics Letters*, *96*, 153306.

[136] Wang, Q., Deng, Z. Q., Chen, J. S., & Ma, D. G. (2010). Realization of blue, green, and white inverted microcavity top-emitting organic light-emitting devices based on the same emitting layer. *Optics Letters*, *35*, 462-464.

[137] Knauer, K. A., Najafabadi, E., Haske, W., & Kippelen, B. (2012). Inverted top-emitting blue electrophosphorescent organic light-emitting diodes with high current efficacy. *Applied Physics Letters*, *101*.

[138] Chiba, T., Pu, Y. J., Miyazaki, R., Nakayama, K., Sasabe, H., & Kido, J. (2011). Ultra-high efficiency by multiple emission from stacked organic light-emitting devices. *Organic Electronics*, *12*, 710-715.

[139] Qi, X. F., Slootsky, M., & Forrest, S. (2008). Stacked white organic light emitting devices consisting of separate red, green, and blue elements. *Applied Physics Letters*, *93*, 193306.

[140] Liao, L. S., Slusarek, W. K., Hatwar, T. K., Ricks, M. L., & Comfort, D. L. (2008). Tandem organic light-emitting mode using hexaazatriphenylene hexacarbonitrile in the intermediate connector. *Advanced Materials*, *20*, 324-329.

[141] Kanno, H., Holmes, R. J., Sun, Y., Kena-Cohen, S., & Forrest, S. R. (2006). White stacked electrophosphorescent organic light-emitting devices employing $MoO_3$ as a charge-generation layer. *Advanced Materials*, *18*, 339-342.

[142] Wang, Q., Chen, Y. H., Chen, J. S., & Ma, D. G. (2012). White top-emitting organic light-emitting diodes employing tandem structure. *Applied Physics Letters*, *101*, 133302.

[143] Cho, T. Y., Lin, C. L., & Wu, C. C. (2006). Microcavity two-unit tandem organic light-emitting devices having a high efficiency. *Applied Physics Letters*, *88*, 111106.

[144] Guo, F. W., & Ma, D. G. (2005). White organic light-emitting diodes based on tandem structures. *Applied Physics Letters*, *87*, 173510.

[145] Chen, C. W., Lu, Y. J., Wu, C. C., Wu, E. H. E., Chu, C. W., & Yang, Y. (2005). Effective connecting architecture for tandem organic light-emitting devices. *Applied Physics Letters, 87,* 241121.

[146] Chang, C. C., Chen, J. F., Hwang, S. W., & Chen, C. H. (2005). Highly efficient white organic electroluminescent devices based on tandem architecture. *Applied Physics Letters*, *87*, 253501.

[147] Law, C. W., Lau, K. M., Fung, M. K., Chan, M. Y., Wong, F. L., Lee, C. S., & Lee, S. T. (2006). Effective organic-based connection unit for stacked organic light-emitting devices. *Applied Physics Letters, 89*, 133511.

[148] Liao, L. S., Klubek, K. P., & Tang, C. W. (2004). High-efficiency tandem organic light-emitting diodes. *Applied Physics Letters, 84*, 167-169.

[149] Liao, L. S., & Klubek, K. P. (2008). Power efficiency improvement in a tandem organic light-emitting diode. *Applied Physics Letters*, *92*, 223311.

[150] Kim, Y.-K., Kim, J. W., & Park, Y. (2009). Energy level alignment at a charge generation interface between 4,4'-bis(N-phenyl-1-naphthylamino)biphenyl and 1,4,5,8,9,11-hexaazatriphenylene-hexacarbonitrile. *Applied Physics Letters*, *94*, 063305.

[151] Lin, L. B., Young, R. H., Mason, M. G., Jenekhe, S. A., & Borsenberger, P. M. (1998). Transient photocurrents across organic-organic interfaces. *Applied Physics Letters*, *72*, 864-866.

[152] Najafabadi, E., Knauer, K. A., Haske, W., Fuentes-Hernandez, C., & Kippelen, B. (2013). Stacked inverted top-emitting white organic light-emitting diodes composed of orange and blue light-emitting units. *Applied Physics Letters*, *103*, 193303.

[153] deMello, J. C., Wittmann, H. F., & Friend, R. H. (1997). An improved experimental determination of external photoluminescence quantum efficiency. *Advanced Materials, 9,* 230-232.

[154] Chen, S.-Y., Chu, T.-Y., Chen, J.-F., Su, C.-Y., & Chen, C. H. (2006). Stable inverted bottom-emitting organic electroluminescent devices with molecular doping and morphology improvement. *Applied Physics Letters*, *89*.

[155] Chu, T.-Y., Chen, J.-F., Chen, S.-Y., Chen, C.-J., & Chen, C. H. (2006). Highly efficient and stable inverted bottom-emission organic light emitting devices. *Applied Physics Letters*, *89*, 053503.

[156] Najafabadi, E., Knauer, K. A., Haske, W., & Kippelen, B. (2013). High-performance inverted top-emitting green electrophosphorescent organic light-

emitting diodes with a modified top Ag anode. *Organic Electronics*, *14*, 1271-1275.

[157] Lindla, F., Boesing, M., Zimmermann, C., Jessen, F., van Gemmern, P., Bertram, D., Keiper, D., Meyer, N., Heuken, M., Kalisch, H., & Jansen, R. H. (2009). Highly efficient yellow organic light emitting diode based on a layer-cross faded emission layer allowing easy color tuning. *Applied Physics Letters*, *95*, 213305.

[158] Lunt, R. R., Lassiter, B. E., Benziger, J. B., & Forrest, S. R. (2009). Organic vapor phase deposition for the growth of large area organic electronic devices. *Applied Physics Letters*, *95*, 233305.